Ensemble Estimation and Analysis of Network Parameters

- Strengthening the GIC Modelling Chain -

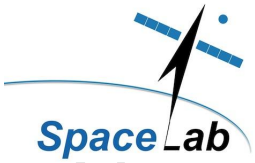

Prepared by:
Michael John Heyns

Supervisor:
Prof. C. T. Gaunt
Department of Electrical Engineering
University of Cape Town

Co-supervisor:
Dr. S. I. Lotz
SANSA Space Science
South African National Space Agency

April 2017

Submitted to the Department of Electrical Engineering, University of Cape Town, in partial fulfilment of the requirements for the degree of Master of Philosophy.

Declaration

This thesis/dissertation has been submitted to the Turnitin module (or equivalent similarity and originality checking software) and I confirm that my supervisor has seen my report and any concerns revealed by such have been resolved with my supervisor. Furthermore, I confirm that I understand the meaning of plagiarism and that it is wrong. All work presented in this thesis/dissertation is my own, unless otherwise acknowledged or deemed to be as part of the normal guidance offered by my supervisor.

Name: Michael John Heyns
Student number: HYNMIC005

Signed by candidate
Signature: Signature Removed
Date: 2017/06/22

Acknowledgements

This project has been impacted by many different people coming from diverse backgrounds, each with input improving aspects of what came before. It has been an absolute pleasure and privilege putting together the final result you are now reading.

Firstly, I would like to acknowledge the main drivers behind the project, Prof. Gaunt from the University of Cape Town (UCT) and Dr. Lotz from SANSA Space Science in Hermanus. Much is owed to Prof. Gaunt's vision and in-depth understanding of the big picture and how all the components fit together. Seldom does one come across an individual as accomplished in all the different facets of the field as Prof. Gaunt. Even more rare is an individual that takes the time for numerous discussions and guidance that moulds the work into what it is. Dr. Lotz has been a pillar of support throughout the course of this work, patiently listening to a constant barrage of enthusiastic ideas and then helping hone them into something sensible. Above and beyond this, he has helped navigate the rather daunting and mysterious world of research from the point of view of a researcher at a research institute.

Also at SANSA, I would like to thank Prof. Cilliers. His energy was absolutely contagious and provided data, insights and comments at the drop of hat. Further thanks needs to go to the staff at SANSA that have hosted me for the duration of the work and allowed me to be part of the organisation. All the way from Canada, I would also like to thank Dr. Danskin. Not only did he provide fantastic insights, but also support and encouragement in the initial phases of the work. Much stimulation also came from the SANSA/UCT GIC Work-group, which included SANSA, UCT and NRCAN researchers, namely Dr. Lotz, Dr. de Villiers, Prof. Cilliers, Prof. Gaunt, Dr. Oyedokun and Dr. Danskin.

Although based at SANSA and working with SpaceLab in the Electrical Engineering department at UCT, the project started initially as part of (and was funded for the duration of the work by) the DST-NRF NASSP Masters programme based in the Astronomy department. Special thanks needs to go to Dr. van der Heyden (NASSP) and Prof. Martinez (SpaceLab) which facilitated the move and more. I know the thought of all the paperwork involved still causes headaches.

Finally, I would like to express my sincere appreciation to John Heyns who was always interested in the work and the best sounding board I could ever ask for.

> "It ain't what you don't know that gets you into trouble. It's what you know for sure that just ain't so."
>
> -Mark Twain

Abstract

Large grounded conducting networks on Earth's surface have long been known to be affected by solar activity and geomagnetic storms. Geomagnetically induced currents (GICs) in these quasi-antennas are just one of the effects. In modern times, society has become more and more dependent on electrical power and, as a result, power networks. These power networks form extensive grounded conductors and are susceptible to GICs, even at mid-latitude regions. Given a large enough event now, such as the Carrington event of 1859, the direct and knock-on results can be devastating. Such an event is more than just a possibility, it is just a matter of time. With this in mind, the study of the effects of GICs and the modelling of them has become essential to ensure the future security of society in general.

GIC modelling makes the assumption that the resultant GIC at a specific node in a power network is assumed to be linearly related to the horizontal vector components of the geoelectric field, which is induced by a plane-wave geomagnetic field. The linear GIC and geoelectric field relation is defined by a pair of network parameters, a and b. These parameters are not easily measurable explicitly but may be estimated empirically. Furthermore, these parameters are traditionally only seen to include network information and remain constant given a stable network.

In this work, a new empirical approach to derive estimates for a and b is presented where the linear relation is solved simultaneously for all possible pair of time instances. Given a geomagnetic storm time-series (length n) of simultaneous GIC and geoelectric field data to solve for a and b, taking all possible time instance pairs yields approximately $n^2/2$ estimates for a and b. The resulting ensembles of parameter estimates are analysed and found to be approximately Cauchy-distributed. Each individual estimate resulting from a single pair of time instances being solved is not the true state of the system, but a possible state. Taking the ensemble as a whole though gives the most probable parameter estimate, which in the case of a Cauchy-type distribution is the median. These ensemble parameter estimates are used in the engineering link of the modelling chain, but the ensembles themselves allow further analysis into the nature of GICs.

An improvement is seen when comparing the performance of the ensemble estimates applied to an out-of-sample dataset during the Halloween Storm of 2003 with previous GIC modelling in the South African power network using the same dataset. Analysis of the ensembles has verified certain ground assumptions (specifically the plane-wave assumption and network directionality) made as a first-order approximation in GIC modelling and has also shown that errors from these assumptions are absorbed into empirically derived network parameters. Using a range of estimates from the ensemble, a GIC prediction band is produced. This in itself corresponds to an error estimate in the prediction. For the first time, it has been explicitly shown that empirically derived network parameters show a correlation to the magnitude of the produced GIC. This behaviour is then used to refine the parameter estimation further and allow for real time dynamic network parameter estimation that further improves modelling.

Contents

List of Tables

List of Figures

1 Introduction

Extensive grounded conducting networks on the surface of Earth have long been known to be affected by geomagnetic activity. Geomagnetically induced currents (GICs) are one of the potentially damaging effects in power networks. The nature of GICs in these quasi-antennas is a text book application of Maxwell's equations, specifically Faraday's Law of Induction. GICs are the final link in a chain of coupled systems. These currents on the surface are coupled directly to the induced geoelectric field, which is in turn induced by fluctuations of the geomagnetic field. The geomagnetic field perturbations are linked to current systems in the near-Earth environment. The magnetospheric and ionospheric current systems, all interrelated, are driven by the solar wind. The solar wind finds its roots in the Sun itself - the first link in the chain. A large event on the Sun, such as a coronal mass ejection (CME), propagates through the chain and is experienced on Earth as a geomagnetic storm. Such large disturbances in the current systems are the main drivers for GICs [48].

Figure 1: An artist's impression of geomagnetically induced currents resulting from an extreme geomagnetic storm [Image credit: Illustration No. 2 in the Solar Storm Disaster Series, Kenn Brown & Chris Wren, Mondolithic Studios and Mondoworks, 2009].

1.1 Geomagnetic Storms

The Sun is in a constant state of flux, on average spewing out energy at 3.86×10^{26} Joules/sec [13]. This is roughly the output of more than a billion Tsar Bomba Hydrogen bombs, which is the most powerful nuclear weapon ever tested... per second! Those are just average figures. Given that the ambient or average solar wind speed is roughly 350 km/s, when there is a coronal mass ejection (CME), the density of energetic particles increases significantly along with solar wind speed (between 10^{15} and 10^{16} grams are blasted off the Sun). This plasma hurtles through space at more than 1000 km/s. As if that is not enough, this speed is supersonic in the interplanetary medium and produces a shock front as well. Such a CME can reach Earth in less than a day [13]. The sheer extent of that energy output means that a significant disturbance on the Sun, such as a CME, would definitely be felt on Earth, besides the typical sunburn on a hot day. In general solar-terrestrial activity is used to describe the changes of energetic particles and magnetic fields (loosely known as plasma

when considered together) that originate on the Sun and travel to Earth's magnetosphere. Given a large enough disturbance, when this plasma reaches the magnetosphere the Earth experiences a geomagnetic storm.

Solar activity itself is on short time-scales relative to human perception. A region or process on the Sun is said to be active when a particle or field disturbance in Earth's magnetosphere can be linked to that specific region or process. On the other hand, the Sun is said to be active when the magnitude of changes is large relative to the average behaviour over a period of tens of years. A typical example of this is the solar cycle of 11 years, as defined by sunspots. During this 11-year cycle, the number of sunspots changes as well as the radial outflow of solar plasma. Another periodicity related to this is the 22-year alternation of sunspot group polarity. There are a number of other supposed cycles, but due to the limited time period since data was first collected (reliable annual sunspot numbers from 1650 onwards) these are not properly tied down. An example of this is the supposed 80-90 year cycle that modulates the amplitude of the conventional solar cycle [13].

Before looking at geomagnetic storms and ultimately their effects on infrastructure on Earth, it pays to look into the main drivers of solar activity. The first link in the chain of processes lies within the Sun after all. The Sun can be divided broadly into four regions. Right at the centre is the high-temperature, high-density core where thermonuclear reactions occur. These reactions generate virtually all the energy output. The region itself is roughly a quarter of the solar radius but contains half the Sun's mass. The radiative region around the core is made up of hydrogen not yet part of the thermonuclear reactions. Photons and other energetic particles from the core are continuously scattered, absorbed or re-emitted in this region on their way out to the surface. Next is the convection zone, which is convectively unstable. This zone makes up the last 30% of the solar interior. Lastly comes the solar atmosphere, which includes the photosphere (visible surface), the chromosphere, the transition region and the corona (outermost part of solar atmosphere that extends many solar radii, finally becoming the solar wind). This region is visible from a distance away from the Sun and is where energy is radiated out into space as the solar wind.

Although most processes in the Sun are linked to the core, most of the disturbances seen in the small scale structure on the surface (photosphere) are related to the dynamics in the layer immediately below it. As mentioned above, the convective zone of the Sun is convectively unstable. This is the result of the radial temperature gradient being more negative than the adiabatic gradient. If we assume negative temperature gradients, this equates to,

$$\left|\frac{dT}{dr}\right| > \left|\left(\frac{dT}{dr}\right)_{ad}\right|. \tag{1}$$

When this is the case, buoyancy forces create up and down motions. In the radiation zone, the opposite is true and the plasma is convectively stable, i.e.

$$\left|\frac{dT}{dr}\right| < \left|\left(\frac{dT}{dr}\right)_{ad}\right|. \tag{2}$$

This condition is known as the Schwarzchild condition. In the convection zone, the up and down motions result in convection cells (see Figure 2) that range from 1000 km (known as granules) to cells a third the size of the Sun (known as giant cells) [16].

Both the Earth and Sun rotate and contain conductive materials. This in general terms is what drives the main magnetic fields. In the Sun's case, the system is much more complicated, with the Sun being made up of plasma and having differential rotation (the rotation period at the equator is roughly 27 days and is commonly used to define the general rotation period). This differential rotation means that the rotation frequency is somewhat greater at the core than the surface and also greater at the equator than at other latitudes. On top of this, we have the convection zone where

convective motions also have to be taken into account. Now assuming a magnetic field frozen into a plasma package (a seed field), as is the case in the Sun, these other motions will distort and twist the field line [16]. Assuming the dominant equatorial rotational motion, the seed field is stretched in the azimuthal direction. This would create a toroidal field (see Figure 3). Now, taking into account the convection zone, the plasma would rise and distort the field line. The Coriolis force then would twist the plasma package and the associated field line, resulting in a poloidal field in the north-south direction (with a complicated loop).

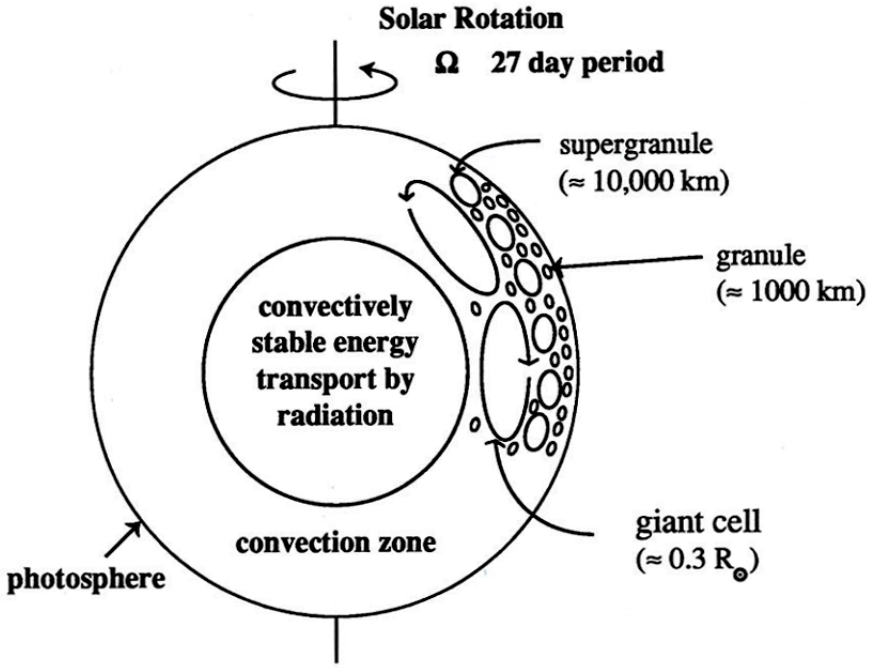

Figure 2: A representation of the interior of the Sun with different convection cells which contribute to the complicated solar magnetic field [Image credit: (Cravens, 1997) [16]].

These convection cell fields have different sizes and manifest themselves on the Sun's surface. A typical example is sunspots, which are thought to be related to supergranule convection cells. This aside, the Sun has a large scale magnetic field that is roughly dipole. At the polar regions, this field is rather uniform and of opposite polarity as expected. At low- and mid-latitudes, the field is much more complex and shows evidence of fields associated with convection cells. These cells, forming part of the smaller scale structure, define the typical time scales for magnetic variation in the Sun. A typical sunspot lasts for about a month and is roughly related to a convection cell 'overturning'. The 'overturning' of the largest convection cells takes roughly 22 years, which in turn is related to the solar cycle. Every 11 years the polarity of the 'average' solar dipole reverses [16]. Geomagnetic activity on Earth also follows this solar cycle. The maximum occurrence of geomagnetic activity is usually delayed by about 1 to 2 years after solar maximum (when the maximum number of sunspots on the solar disc is observed). This is as a result of the changing latitude of sunspots which coincides with the Earth's orbital plane. At solar maximum, the majority of sunspots would still be at too high a latitude to be geoeffective. As the average sunspot latitude decreases with the solar cycle, the number of geoeffective sunspots increases but the total number of sunspots decreases. The optimum between these two trade-offs is the typically observed 1 to 2 year lag [14].

On the photosphere, granulation of roughly 1000 km is visibly observable. This is directly a result of the convection cells below and has a characteristic time of 10 minutes. Supergranulation is also present, but much harder to identify on top of the other forms of granulation. Seeing this larger structure is easier when observing the magnetic fields, the motion of gas or manifestations of supergranulation in the chromosphere, such as spicules. Supergranulation cells are of the order of 20 000

km across and have lifetime of a couple of days. Apart from these general structures, there are more specific structures of interest, often also directly related to granulation and supergranulation.

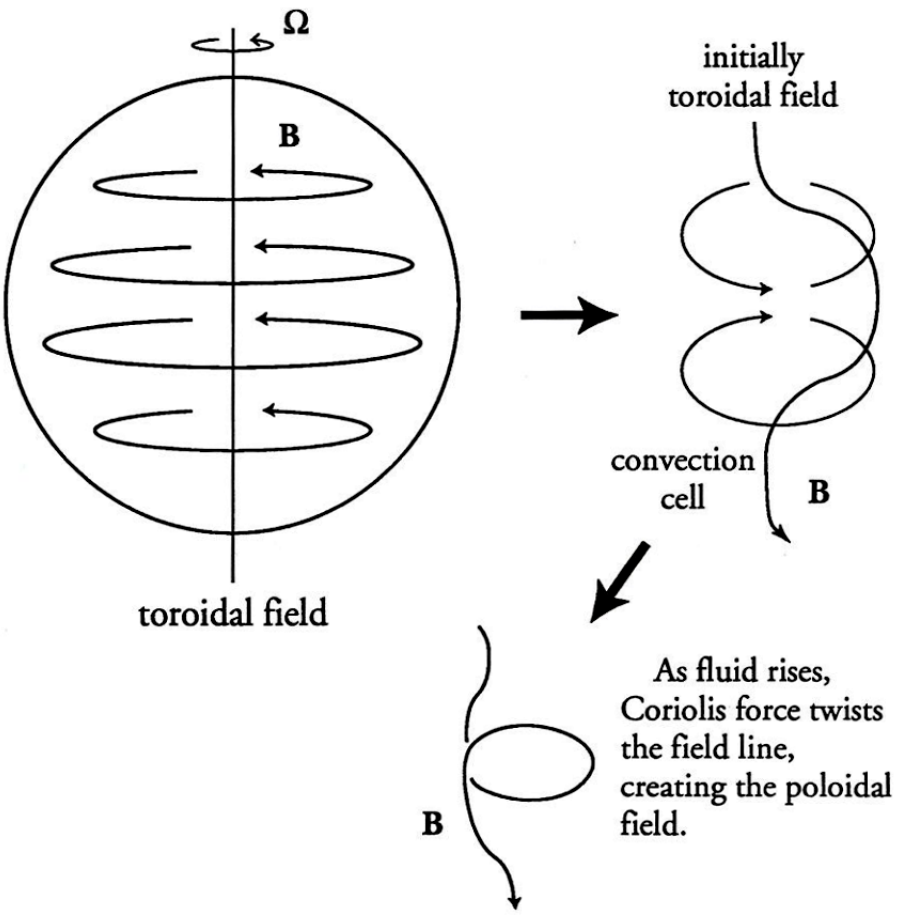

Figure 3: A sketch of the toroidal and poloidal fields created by convection cells [Image credit: (Cravens, 1997) [16]].

Sunspots were probably the first observed structures on the surface of the Sun. The discovery of sunspots by Galileo in 1612 allowed him to postulate that the Sun was rotating. Sunspots have an extent related to supergranulation, being roughly 20 000 km in diameter. They appear darker on the surface of the Sun as they are cooler (3000 K cooler) than the surrounding regions. Groups of sunspots are associated with active regions in the overlying chromosphere. The magnetic field associated with sunspots is particularly strong, of the order of 0.1 Tesla (a 1000 times greater than the average photospheric field). In the case of sunspot groups, the magnetic field can be excessively complex, but can also be unipolar or bipolar. On the solar disc, sunspots appear in two latitude zones, one in each hemisphere. They are further closely related to the solar cycle, varying in number (first increasing and then decreasing) and location (starting at mid-latitudes of around ±35° and progressing to equatorial latitudes of around ±10-15°) during the course of the cycle. The basic driver of sunspots is directly related to the dynamo mechanism in the convection zone and is illustrated best with a single sunspot pair. When a plasma parcel with a 'frozen' in magnetic field line (often with a complicated loop) in the convection zone becomes buoyant and moves upward, it also cools adiabatically. When it emerges at the surface, it is often cooler than the surrounding photosphere, i.e. as a bipolar sunspot pair with two 'spots' where the magnetic field lines penetrate the surrounding area. If the cooling is too extreme, buoyancy is lost and the sunspot disappears. The strong magnetic field associated with sunspots extends into the chromosphere and results in an active region (which may contain magnetic 'arch' or 'loop' structures). Given a sunspot pair, often the leading sunspot (in the direction of solar rotation) has opposite polarity in the Northern and Southern hemispheres.

As with the average solar magnetic dipole, every solar cycle the polarity swaps.

Filaments (prominences viewed from directly above) and prominences extend from the chromosphere into the corona as arch-like structures, stretching up to 100 000 km and being 6000 km thick and 50 000 km above the surface. It is thought that a magnetic cushion and very strong magnetic fields support these semi-static structures. A particular type of prominence, the quiescent prominence is typically 300 times cooler than the surrounding gas. The equilibrium maintained by the magnetic cushion is not always maintained. Solar flares are explosively eruptive prominences that release huge amounts of energy across the electromagnetic spectrum. It is generally thought that magnetic reconnection provides a mechanism for this release of energy. Another typical structure is a coronal hole. Coronal holes are very large in extent (up to half a solar radius) and extend far out into the corona. These 'holes' are associated with open field lines and high-speed solar wind streams. These high-speed streams have the effect of compressing the ambient solar wind as a result of the Archimedian spiral created by the solar rotation. The resulting collisionless shocks add to the complexity and turbulence of the solar wind.

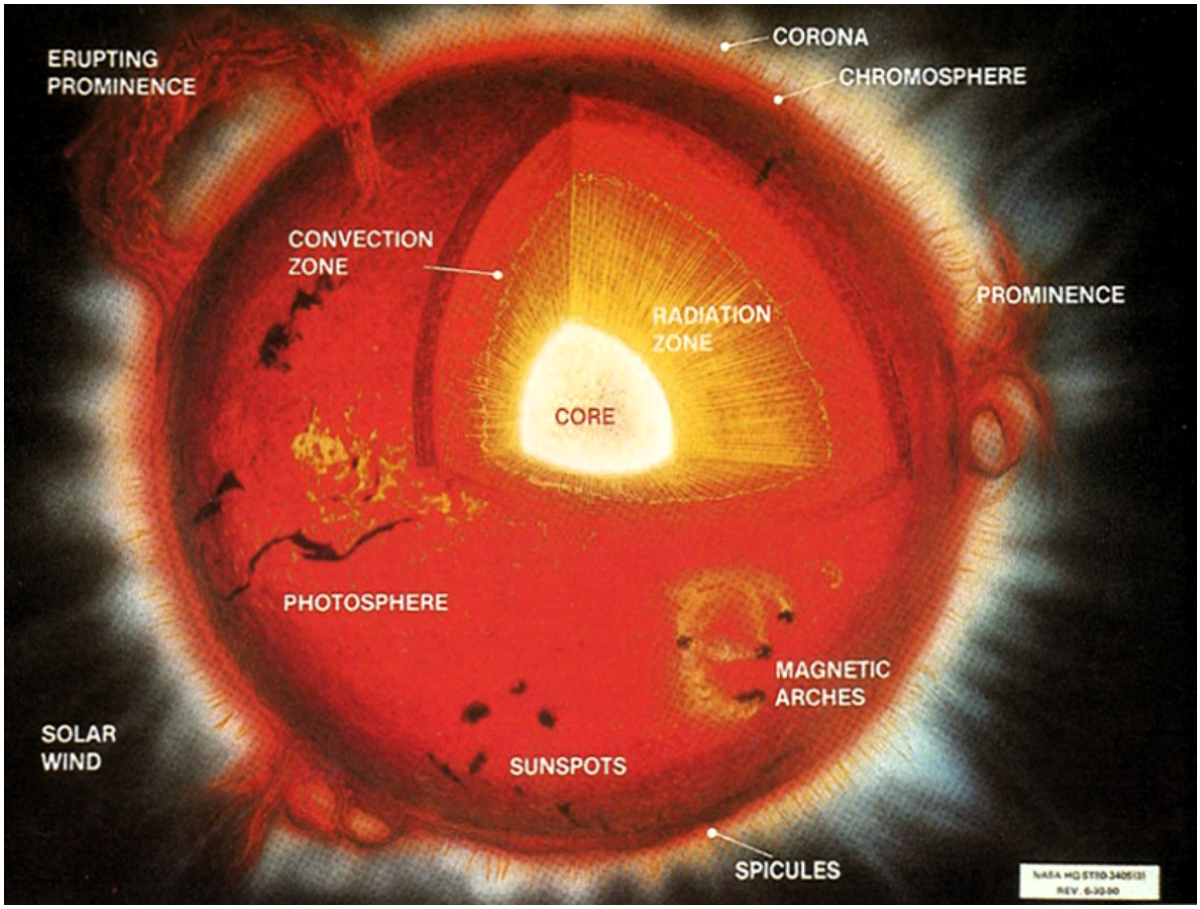

Figure 4: An illustration by NASA showing various important features of the Sun [Image credit: (Campbell, 2001) [14]].

Related to prominences are coronal helmet streamers and the CMEs (coronal mass ejections) mentioned earlier. These are much larger than prominences, being in the order of 0.5 to 1 solar radii as well as being relatively dense (and bright in the visible spectrum). Helmet streamers extend from the inner corona, where they are associated with closed field lines, to the outer corona, where the field lines open. When helmet streamers become unstable, they are ejected from the surface as CMEs in a similar way to a typical explosively eruptive prominence. It should be noted that although related, there is not a very good correlation between CMEs and solar flares. This bulk of coronal plasma (billions of tons) accelerates through the interplanetary medium. Ahead of this plasma is usually a

build-up of particles in the form of a shock front. Along with CME plasma comes enhanced solar wind dynamic pressure and possibly an interplanetary magnetic field (IMF) change from the typical northward to southward. These are thought to be the main drivers of geomagnetic storms.

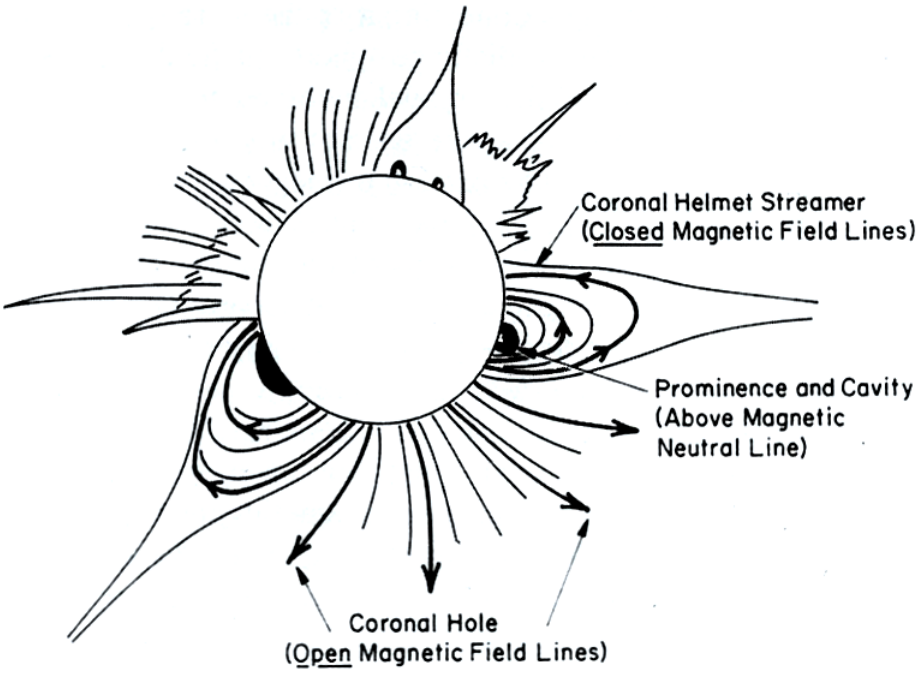

Figure 5: A sketch of magnetic field structures within the coronal features observed during the 1966 solar eclipse, which in effect is a natural coronagraph [Image credit: (Kivelson, 1995) [28]].

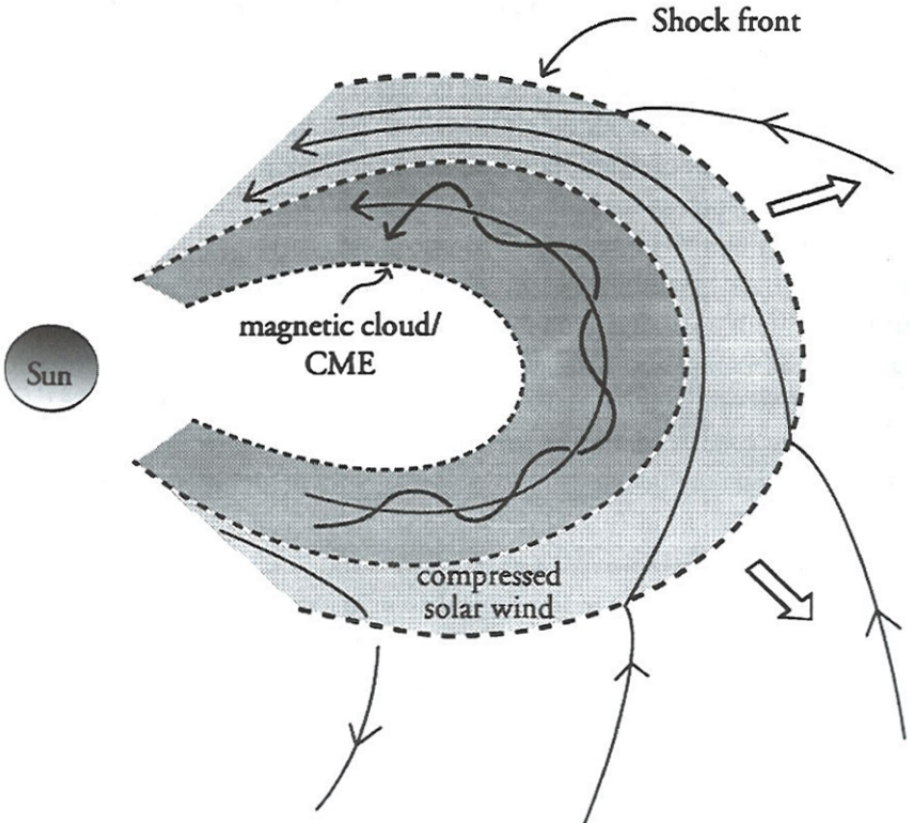

Figure 6: A sketch of the propagation of a CME through the interplanetary medium [Image credit: (Cravens, 1997) [16]].

When charged particles in the solar wind encounter Earth's magnetic field, the Sun-ward boundary of the magnetosphere is forced inward by the bow shock (for now we ignore the effects of the IMF). The solar wind then reconfigures the entire magnetosphere into a tear drop shape with a trailing tail. The outer boundary is called the magnetopause and the region between the bow shock and magnetopause is called the magnetosheath. In this 'closed' model, sheet currents flow on the magnetopause (known as Chapman-Ferraro currents). These currents close on themselves or through the current sheet (plasmasheet) at the center of the magnetotail. The magnetopause current in effect cancels the dipole field outside the magnetopause (but doubles the dipole field inside the magnetopause). This effect is felt on Earth when an increase in solar wind dynamic pressure (as a result of an interplanetary shock) compresses the magnetosphere and pushes the magnetopause closer to Earth. The magnetopause current intensifies and there is an increase in the geomagnetic field by a few tens of nanotesla. This increase is seen as the sudden impulse or sudden storm commencement (discussed later). Another important feature in the 'closed' model of the magnetosphere is the cusp region. This is the region where the geomagnetic field lines are split between those that are 'closed' in on themselves at the poles and 'open' field lines that extend down the magnetotail. The boundary layer reaches deep into the magnetosphere here and magnetosheath plasma has its most direct access to the magnetosphere. The cusp regions create the auroral oval where energetic particles precipitate into the upper atmosphere, causing aurorae.

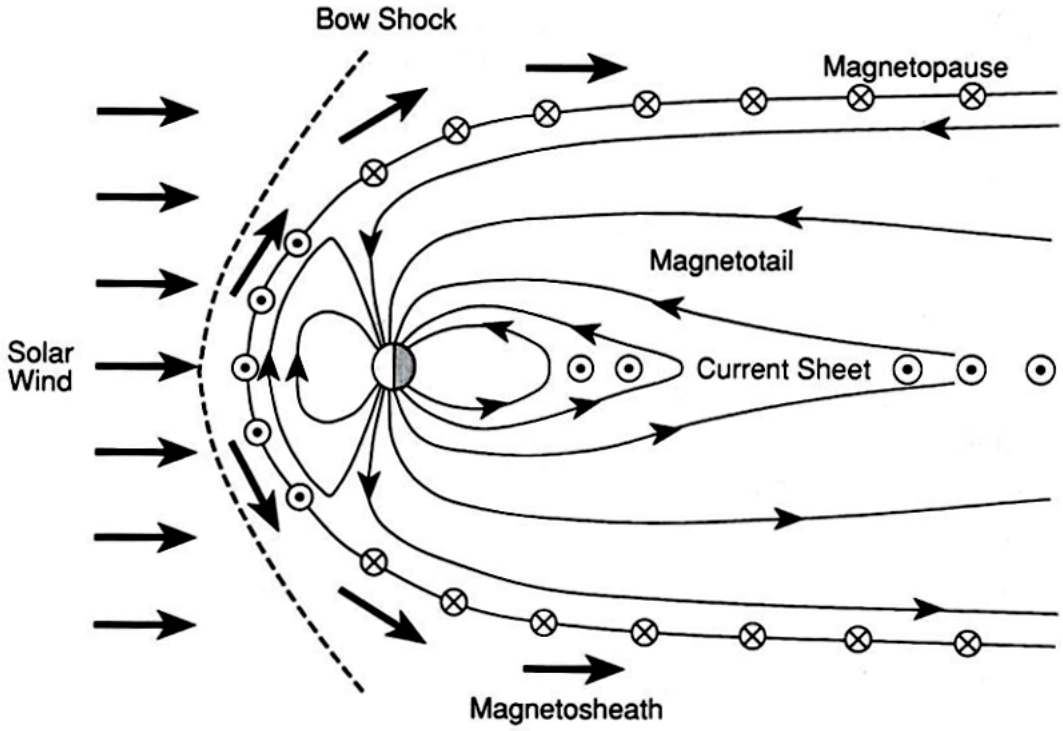

Figure 7: The simplest 'closed' model of the magnetosphere in the noon-midnight meridian - the geomagnetic field is confined by sheet current on the magnetopause which joins the secondary midplane current sheet at the flanks of the tail. The solar wind is deflected at the bow shock and flows around the magnetosphere, creating the magnetosheath [Image credit: (Kivelson, 1995) [28]].

There are a number of shortcomings of the 'closed' model. These can be summarised as (i) the plasma is assumed to be collisionless and an effective viscosity needs to be introduced to explain momentum transfer to the magnetopause, (ii) there is no dependence on IMF orientation, but observations show sensitivity to this and finally (iii) particle measurements, especially in the cusp region, show evidence for 'open' field lines.

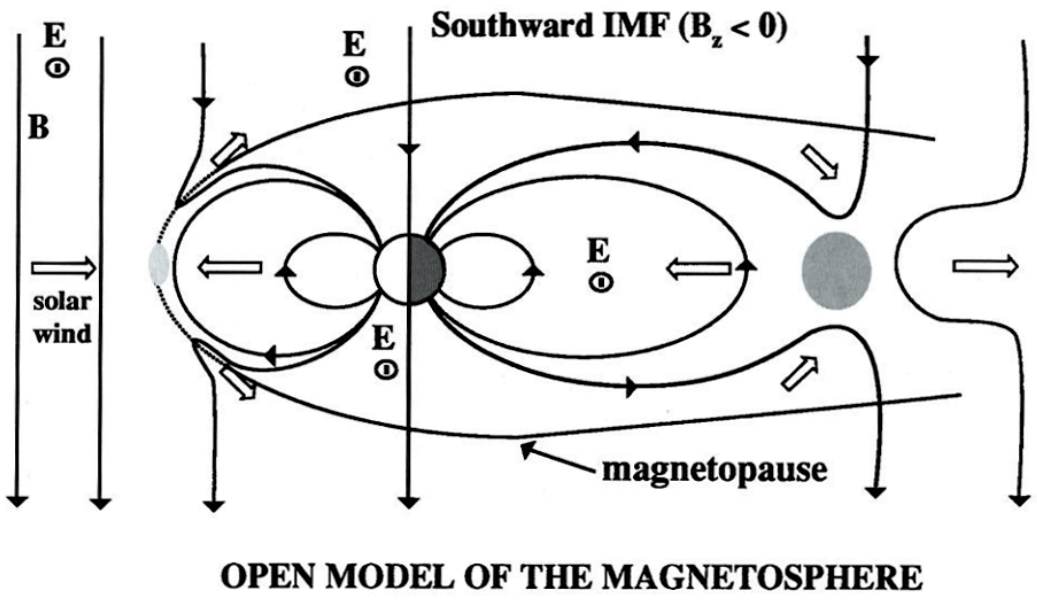

Figure 8: During disturbed time associated with a southward IMF (high geomagnetic activity), the 'open model' is favoured - reconnection areas are shaded in the diagram above [Image credit: (Cravens, 1997) [16]].

The aptly named alternative 'open' model addresses these shortcomings. In this model, it is proposed that the magnetosphere connects to the IMF via magnetic reconnection. The solar wind electric field can thus map to the open field lines and create a convection electric field along the magnetopause from the dawn to dusk side of the Earth. The plasma responds with a $E \times B$ drift as observed in the magnetopause sheet currents. The extent of this drift is dependent on the efficiency of the reconnection, the most efficient being for a southward IMF. When this is the case, the IMF is anti-aligned with the geomagnetic dipole enabling simple reconnection in a diffuse region on the day-side of the magnetopause. Reconnection with non-southward IMF is much more complicated. These reconnected field lines then convect tailward over the polar caps. Magnetic flux accumulates in the tail where circulation forms an intense westward tail current (measurable at low-latitudes during the midnight hours). Field lines again reconnect in this region. These magnetic field lines are then carried back to the Earth along with plasma, which is often associated with geomagnetic substorms [16].

At this point, it should be noted that geomagnetism is a global phenomenon that shows different behaviour at different latitude regions [14]. These regions are not strictly defined, but rather relatively. The main regions of reference are the auroral zones, in the polar regions where aurorae are seen, and the equatorial region, where the geomagnetic field is purely horizontal. From these relative measures, the following zones are defined:

1. polar caps - where the geomagnetic field is near vertical (different to the geographical poles).
2. auroral zones - where the auroras are most commonly seen.
3. high-latitudes - near enough to the auroral zones to be significantly affected during solar driven geomagnetic disturbances.
4. equatorial region - within the magnetic dip equator, which is different to the geographical equator, being defined as the region where the geomagnetic field lines are parallel to the Earth's surface (this purely horizontal field creates unique upper-atmosphere effects).
5. low-latitudes - just outside the equatorial region.
6. mid-latitudes - the regions between the high- and low-latitudes (also the most populated).

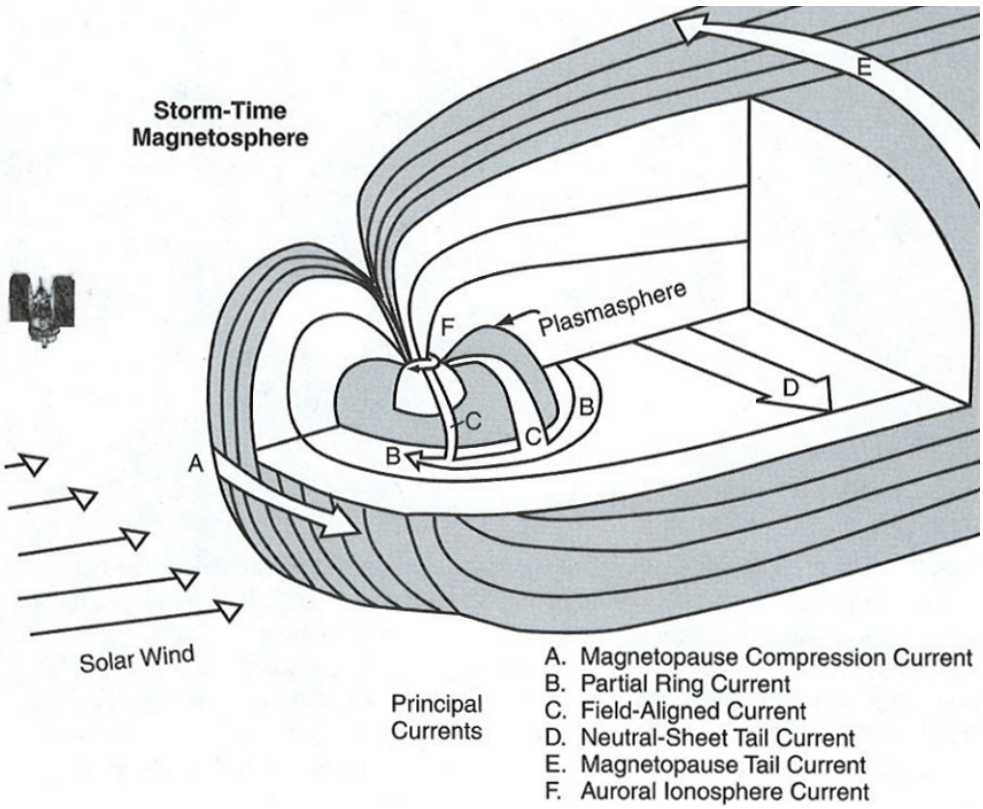

Figure 9: Considering either open or closed magnetosphere model, a number of principle currents are observed in the magnetosphere during a geomagnetic storm [Image credit: (Campbell, 2001) [14]].

Given either model of the magnetosphere, there are a number of current systems that need to be taken into account, especially during geomagnetic storms. Originally it was believed that the large negative field seen during a magnetic storm at low-latitudes magnetic observatories was a feature of the radiation belts (such as the Van Allen belts) that circle the Earth. Specifically, it was thought that a main ring current grew with the arrival of the solar wind ions and decayed as the particles disappeared with recombination. This is in fact only a first order approximation of a number of different current systems that interact and contribute to the end observed effect. In Figure 9 above, principal currents A, D and E have already been discussed in the large scale context. In the region closer to Earth though, currents (B) were found to be briefly part of the ring region, but then dump their particles through field-aligned or Birkeland currents (C) into the high-latitude ionosphere (the partially ionised region of the upper atmosphere).

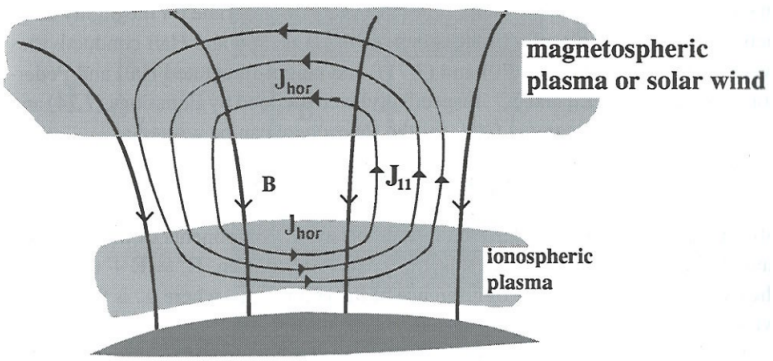

Figure 10: The magnetospheric plasma is linked to ionospheric plasma by magnetic field lines (current densities are shown as streamlines) - the current component aligned to the magnetic field lines are known as field-aligned or Birkeland currents (denoted by $J_{||}$) [Image credit: (Cravens, 1997) [16]].

These field-aligned currents are also large contributors to the storm disturbance measured by magnetometers from the polar regions through to the mid-latitudes. Completing the circuit, currents in the ionosphere create a westward auroral electrojet (F) which dominates the geomagnetic field disturbances in the polar regions. As a result of conductivity, parts of these electrojets are lead from the auroral zone to low- and equatorial latitudes, where they also affect measurements. As a general practice, the magnetic fields of these current systems are represented as contours of current flowing parallel to the surface in the ionosphere. These are referred to as equivalent ionospheric currents.

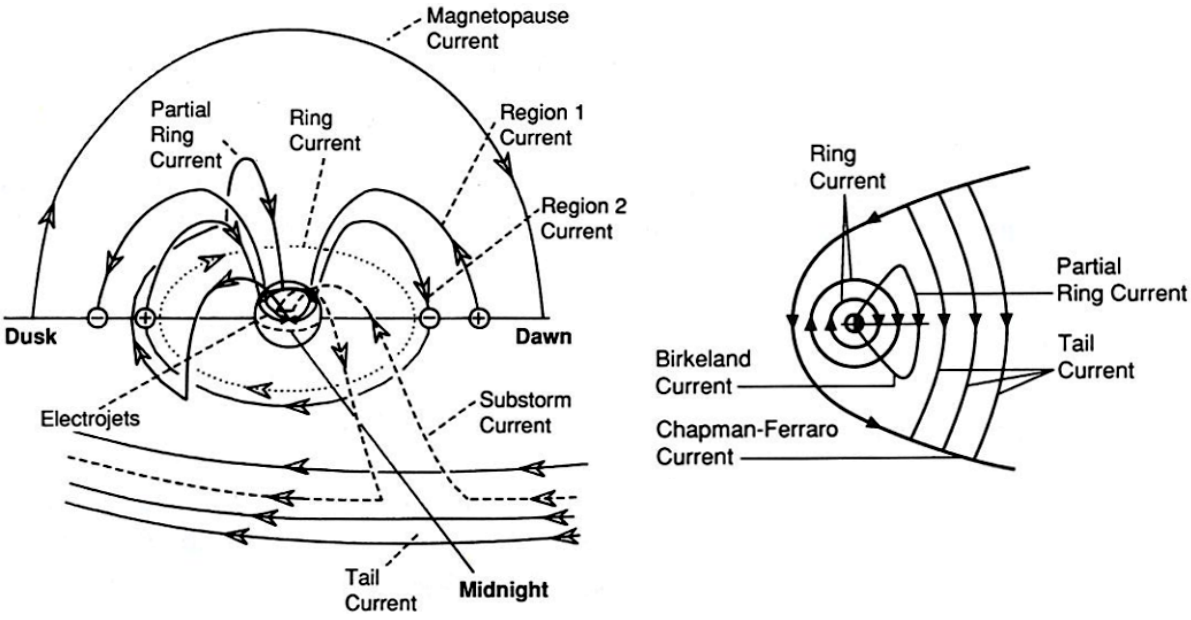

Figure 11: A highly schematic diagram showing the different current systems (see text for more detailed description) linking the magnetospheric and ionospheric currents responsible for geomagnetic activity [Image credit: (Kivelson, 1995) [28]].

Returning to the ring current region, it is now thought that the region is located in the inner magnetosphere, around the plasmapause. The plasmapause is the boundary of the plasmasphere, which itself is a doughnut-shaped low-latitude region near Earth (less than a few Earth radii). This region is made up mostly of ionospheric plasma. The ring current region contains particles with energies in the order of tens of KeV as well as colder plasmaspheric plasma. The trapped radiation belts (Van Allen belts) are higher energy extensions of the ring current region, with MeV particle energies. Generally the colder plasmas are dominated by $E \times B$ drift, but the more energetic ring current region also has magnetic gradient and curvature drifts. It is these drifts, along with a magnetisation current, that produce the westward electrical current around the Earth, known now as the ring current. A typical current amplitude is about one million amperes, but varies significantly with geomagnetic activity (the trapped radiation belts are more stable). The ring current ions are 'injected' into the inner magnetosphere from the plasmasheet region in the tail during geomagnetic storms. As mentioned above, besides the ring current, there are also the partial ring currents in the mid-magnetosphere that flow part of the way around the Earth. These are linked by field-aligned (Birkeland) currents to the ionosphere where conduction currents complete the circuit as auroral electrojets (see Figure 10). This is known as the Region 1 current system which connects the open magnetic field lines of the solar wind and magnetopause with the polar ionosphere. Additional field-aligned currents link the tail and magnetopause. This is known as the Region 2 current system and connects the plasmasheet to the auroral ionosphere through closed field lines.

In general, geomagnetic storms display common features [13]. An intense global geomagnetic storm has been defined as a period when the *Dst* (disturbance storm time) index or its high resolution counterpart, SYM-H (symmetric disturbance in the H-field) [66], drops below -100 nT [23]. Both these

indices are indicative of ring current intensity and to a lesser extent, the magnetopause and partial ring currents. Measurements for both indices are made by a global network of magnetometers, near the equator (not right at the equator since the ionospheric equatorial electrojet can also result in magnetic field perturbations).

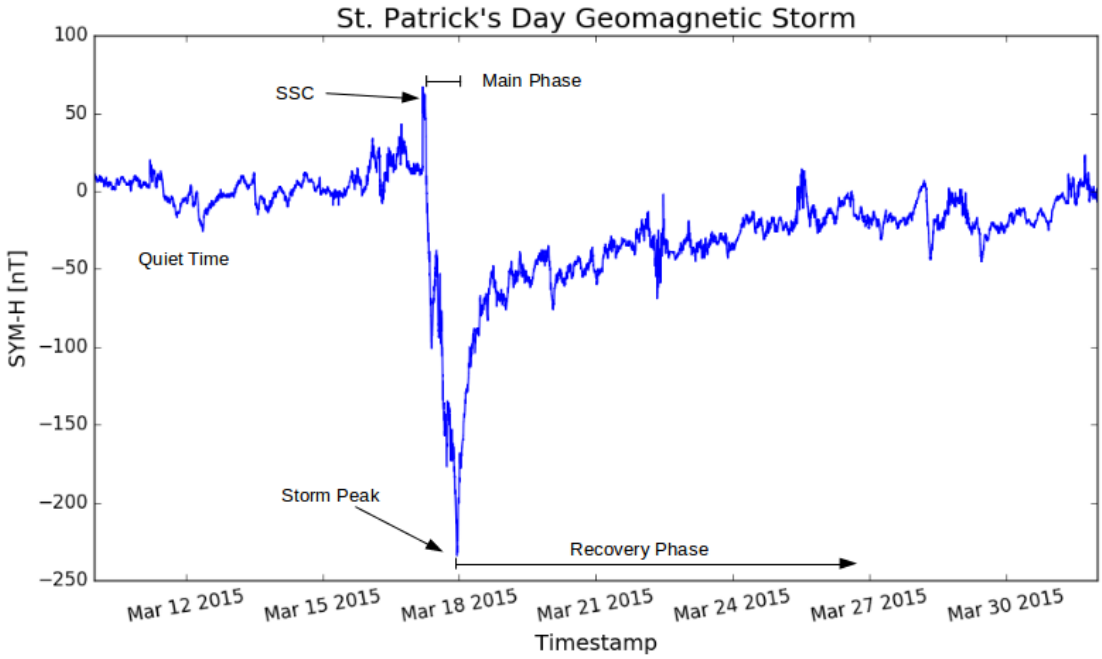

Figure 12: The St. Patrick's Day Storm of 17 March 2015 is a typical geomagnetic storm - in this SYM-H plot the different storm phases indicated.

Typically, a geomagnetic storm would start with a sudden commencement (SC) or sudden storm commencement (SSC) that occurs almost instantaneously anywhere on Earth (see Figure 12). This corresponds to the shock wave formed by the arrival of the fast solar-wind plasma at the magnetosphere. The SC is often, but not in all cases, followed by an increase in the geomagnetic northward field. This is called the initial phase and is a compression effect which can last for a number of hours. The next phase, which sometimes is the only visible phase, is the main or growth phase of the storm. The principle geomagnetic field component decreases and shows major fluctuations for a much longer time and with larger amplitudes than the initial phase. It is during this phase that aurorae and intense electrojets are observed. Following this, the geomagnetic field gradually recovers to its original undisturbed level. This is called the recovery phase and takes much longer than all previous phases put together, in some cases lasting as long as several days. Of course, in certain cases when the Sun is particularly active, a second CME can hit Earth during this recovery phase. The cumulative effects of CME chains are particularly destructive, as seen with the Halloween Storm of 2003 (see Figure 22).

As mentioned previously, the direction of the IMF is critical to the magnetospheric and hence geomagnetic field response to a CME. When the IMF is northward at the arrival of the plasma, then there is no subsequent geomagnetic storm. The shock effects however do remain, and the result is called a sudden impulse (SI). Both SC and SI events are believed to be produced by magnetospheric currents and ionospheric currents caused by compressional waves propagating in the magnetosphere. As a result SC's and SI's are strongest at the magnetic dip equator on the summer hemisphere due to enhanced conductivity (increased ionisation). Given the case that the IMF is southward, a geomagnetic storm is likely to follow. The main phase of the resulting storm is dependent on the southward IMF being sustained at the magnetosphere boundary. This allows injection of particles into the magnetosphere and a charge separation arises between the dawn and dusk sides. The potential dif-

ference results in equatorial drifts of the injected particles in the partial ring current. Furthermore, this feeds the field-aligned current systems that link the magnetosphere and ionosphere. When this southward IMF switches northward, the recovery phase begins. A further effect, not covered in detail here, is that of geomagnetic substorms. These bursts of storm activity are much more relevant at higher latitudes and are of much shorter time-scales than the main or recovery phases. The drivers of substorms are down-tail processes that include magnetic reconnection. In summary, the solar wind drives convection in the magnetosphere that dissipates in geomagnetic storm processes. This is divided into direct input into the auroral ionosphere, the creation of magnetospheric currents and down-tail processes.

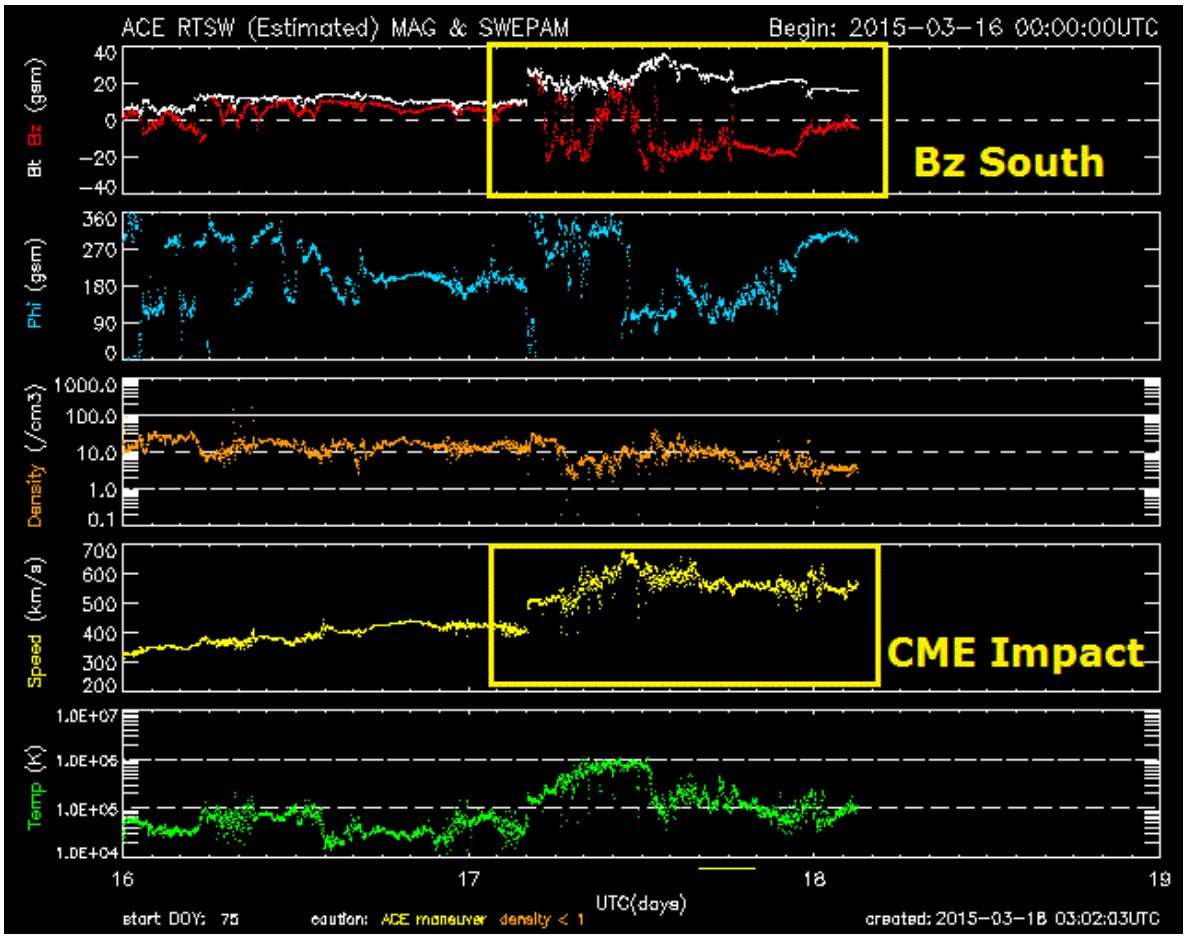

Figure 13: Now replaced by DISCOVR, the ACE satellite was long our probe in the turbulent solar wind, allowing for near-time prediction using upstream measurements - this image is of the St. Patrick's Day Storm, with the onset of the CME indicated by the increased solar wind speed and the change in the IMF from northward to southward (B_z component) [Image credit: `http://www.solarham.net/` [56]].

Given all the theory, we have a number of satellites and observatories that are dedicated to monitoring the Sun and making in-situ solar wind measurements. One of the first satellite missions was Wind, launched in 1994. Situated at the L1 Lagrangian point between the Earth and the Sun, it sends back information regarding radio waves and plasma in the solar wind. In 1997, this was supplemented by the Advanced Composition Explorer (ACE) satellite (see Figure 13). Even more advanced than the previous two missions is the Deep Space Climate Observatory (DSCOVR), which was launched in 2015.

Moving away from the solar wind and looking at the Sun itself is the SOHO satellite. The SOHO mission is aimed at monitoring the solar atmosphere for research and space weather prediction

purposes. An example of this is Figure 14, where the different images of solar events leading up to the Halloween Storm of 2003 are as follows [39]:

- Orange: visible light image by the Michelson Doppler Imager (MDI) of the solar disc showing the sunspot group that produced the solar eruption.
- Green: ultraviolet image by the Extreme ultraviolet Imaging Telescope (EIT) of the Sun including a bright flash from the X17 solar flare.
- Red: LASCO/C2 coronagraph (with an artificial eclipse) showing the CME.
- Blue: LASCO/C3 coronagraph (with an artificial eclipse) showing a further out view of the CME.

In 2010, the Solar Dynamics Observatory (SDO) supplemented SOHO with more modern instruments and improved measurements.

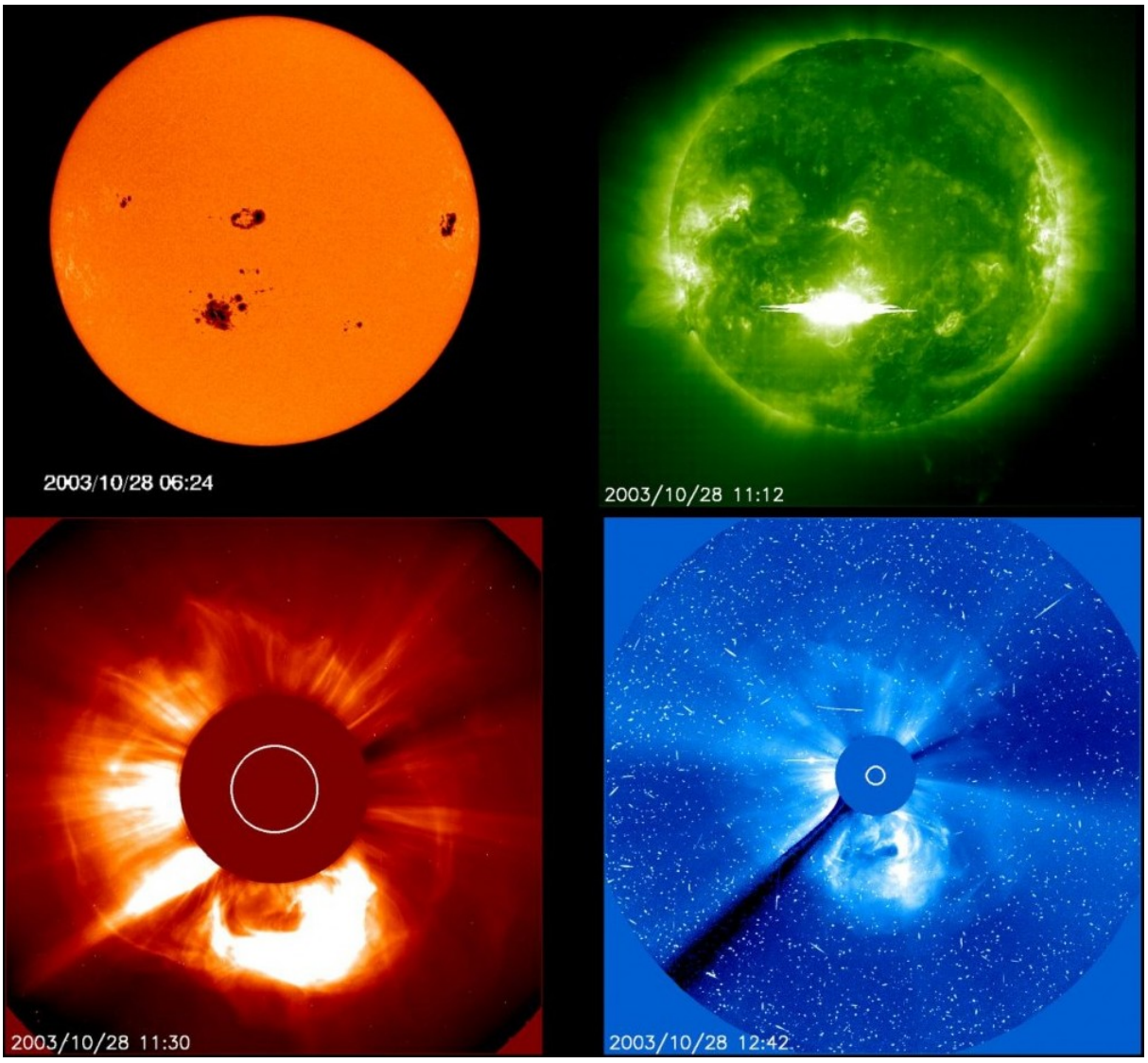

Figure 14: Images from different instruments on the Solar and Heliospheric Observatory (SOHO) satellite of the events on the Sun relating to the Halloween Storm of 2003 [Image credit: `http://www.thesuntoday.org/` [39]].

Another vitally important mission for space weather prediction is the STEREO (Solar Terrestrial Relations Observatory) mission. This mission consists of two nearly identical spacecraft that allow for

stereoscopic imaging of the Sun. This gives a three dimensional interpretation of solar phenomenon such as CMEs, which is then used in models such as the WSA-ENLIL solar wind prediction model (see Figure 15). Ultimately, using predicted and in-situ solar wind data can allow for a GIC prediction model and mitigation scheme [34].

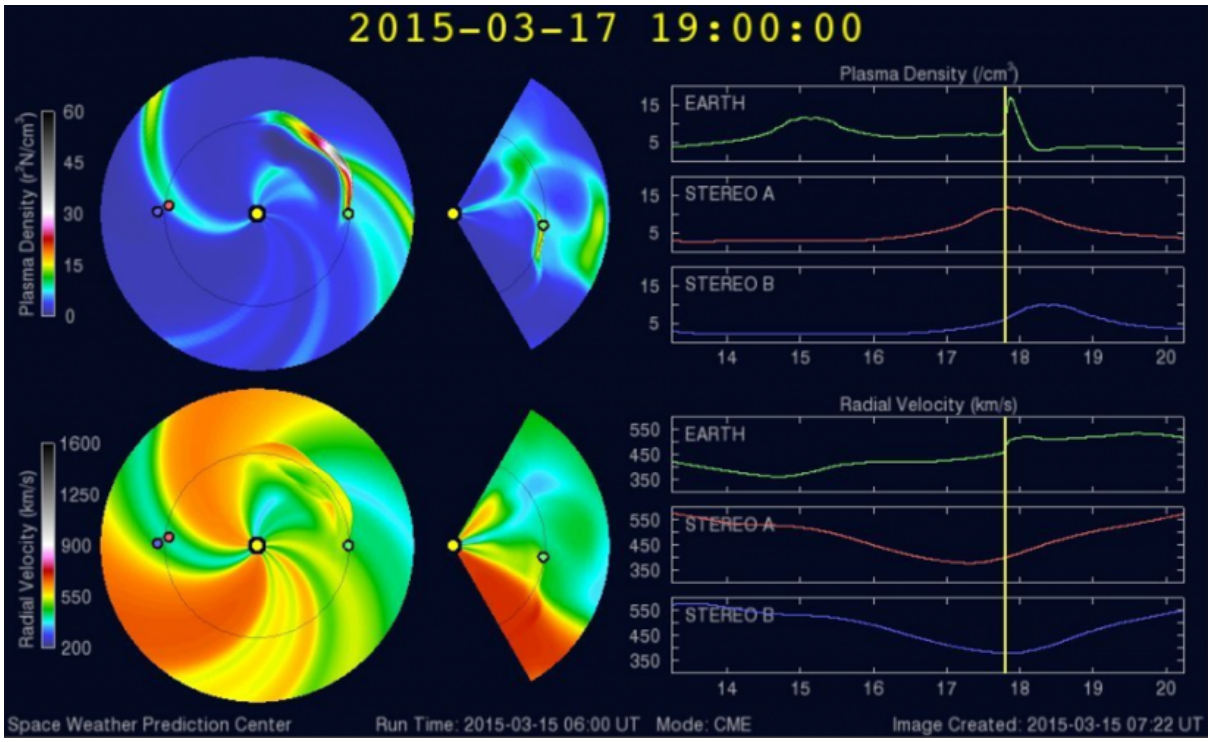

Figure 15: One of the big advances in prediction is the WSA-ENLIL model that propagates CME characteristics immediately after an active region erupts - this image is taken of the St. Patrick's Day Storm prediction, more than two days before the true CME arrived [Image credit: `http://www.swpc.noaa.gov/` [44]].

1.2 GICs and the Power Network

Although any large grounded conductor networks are susceptible to GICs, in this work we restrict ourselves to power networks. In modern times, society has become more and more dependent on electrical power, and by default, the associated networks. The effects of GICs in these networks can be particularly damaging and costly [8, 37], especially in high latitude regions. Lesser, but still significant effects have also been observed at mid-latitudes [31, 24, 21]. Given a large enough event now, such as the Carrington event of 1859, the direct and knock-on results can be absolutely devastating. Such an event is more than just a possibility, it is just a matter of time [54]. With this in mind, the study and modelling of the effects of GICs has become essential to ensure the future security of society in general.

The total adverse effect of GICs on transformers and the power network is generally a combination of different effects. These can be summarised in broad brush strokes as:

1. Transformer (half-cycle) saturation:

   Saturation can probably be thought of as the main driver of adverse effects in power networks resulting from GICs. In a transformer, there is a ferromagnetic core with high permeability. This core is needed to provide a low-reluctance path for the magnetic flux generated by the windings of the transformer. In normal operation, most of the flux is confined to this core

and there is linear relationship between the magnetising current and the magnetic flux. As magnetic flux increases, there is a point where saturation is reached and the linear relationship breaks down [40]. Also needed is an excitation current which energises the core and overcomes internal loss. During normal operation, this excitation current is very small. For efficiency purposes transformers are designed to operate near the saturation point. In the case of quasi-DC GICs, even low values could push the core into saturation [26]. Since the phenomenon is quasi-DC, saturation occurs for half an AC cycle, hence the term half-cycle saturation. When a core goes into saturation, the path for the magnetic flux has a higher reluctance (permeability tends to 1) and requires more current to generate the same amount of magnetic flux. This in turn means a larger excitation current is needed, which in turn results in higher reactive power demands and more harmonics [65]. Under these conditions, transformers become reactive power sinks and sources of harmonic currents [29]. In terms of the network, this results unusual power flows, voltage fluctuations, frequency shifts and protective system malfunctions [1]. Ultimately, half-cycle saturation caused by GICs in transformer windings rapidly accelerates degradation of the transformer (and in extreme cases total failure) [21]. Evidence of this is seen in transformer heating and gas formation [2].

2. Heating and gas formation:

   One of the effects of half-cycle saturation is the leakage of excess flux [2]. The excess flux tries to find alternative paths to the core, such as the tank wall, flux shields, clamps and other structural members of the transformer [29]. Eddy currents from this stray flux can cause rapid and excessive heating in the transformer. An implication of this is the degradation of winding insulation, which decreases efficiency and degrades the transformer. In extreme cases, there can even be a meltdown of the transformer itself. A second implication is that an intense hot spot may generate a free gas bubble in the oil [3]. Such a gas bubble leads to dielectric breakdown and sparking. The effects of this can be seen in dissolved gas-in-oil analysis (DGA) tests. These tests are used to assess the internal condition of transformers. The localised overheating produced by leakage flux would be evident in these tests [30]. The results of the DGA analysis has further linked GICs to transformer damage and failure in severe geomagnetic storms, as well as demonstrating the accelerated degradation and shorted lifetime caused by less severe storms [21].

3. Harmonics:

   During transformer saturation, the exciting current generates harmonic components. The asymmetry caused by the DC offset leads to both odd and even harmonics [40]. The magnitude of these harmonics generally decreases with increasing order at a given current magnitude [65]. When these harmonics go above the design thresholds they can cause increased I^2R power losses (decreased efficiency) and heating in transformers and tripping in the network [3].

4. Protective relay tripping:

   When a large amount of harmonic distortion is introduced into the network by transformer response to GICs, conventional protection systems are often inadequate [29]. An example of this is in distance relays. Half-cycle saturation can in this case reduce the apparent impedance seen by the relay and if this is within the operating zone of the relay, false tripping may occur [26]. Reactive power compensators, such as shunt capacitors, have neutral overcurrent relays which are tripped by harmonics. Transformer overcurrent relays can also be false tripped by triplen harmonics (odd multiples of the 3rd harmonic which can lead to large currents in the neutral) [40]. Furthermore, undervoltage relays can trip due to depressed voltages due to saturation caused voltage fluctuations [26]. In the Hydro-Québec blackout of 1989, 7 reactive

power compensating overcurrent relays tripped [26].

A case study of how multiple effects at multiple parts of the network can lead to disaster is the 1989 Hydro-Québec blackout that resulted from a severe geomagnetic storm. In this case the tripping protective relays which were shorted by harmonics coincided with a build-up of reactive power. The combination of these particular effects resulted in the collapse of the entire network in less than 2 minutes, leading to a 12 hour blackout that affected millions of people [5].

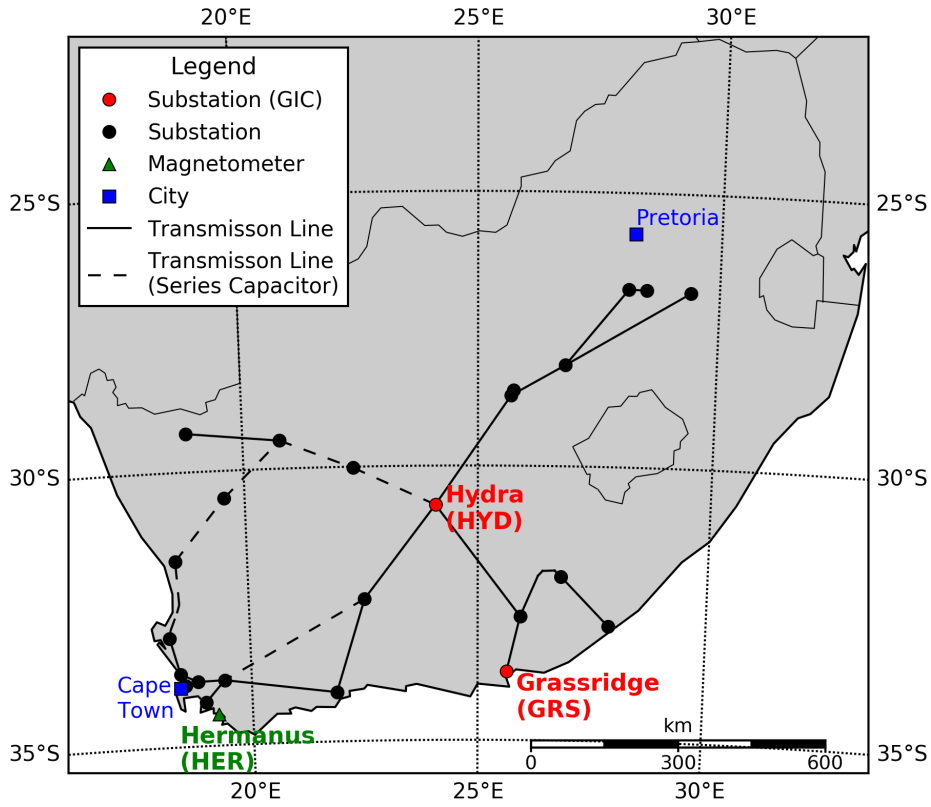

Figure 16: Map of the relevant portion of the South African 400 kV power network between 2000 and 2005. It should be noted that not the entire network is needed to model the GICs in the network - GICs flow from site to site and the only relevant transmission lines and substations are those within a few hundred kilometres of where the GIC is measured [59]. Transmission lines with series capacitors do not contribute to the measured GIC since capacitors effectively block the quasi-DC GIC [21].

1.3 GIC Modelling

Modelling GICs entails not just modelling a single system, but rather modelling a chain of coupled systems. In previous sections, the large-scale drivers and subsequent effects of GICs were unpacked. Of the different GIC drivers, a geomagnetic storm is generally associated with the most intense GICs. Taking this into account, we can look into the specific mechanism that actually drives GICs. During a geomagnetic storm, the near-Earth current systems are significantly disrupted. Linked to the current systems is the system defined by the power network on Earth where GICs ultimately occur. It is the interaction between these two systems that ultimately drives the GICs. At this point, it should be noted that previous work has emphasised entire network modelling, which is not done in the current work. Such modelling is just an extension of the theory and results presented here.

Before getting into the mechanism behind GICs, let us define a few governing assumptions made in typical GIC modelling. Firstly, it is assumed that the induced geoelectric field is driven by a plane-wave geomagnetic field over the system (spatially constant) for a snapshot in time [48]. Such an

induced geoelectric field would be uniform if the conductivity of Earth is dependent only on depth (laterally constant). In this work, we will refer to this collection of assumptions as the plane-wave assumption. A plane-wave geomagnetic field can result from a number of cases. One would be a very long (relative to the system) uniform sheet or line current. Another would be a very distant point source. These are idealised cases which can be thought of first order approximations to real current systems, but in general, a plane-wave geomagnetic field is an oddity [11]. In reality, the ionospheric current systems are exceptionally complex, non-uniform and highly variable. However, at mid-latitudes the plane-wave geomagnetic field assumption is not too bad. Here, the assumption is much more relevant than in auroral regions where the auroral electrojet is the dominant current system. This current system is more variable and closer compared to the mid-latitude drivers, making the interactions more complicated [10, 24, 25, 67, 71, 18].

There are a number of subtle points when it comes to what actually drives GICs. A well-known result of Faraday's Law of Induction is that the rate of change of magnetic flux through a closed path induces an electric field and electromotive force (EMF) that can drive a current around the path. Probably most recognisable in its differential form,

$$\nabla \times \vec{E} = -\frac{\partial \vec{B}}{\partial t}, \tag{3}$$

the integral form is what is of interest in this case and defines the EMF,

$$\oint \vec{E} \cdot \vec{dl} = -\frac{d\Phi_B}{dt} = EMF, \tag{4}$$

where Φ_B is the magnetic flux through the closed path as defined by the integral. This mathematical result is incredibly useful in calculations. Furthering on this, Lenz's Law (a result of the conservation of energy) states that the direction of this induced current would be such that the magnetic field induced by the current opposes the initial magnetic field. This in a nutshell is what drives the GIC. The details of this are not as simple. A common mistake is to assume the closed path (induction loop) is formed by the transmission line a few metres above the Earth's surface, its grounding connections and the return path along the Earth's surface. This integral is essentially zero - the slow variation of the geomagnetic field requires a much larger loop to drive the measured GIC [11]. A quick calculation shows this. Firstly, let us take a typical variation in the geomagnetic field to be around 2 nT/min. This is in fact the typical rate of change in the magnetic field over South Africa in the initial phase of the 2015 St. Patrick's Day geomagnetic storm (see Figure 17). Assuming a transmission line of 100 km being 10 m off the ground, the induction loop would have an area of $A = 10^6$ m^2. Considering this loop we have the resulting EMF voltage,

$$\begin{aligned} EMF &= -\frac{\Delta BA}{\Delta t} \\ &= -\frac{2 \times 10^{-9} \times 10^6}{60} \approx 0.33 \times 10^{-4} \text{ V}. \end{aligned} \tag{5}$$

If we assume the typical transmission line has a resistance of 0.03 Ω per 1 km [38], then a 100 km line would have a resistance of 3 Ω. Taking this as the only resistance (Earth's resistance is negligible as is shown later) we can use Ohm's Law, $V = IR$, to get the current in this loop produced by the EMF,

$$\begin{aligned} I &= \frac{V}{R} \\ &= \frac{0.33 \times 10^{-4}}{3} \approx 10^{-5} \text{ A}. \end{aligned} \tag{6}$$

Typical values for measured GICs in the South African power network for similar cases are of the order of a couple of amperes [29, 21, 4]. This suggests that the induction loop chosen simply is not correct.

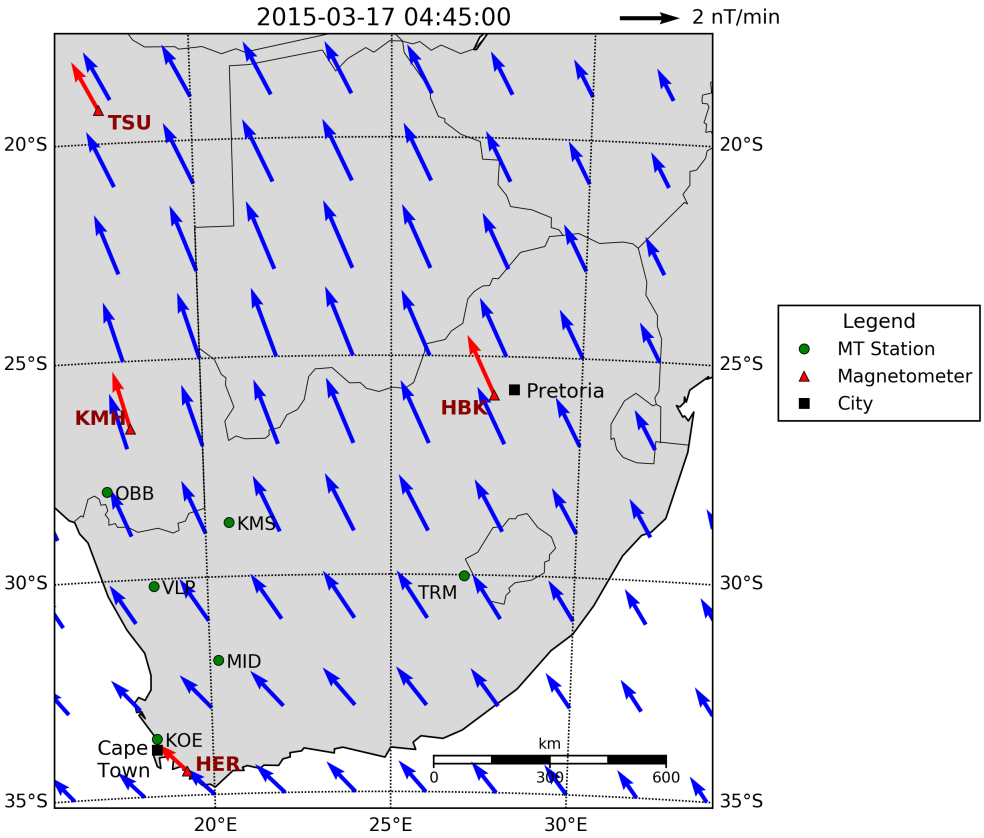

Figure 17: A plot of the typical geomagnetic field fluctuations over South Africa in the initial phase of the 2015 St. Patrick's Day geomagnetic storm. This plot was generated by interpolating geomagnetic field data from the different magnetometers in South Africa using SECS (Spherical Elementary Current Systems) interpolation [63, 4, 42, 36].

At this point, it pays to look into the nature of the EMF as well. As with the abstraction of fields, which we can only 'measure' by observing interactions and that allow us to very accurately describe the physical world, so the EMF is also an abstraction. Although the name includes the term 'force', the EMF is in fact not a force at all. The EMF instead drives a current as a result of the fluctuating magnetic field as defined by Faraday's Law. This extra generated or induced voltage (energy per unit charge) is different form the typical charge distribution or battery related voltages as the zero-potential can be defined anywhere in the induction loop. When dealing with an EMF, the entire loop has to be taken into account as it is only defined for that particular system. In the case of GICs, the voltage difference seen between grounding points is a result of the EMF induced current and the resistance of the transmission line and not because of a charge difference on the surface. A common misconception is that this voltage difference is what drives the GIC (rather, it is purely an effect). This mistaken assumption of a potential gradient on the surface of Earth has led to GIC modelling by approximating voltage sources at grounding points that drive GICs from the Earth into the network. This does in fact produce accurate results assuming a uniform induced geoelectric field, but for the wrong reasons.

What is not always appreciated, is that the induction loop relevant to GICs extends deep into the Earth. This is illustrated by the back-of-an-envelope calculation presented above - in order to get the right order of magnitude using the same example and assuming a magnetic field that is not attenuated

by the Earth, the depth of loop should not only be 10 m, but rather 1000 km. Such a typical loop (ABCD) is shown in Figure 18. Considering the broader range of magnetic field variations relevant to GICs, the induction loop becomes even more important. These variations span frequency range from 10^{-5} to 1 Hz. Frequencies lower than this are too slow to produce significant GICs. On the other hand, power system inductances have a damping effect on higher frequencies, just as capacitance damps low frequencies [11].

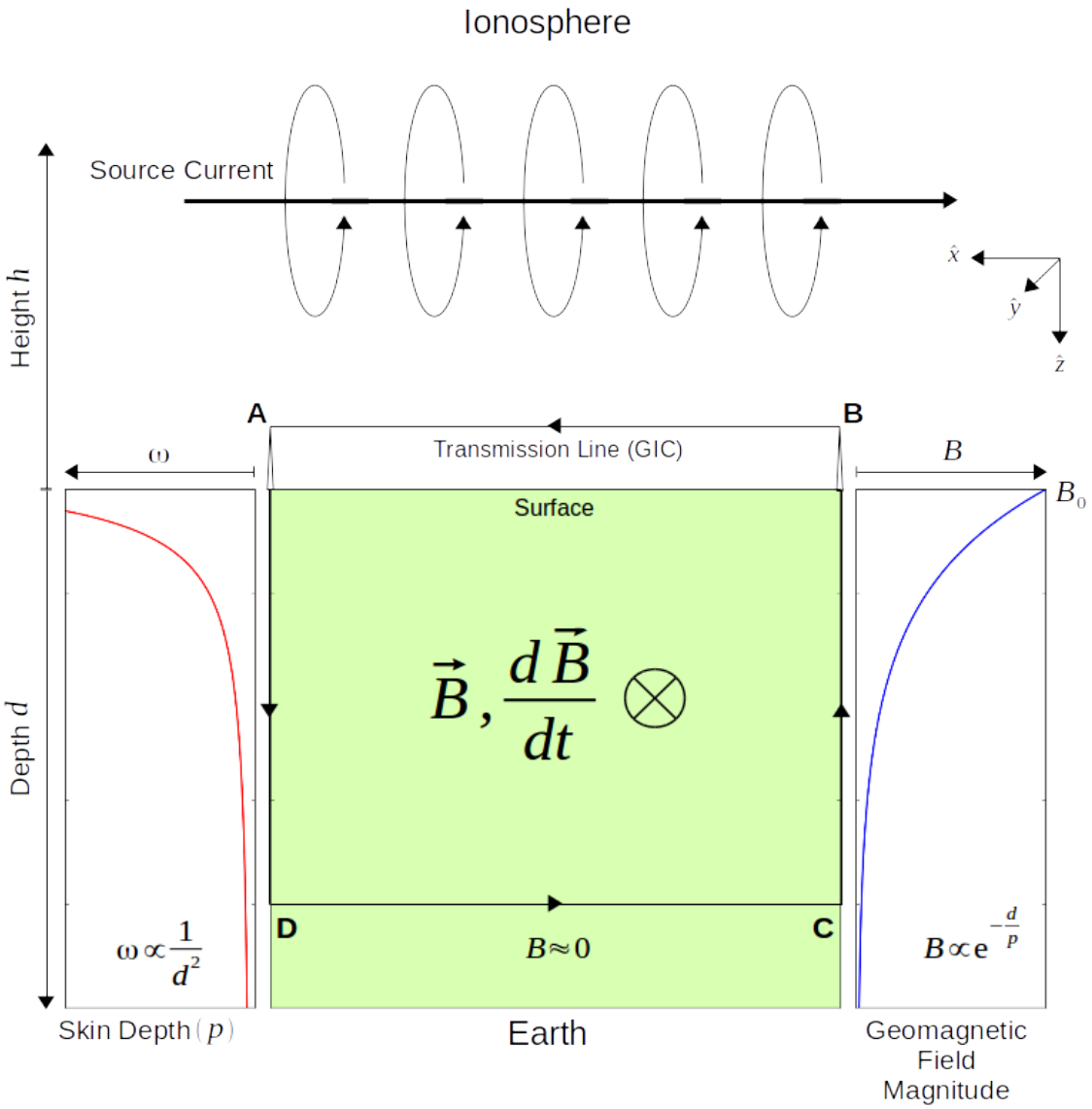

Figure 18: A diagram showing the various components relevant to driving GICs in a power network.

At this point it should be pointed out that due to the very low conductivity of air ($\approx 10^{-14}$ S/m), there is no galvanic connection between the Earth, ionospheric and magnetospheric currents [52]. This essentially means that the currents in the Earth are purely from induction and that the associated induction loops would not include the air. Now, with the correct induction loop for driving GICs identified, we can look further into the theory involved. For this we will use the incredibly simplified system as defined in Figure 18, where a very long line current in the ionosphere (moving to the right and aligned with a grounded transmission line) results in a magnetic field (into the page). In this case, we assume the magnetic field is increasing in magnitude (also into the page). By Lenz's Law, the direction of the induced current in the ABCD induction loop would be anti-clockwise. In this system, we assume a homogeneous Earth with conductivity σ, which would have a typical value

of 0.001 S/m (resistivity of $\rho = 1000$ Ω·m). The choice of a line current source is arbitrary, as it could also be a uniform sheet current or distant source. The main requirement is that the magnetic field produced is uniform and in the case of a radiated electromagnetic wave propagating from the source, vertically incident to the surface of the Earth. Typically, this is known as a plane-wave. It should also be noted that it is not the magnetic field itself which drives the GIC, but the magnetic field fluctuations. This means we generally ignore the 'constant' dipole field of the Earth, which acts as a baseline for the magnetic field from the ionospheric current. Together, these result in the geomagnetic field. Furthermore, the magnetometer at the surface of the Earth would also be measuring the induced magnetic field from the induced currents in the Earth, which in effect scales the ionospheric/magnetospheric driven magnetic field [52]. In GIC modelling, we are not concerned about the source of these fields but rather just the nett fluctuations. That said, let the measured magnetic field from the ionospheric current source at the surface in this case be B_0.

There are two interpretations of the driving magnetic field. As mentioned, either we can consider the magnetic field to be just that - a magnetic field (produced from something like a line current), or we can consider the magnetic field as a component of an electromagnetic wave that is radiated by some distant changing current source. The second interpretation means we can treat the magnetic and electric fields as components of an electromagnetic wave that propagates vertically down. This simplifies the system immensely and we will consider it first. Firstly, it is expected (as with all electromagnetic waves in matter) that the vertically incident uniform electromagnetic would be attenuated by the Earth. Assuming this magnetic field has a frequency ω, the associated penetration would be given by the complex skin depth [11],

$$p = \sqrt{i\omega\mu_0\sigma}, \tag{7}$$

where μ_0 is the permeability of free space and σ is the conductivity of the Earth (assumed in this case to be constant). In this case, we assume that the conductivity is related to the permeability of free space and not some relative permeability of the material. The left plot (red line) in Figure 18 shows the typical relative skin depth for different frequencies (higher frequencies on the left have less penetration than lower frequencies on the right). In the case of a layered Earth model with different conductivity layers (laterally constant) as often used in modelling, the general behaviour would stay the same. In these types of models, the general approach is to iteratively consider each layer, using the lower boundary condition of the previous layer to define the upper boundary condition of the next layer down. For a linear decrease in frequency, there is a quadratic increase in the penetration depth. This feeds into the drop-off of the incident magnetic field B_0, as defined by the skin depth (the skin depth is the depth at which an electromagnetic wave attenuates by $1/e$),

$$B = B_0 e^{-\frac{d}{p}} \tag{8}$$

where d is the depth ($-z$ in Cartesian coordinates) and p is the skin depth. This relative drop-off for a single frequency is shown by the right (blue) plot in Figure 18. The end result is that lower frequency incident magnetic fields penetrate deeper into the Earth and are attenuated less. These lower frequency magnetic fields dominate when considering GIC drivers, but there is a cut-off where the fluctuations associated with the low frequency fields are just too slow. Ultimately though, with any frequency considered, the electromagnetic components will tend to zero at a significant depth. A further result of the electromagnetic wave interpretation that will be used later is that the magnetic and electric fields are purely horizontal (since the propagation is vertically downwards). This means that in the case of the magnetic field being in the y direction, then the associated electric field would be in the x direction, since $\hat{E} \times \hat{B} = \hat{k} = \hat{x} \times \hat{y} = \hat{z}$.

Assuming some effective depth, which takes into account the frequency and area considerations, the 'return' path of the GIC current will be spread from the surface to this depth. This spreading of

the 'return' path is furthermore three dimensional, meaning that the volume needs to be taken into account and not only the depth. General conductivity modelling assumes layers infinite in lateral extent when compared to the system. This has a direct effect on the effective Earth related resistance experienced by the EMF generated current. Taking a typical homogeneous Earth with a resistivity of $\rho = 1000$ Ω·m, we can find the typical resistance through the relation $R = \rho l/A$, where A is the cross-sectional area and l is the length. Although the length of the transmission line increases the effective resistance the area (depth multiplied by lateral extent which is assumed to be much greater than the system size) dominates. Another interpretation of this is to model the resistance associated with the Earth by approximating many parallel resistors to represent the different paths, each resistor having its own defined $R = \rho l/A$. Assuming each is defined so that their resistances are the same, the effective resistance would be $R_{eff} = R/N$, where N is the number of resistors. The more 'paths', the less resistance. Ultimately, these two results mean that the effective resistance of a homogeneous Earth is negligible when compared to the resistance of the transmission line. For a realistic model of the Earth's conductivity, the effective resistance is even smaller since conductivity increases with depth.

Taking a step back, let us consider the alternate interpretation of the driving magnetic field, i.e. purely a magnetic field from a line current. For this we consider the differential form of Maxwell's equations and apply them to the magnetic field purely in the y direction. Specifically, let us consider Faraday's Law as defined in equation (3), and Ampere's Law,

$$\nabla \times \vec{B} = \mu_0 \vec{J} + \mu_0 \epsilon_0 \frac{\partial \vec{E}}{\partial t}, \tag{9}$$

where $\vec{J}$ is the current density and ϵ_0 is the permittivity of free space. Taking the curl of equation (3), we get,

$$\nabla \times \left(\nabla \times \vec{E}\right) = -\frac{\partial}{\partial t}\left(\nabla \times \vec{B}\right). \tag{10}$$

Substituting Ohm's Law as defined in physics, $\vec{J} = \sigma \vec{E}$, and equation (9) into equation (10), we get,

$$\begin{aligned} \nabla(\nabla \cdot \vec{E}) - \nabla^2 \vec{E} &= -\mu_0 \sigma \frac{\partial \vec{E}}{\partial t} - \mu_0 \epsilon_0 \frac{\partial^2 \vec{E}}{\partial t^2}. \\ \nabla^2 \vec{E} &= \nabla(\nabla \cdot \vec{E}) + \mu_0 \sigma \frac{\partial \vec{E}}{\partial t} + \mu_0 \epsilon_0 \frac{\partial^2 \vec{E}}{\partial t^2}. \end{aligned} \tag{11}$$

This equation can be updated by introducing a dimensionless parameter $t' = t/T$, where T is some characteristic time that defines the phenomenon [52]. Substituting this into equation (11) results in,

$$\nabla^2 \vec{E} = \nabla(\nabla \cdot \vec{E}) + \frac{\mu_0 \sigma}{T} \frac{\partial \vec{E}}{\partial t'} + \frac{\mu_0 \epsilon_0}{T^2} \frac{\partial^2 \vec{E}}{\partial t'^2}. \tag{12}$$

Relating the coefficients in second and third terms of equation (12) and using a typical lower bound on conductivity being of the order 10^{-5} S/m and lower bound on the characteristic time being of the order of 1 s (frequency of 1 Hz), we have the $\mu_0 \sigma/T \gg \mu_0 \epsilon_0/T^2$ since $\epsilon_0 = 8.85 \times 10^{-}12$ F/m. Any higher conductivity or lower time period would result in an even greater inequality. Following from this, for the given system (geomagnetic fluctuations) the third term can be neglected. This quasi-static approximation is equivalent to neglecting the last term (displacement current) in equation (9), i.e.,

$$\nabla \times \vec{B} = \mu_0 \vec{J}. \tag{13}$$

Taking the divergence of the quasi-static approximation of Ampere's Law, we see that $\nabla \cdot \vec{J} = 0$ (divergence of a curl is always zero). Physically, this means that the current induced in the Earth by geomagnetic fluctuations is divergence-free. Applying this condition to Ohm's Law, we have,

$$\nabla \cdot \vec{J} = \nabla \cdot \sigma \vec{E} = (\nabla \sigma) \cdot \vec{E} + \sigma \nabla \cdot \vec{E} = 0. \tag{14}$$

From this, the divergence of the electric field can be written as,

$$\nabla \cdot \vec{E} = -\frac{(\nabla \sigma) \cdot \vec{E}}{\sigma}. \tag{15}$$

Substituting this expression into equation (12), we obtain the seemingly complex result,

$$\nabla^2 \vec{E} = -\nabla \left(\frac{(\nabla \sigma) \cdot \vec{E}}{\sigma} \right) + \mu_0 \sigma \frac{\partial \vec{E}}{\partial t} \tag{16}$$

This equation can be simplified considerably by restricting ourselves to either a homogeneous or layered Earth model. In such models the conductivity gradients can be neglected since the conductivity is uniform in each 'layer' and each layer is considered separately. The result of such an assumption is the diffusion equation,

$$\nabla^2 \vec{E} = \mu_0 \sigma \frac{\partial \vec{E}}{\partial t}. \tag{17}$$

Similarly, it can be shown that the magnetic field $\vec{B}$ results in a diffusion equation. Taking the curl of equation (13) and substituting first Ohm's Law and then Faraday's Law into the result, we get,

$$\nabla \left(\nabla \cdot \vec{B} \right) - \nabla^2 \vec{B} = \mu_0 \left(\nabla \times \vec{J} \right) \tag{18}$$

$$\nabla^2 \vec{B} - \nabla \left(\nabla \cdot \vec{B} \right) = -\mu_0 \sigma \left(\nabla \times \vec{E} \right) \tag{19}$$

$$= \mu_0 \sigma \frac{\partial \vec{B}}{\partial t}. \tag{20}$$

Since magnetic fields are always divergence-free (no monopoles), this equation becomes,

$$\nabla^2 \vec{B} = \mu_0 \sigma \frac{\partial \vec{B}}{\partial t}. \tag{21}$$

The implication of this is that the incident magnetic field and its induced electric field diffuse through the Earth. From this, we can derive the appropriate boundary conditions and apply the standard techniques of using an induction loop to calculate the EMF. The first boundary condition to take into account is that the magnitude of the magnetic and induced electric fields must tend to 0 as z tends to $-\infty$ (very deep and very far away from the line current source). This result from the diffusion equation holds up with the penetration depth argument presented earlier in the electromagnetic wave interpretation. Additionally, it is expected that there is no vertical component of the magnetic field (as defined) and that the system is aligned in such a way that the magnetic field only has a y component. The induced electric field would always be perpendicular to this magnetic field (i.e. in

the xz-plane). At the surface, an additional boundary condition on the electric and magnetic field can be applied. Here, the magnetic field would have the defined magnitude B_0 in the y direction as defined by the system. The electric field on the other hand has to satisfy the divergence-free condition on the current density. This implies that at the surface,

$$\begin{aligned} \vec{J}_{above} \cdot \hat{n} &= \vec{J}_{below} \cdot \hat{n} \\ \sigma_{above}\vec{E}_{above} \cdot \hat{n} &= \sigma_{below}\vec{E}_{below} \cdot \hat{n} \\ \sigma_{above}\vec{E}_0 \cdot \hat{n} &= \sigma_{below}\vec{E}_0 \cdot \hat{n} \end{aligned} \tag{22}$$

where $\hat{n}$ is the unit normal vector to the surface (z direction) and $\vec{E}_0$ is the induced geoelectric field at the surface. σ_{above} in this case is the conductivity of air and is approximately zero. σ_{below} on the other hand is significant larger and non-zero. This means that the surface of Earth, the vertical component of the induced electric field is assumed to be zero as well. Applying this approach iteratively in the case of a layered Earth (only depth dependent conductivity), at the interface between each layer the same condition holds (the effect of different conductivities can only be balanced with a zero electric field) until finally at the deepest layer the second boundary condition that the magnitude of the fields is approximately zero applies. The result of this is that the vertical component (z direction) of the induced electric field is always zero. Although the induced electric field in the xz-plane, only the horizontal component in the x direction is non-zero. In summary, the diffusive nature of the fields in the Earth leads to horizontal magnetic and electric fields. Considering Figure 18, the magnetic field has an initial magnitude B_0 in the y direction at the surface, and falls away to zero at a significant depth. The associated induced electric field has an initial magnitude of E_0 in the x direction at the surface, and also falls away to zero at a significant depth. This is consistent with the electromagnetic wave interpretation of the fields.

With the nature of the fields in the Earth defined, we can apply Faraday's Law of Induction to the system. We have already shown that the induction loop to consider is much deeper than often thought. Bearing in mind that the integral form of Faraday's Law is essentially an application of Stoke's Theorem, which states that if the boundary path is split into two separate closed paths, any interior path segments are in opposite directions and their contributions to the total path integral cancel. When applied to the system in Figure 18, the boundary path defined by ABCD is the same as considering the two paths AB-surface and CD-surface. As already shown, the integral defined by the AB-surface loop is essentially zero and the main contribution to the ABCD path integral comes from the CD-surface loop. Alternately stated, the EMF produced by the AB-surface induction loop is essentially zero when compared to the CD-surface induction loop. This is a result of the relative areas. Taking the idealised example of a 10 m high and 100 km long transmission line, we saw that the required induction loop stretches down to roughly 1000 km. This does not take into account the drop-off of the field magnitudes with depth, so in actual fact the depth required is even greater. Even so, in this scenario the relative areas are 10^6 m^2 for the AB-surface loop and 10^{11} m^2 for the CD-surface loop. The result of this is that the EMF produced by the ABCD loop and drives the GIC is effectively exactly the same as the EMF produced by the CD-surface loop. With that in mind, we can use the nature of the fields in the Earth to find the EMF, i.e.,

$$\begin{aligned} EMF &= -\oint \vec{E} \cdot dl \\ &= -\Big(E_x(z=0) \cdot dl_{AB} + E_z \cdot dl_{BC} + E_x(z \to \infty) \cdot dl_{CD} + E_z \cdot dl_{DA}\Big) \\ &= -E_x(z=0) \cdot dl_{AB} \\ &= -E_0 L, \end{aligned} \tag{23}$$

where L is the length of the transmission line. This result is due to the conditions derived earlier, i.e. the induced geoelectric field is always horizontal ($E_z = 0$) and at a significant depth the fields are approximately zero (field magnitude decreases exponentially with depth). The resulting relation in this case means the EMF produced by the induction loop ABCD (which is the same as the CD-surface loop) effectively comes from the induced electric field as the surface. After taking into account the circuit resistances, the current produced can be linearly related to the induced geoelectric field at the surface through the EMF (which in effect is the often used governing equation for GICs). This means that if you know the induced geoelectric field at the surface, you can calculate the associated EMF and scale appropriately to get the induced current.

At this point it should be emphasised that the induced electric field at the surface, often referred to as the geoelectric field is purely an induced field related to fluctuations in the measured geomagnetic field. This means that it is not the total electric field, but rather a specific component of the total electric field. That said, it is this component that is relevant in the induction calculations. This geoelectric field is a mathematical result that links the measured geomagnetic field to the induced current. It is in fact not measured explicitly. Instead of deriving the geoelectric field by giving the system the full treatment as presented, a number of assumptions can be used to directly relate the geomagnetic and induced geoelectric fields. Assuming that the magnetic and electric fields have typical harmonic variations of the form,

$$E = E_0 e^{i(\omega t - kz)} \qquad \text{and} \qquad B = B_0 e^{i(\omega t - kz)}, \tag{24}$$

and a homogeneous Earth with conductivity σ, then we can update the diffusion equations to,

$$\nabla^2 \vec{E} = i\omega\mu_0\sigma\vec{E} \qquad \text{and} \qquad \nabla^2 \vec{B} = i\omega\mu_0\sigma\vec{B}. \tag{25}$$

As noted, the solutions to these equations are decaying exponentials of the form $e^{-z/p}$, where p is the complex skin depth. Substituting this result back into the differential form of Faraday's Law (or the quasi-static approximation of Ampere's Law) gives,

$$\begin{aligned} \frac{dE_x}{dz} &= -i\omega B_y \\ -\frac{E_0}{p} &= -i\omega B_0 \\ \therefore \frac{E_0}{B_0} &= i\omega p = \sqrt{\frac{i\omega}{\mu_0\sigma}}. \end{aligned} \tag{26}$$

In the case of a similar system defined in such a way that the geomagnetic field is in the x direction and still vertically incident, then the geoelectric field must be in the $-y$ direction. In such a coordinate system, the minus sign is included in the relation between the two orthogonal components. The general relation between the orthogonal components of the geomagnetic and geoelectric field is usually written as the magnetotelluric surface impedance Z [12], where,

$$Z = \frac{1}{\mu 0}\frac{E_x}{B_y} = -\frac{1}{\mu 0}\frac{E_y}{B_x}. \tag{27}$$

A more complex version of this relation (not just a homogeneous Earth and with a range of relevant frequencies) is used to derive the geoelectric field in Section 4.2. Again, it must be emphasised that this derived geoelectric field is the induced electric field as defined by the system.

Up to now, we have only considered the very idealised and specific case as defined by Figure 18. This system is representative of the driving mechanism and can be extended to other cases by conveniently choosing a coordinate system that aligns to the transmission line or only considering the

projection onto the coordinate system defined by the transmission line. A second point is that we have considered magnitude fluctuations in the geomagnetic field and specifically only an increasing geomagnetic field. In the case of a decreasing geomagnetic field, the induced current will flow clock-wise by Lenz's Law. The induced geoelectric field will match this and the result is that the defined system holds for normal GIC modelling. When a geomagnetic field changes spatially, the projection of this change in relation to the induction loop would need to be taken into account, but the resultant induced geoelectric field would still respond in the same way. Given such simple systems, which produce uniform geoelectric fields on the surface of the Earth, the modelling of GICs is relatively straight forward. Since a uniform field is conservative, the Gradient Theorem applies. The result of this is that the integral along a path is dependent only on the endpoints of that path, not the path itself (path independent). In GIC modelling, the dot product of the induced geoelectric field and the line direction is related to the driving EMF and hence the measured GIC (see Section 3.1). In order to estimate the total driving EMF, the dot product of the geoelectric field and the transmission line has to be integrated along the transmission line. Since in this case only the endpoints are relevant, integration is not needed and only the absolute distance between the endpoints or nodes needs to be considered. This is one of the reasons modelling GICs as if there were voltage sources at the grounding points works with a uniform field. Furthermore, since the field is uniform, the endpoints have the same geoelectric field associated with them. This means that the geoelectric field only has to be derived at one of the nodes (see Section 3.1).

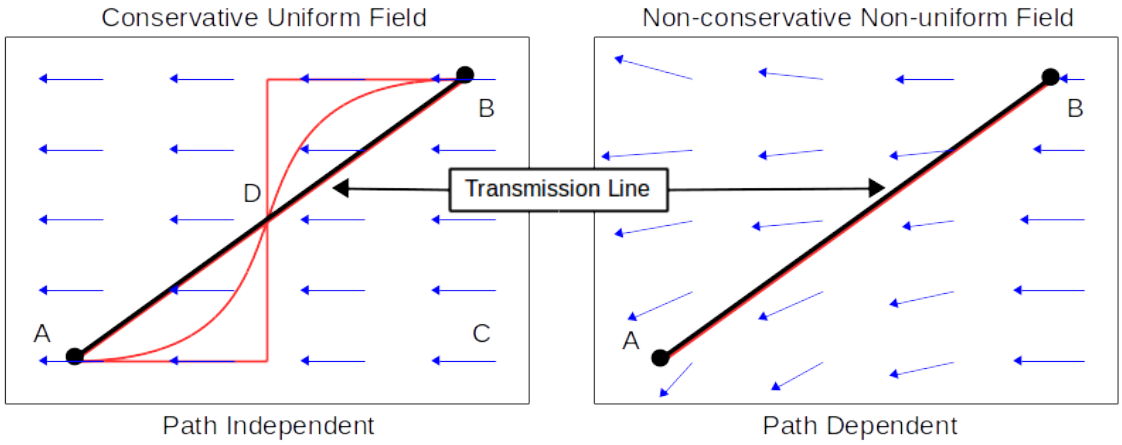

Figure 19: When considering a uniform versus a non-uniform induced geoelectric field (blue), different approaches are needed to calculate the resulting GIC since the former is path independent and the latter is path dependent. In the case of a conservative field (left), the line integral as defined by paths (red) ACB, ADB and AB (along the transmission line) are all equal. For a non-conservative field (right), the only valid line integral is the path AB (red) along the actual transmission line.

In the case of a realistic non-uniform geomagnetic field, then the system is not quite as representative. In the case of a real world non-linear current system, a typical example is when the rate of change of the geomagnetic field is not in the xy-plane (perhaps as a result of an incidence angle not equal to 90°). In this case the typical curl of the induced electric field would no longer just be in the xz-plane and the field at the surface no longer conservative. In these cases, any line integral is path dependent. Analytically, it is not possible to take into account all these different variables. The best we can do is to define the system in such a way as that locally it represents the typical plane-wave defined system we have used up to now. One way to do this is to choose an appropriate induction loop where the geomagnetic field is roughly uniform along the length. This length would typically be a lot shorter than the system length. Using such a loop, we would need to derive the induced surface geoelectric field valid for that length of transmission line. To model the GIC in this case, the dot product of the geoelectric field and transmission line segment needs to be integrated

along the transmission line. This in effect can be thought of as modelling discreet voltage sources in the transmission lines. Although at mid-latitudes, the uniform geoelectric field is a relevant assumption, a uniform field is still a mathematical oddity and does not represent a realistic field that goes to zero at infinity [7]. Non-uniformity does not only arise from the current source, but also from localised distortion in the Earth's different conductivity layers. A typical example of this is at vertical conductivity profile boundaries. Here a charge distribution accumulates and produces a localised electric field, in addition to the normal induced geoelectric field. A typical example of such a conductivity boundary is at a coastline. A larger (can be of the order of 20%) geoelectric field is measured here, a phenomenon often referred to as the coastal effect [11]. Even with this added complexity, if we model the simple system empirically, many of the perturbations in the modelling chain will be absorbed. An analytical approach is limited in this regard.

Nevertheless, assuming the plane-wave geomagnetic field assumption along with a resulting induced uniform geoelectric field, the GIC in a conductor (not the entire network) can be modelled by equation (28) [60],

$$GIC(t) = aE_x(t) + bE_y(t). \tag{28}$$

This equation is of the same form as Ohm's Law as defined in physics,

$$\vec{J}(t) = \sigma\vec{E}(t). \tag{29}$$

This law is often used in the literature to describe the nature of GICs. In equation (29), $\vec{J}$ is the current density (defined as the current per unit of cross-sectional area), σ is the conductivity of the system and $\vec{E}$ (V/m) is the applied electric field. Conductivity is the reciprocal of resistivity, which is measured in Ω·m, and measured in S/m. It should be emphasised that the resulting form is the same, but the drivers and parameters used to describe the resulting current are different. Ohm's Law in the form of equation (29) implies that the current is driven by the electric field experienced by the conductor, which in this case is the transmission line. Of course, the total electric field at the transmission line includes components other than that defined as the induced geoelectric field. In the case of GICs, it is the induced EMF that drives the current as described above. The induced geoelectric field is the main contributor to this, with the EMF being defined as the projection of the induced geoelectric field onto the transmission line, multiplied by the length of the line (dot product). For now, let us assume that the geoelectric field and the transmission lines are aligned. Using the circuit theory interpretation of Ohm's Law, i.e. $V = IR$, we can relate the two forms. In this case, the current I through the conductor (GIC) is related to the voltage V across the length of the line (EMF) through the resistance of the circuit R. This can be represented by a simple circuit, (see Figure 20).

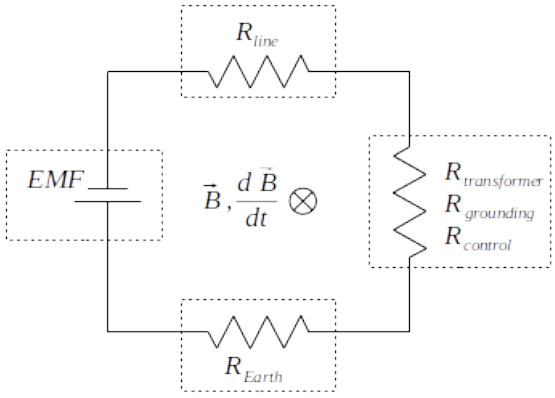

Figure 20: A simple circuit representation of a GIC in the power network.

There are a number of resistances involved in the circuit, the most obvious being the resistance of the Earth and the resistance of the line. As mentioned before, due to the extent of the Earth, the associated effective resistance of Earth is negligible when compared to that of the line, even though the line resistance is very low. In addition to these are network related resistances, which are often greater than the two previously mentioned. These would include the transformer resistances, grounding resistances (from grounding plates and such) and network control resistors. The former two are always present, but the control resistors are not. Although they serve a variety of purposes, they are only used for where needed. An example of such usage is for specific voltage control. That said, all these resistances need to be taken into account when modelling GICs. Grouping these resistances, which are in series, into a single resistance R_{tot}, the resulting GIC in the simple aligned system we have been using would be given by,

$$\begin{aligned} GIC = I &= \frac{V}{R} \\ &= \frac{1}{R_{tot}} EMF \\ &= \frac{1}{R_{tot}} E_0 L \\ &= \frac{L}{R_{tot}} E_0, \end{aligned} \tag{30}$$

where E_0 is the induced geoelectric field (which is roughly the sole contributor to the EMF) and L is the length of the transmission line. At this point, it should also be emphasised that L and R_{tot} are network dependent values. Doing some dimensional analysis on equation (30), we have,

$$\begin{aligned} I = \frac{V}{R} &= \frac{[V]}{[\Omega]} \\ [A] &= \frac{1}{[\Omega]}[V] \\ &= \frac{1}{[\Omega]} \frac{[V]}{[m]}[m] \\ &= \frac{[m]}{[\Omega]} \frac{[V]}{[m]}. \end{aligned} \tag{31}$$

Looking at the last line of both equation (30) and equation (31), we have that the linear relation between the resulting GIC current and the induced geoelectric field is scaled by the network dependent parameters. Specifically, this scaling is defined by the expression L/R_{tot}, which has dimensions of $[m]/[\Omega]$ or alternately $[A][m]/[V]$. This expression can be absorbed into a single network parameter, which in this work we will define as ζ. Compared to Ohm's Law as defined in equation (29), ζ would be defined as the conductivity σ multiplied by the cross-sectional area of the conductor. This discrepancy comes from the fact that the current density is used in equation (29) instead of the actual current. Using the analogy though, ζ can loosely be thought of as a conductivity. Given a more complex system, such as when the induced geoelectric field is not necessarily aligned with the network and directionality needs to be taken into account, ζ would be defined appropriately to take alignment into account.

Now, getting back to the governing GIC equation (28), we have a complex system where the induced geoelectric field is not necessarily aligned to the network and the network itself is not just made up of a simple grounded transmission line. In this case, geoelectric field is defined in Cartesian coordinates which results in a pair of network parameters. These constants, a and b, relate the

magnitude of the GIC flowing in a transformer line to the horizontal components of the induced electric field, defined in this case as the northward (E_x) and eastward (E_y) components. The network parameters in such complex cases have to take into account the entire network, which is significantly more complicated than the simple circuit used to develop the theory. Nevertheless, the analytical methods for estimating the network parameters used in other work do just this [32]. The relating of the induced geoelectric field to the resulting GIC is generally referred to as the 'engineering step' in the modelling process, compared to the 'geophysical step' where the geoelectric field is derived (see Section 4.2). As shown above, these network parameters have the units of A km/V. It should be further noted that they are unique to each node of the power system [60].

Building on the simplified circuit above, there are a number of other factors that affect GICs in power networks, most of which are absorbed into the network parameters. Already mentioned are the resistances of the network [61]. Indirectly though, because of transmission line construction, higher voltage lines have lower resistance and in turn experience the largest GICs. Also related to this is the already mentioned line length, with higher voltage lines generally being used for long distance transmission. The relation derived for the idealistic simple case is misleading though. GIC values in a network scenario have been observed to initially increase with line length but then approach a constant value. When looking deeper into the relations we see that this is entirely expected and can be attributed to the fact that both the driving EMF and line resistance scale with length ($R_t = \frac{\rho l}{A^2}$). Taking into account typical (constant) values for resistivity ρ and cross-sectional area A of the line, the line resistance is of the order of 0.03 Ω/km [38]. Breaking down the total resistance of the circuit into its various components, let us assume the grounding, control and transformer resistances together are of the order of a couple of ohms. We can group these other resistances into a constant resistance R_c of say $\approx 3\Omega$ [30]. Breaking equation (30) into these different terms and assuming a line length of L, we get,

$$\begin{aligned} GIC &= \frac{L}{R_t + R_c} E \\ &= \frac{L}{\frac{\rho L}{A^2} + R_c} E. \end{aligned} \tag{32}$$

If $\frac{\rho L}{A^2} \ll R_c$, then the result would tend to $GIC \approx \frac{E}{R_c} L$ (which linearly increases with length). On the other hand, if $\frac{\rho L}{A^2} \gg R_c$, the result would tend to $GIC \approx \frac{EL}{R_t} = \frac{EA^2}{\rho}$ (which is a constant). This at short line lengths, when the non-line network related resistances dominate, an increase in line length would increase the resulting GIC. In this case, at 100 km the two resistances are comparable and the effect is decreased. At say a couple of thousand kilometres, the line resistance dominates and the resulting GIC no longer changes with line length. Although line length is an important factor, the total system length is more important since GICs typically flow to/from ground through substations at the edge of a network [11]. Small changes in these factors do not seem to change the results of modelling significantly [61]. The other main factor to consider is of course the geoelectric field and the alignment between the field and the network (see Section 3).

1.4 Hypothesis, Research Questions and the Way Forward

As noted above, the network parameters play a crucial role in understanding and modelling GICs in the power network. Following on from this, the hypothesis for this work would be two-fold and defined as:

H1: "Considering an empirically defined set of network parameters would improve the accuracy of GIC modelling during extreme geomagnetic events when compared to previous analytically derived network parameters."

H2: "Network parameters themselves have an intrinsic error associated with them and quantifying this error would improve GIC modelling during extreme geomagnetic events even further."

The research questions related to this two-fold hypothesis would be broadly defined as:

RQ1: What methods can be used to estimate the network parameters empirically from measured data?

RQ2: Do empirically derived network parameters perform better than analytically derived network parameters when modelling extreme events?

RQ3: Could the uncertainty in the network parameters and specifically the error made in the empirical derivation of the network parameters be quantified?

RQ4: What are the drivers of the error in the empirically derived network parameters?

RQ5: When exploring the parameter-space that defines extreme geomagnetic events, do the network parameters and the associated error in them stay constant or are they sensitive to factors such as event intensity?

Some of the research questions are purposefully vague so as not to limit research or be prescriptive (a typical example being RQ5). Throughout this work, reference will be made to the research questions. There may be cases where the research questions are refined though. This would generally happen when the data available limits the extent to which the questions can be explored.

Following on from the defined research questions, the first step is to look into the previous work done. This is relevant to all the research questions and is covered extensively in Section 2. Following on from this, Section 3 covers the theory specific to the network parameters and a new estimation model is developed, building on what has been done previously. This model is then applied in the real world using measured data, which is described in Section 4. The results of the application of the new estimation technique are covered in Section 5 and further discussed and analysed in Section 6. Section 7 concludes this study, summarising the methodology and results and then addressing the research questions to finally either accept or reject the defined hypotheses.

2 Previous Work

Although already partially covered in Section 1, this section aims to provide more background on the extensive work done on modelling GICs. Emphasis is placed on literature where the network parameters used in GIC modelling are investigated. Also included is a summary of the more general, but still relevant literature. This section is crucial in answering all the research questions.

Viljanen et al. (1994) [60]

This extensive review paper, which takes into account previous research done [32], summarises the theory of geomagnetically induced currents and serves as the basis for almost all further GIC research. It is this paper that splits GIC modelling into two steps, namely the geophysical and the engineering. In the geophysical step, the horizontal geoelectric field is determined. In the engineering step the geoelectric field derived previously is applied to the network and GICs calculated. When doing this, the geoelectric field over the network acts as an external electromotive force. It should also be noted that the geoelectric field is assumed spatially constant (uniform). This would be the case if the driving ionospheric current is a very wide uniform sheet current or a distant source which results in a plane wave geomagnetic field and if the Earth's conductivity depends only on depth. From this formalism, GICs due to a spatially constant electric field are obtained from equation (28), i.e.,

$$GIC(t) = aE_x(t) + bE_y(t).$$

Here we see the introduction of the constant network parameters a and b. These parameters depend on the resistances and geometry of the power system and are unique to each node in the network. Further relevant comments on the nature of GICs and the network parameters are also made. Since GICs can flow from node to node in a network, the entire network should ideally be taken into account. In practice though, only the local grid is relevant (up to two nodes away). That said, the more complicated the network, generally the less GICs present. When considering GICs in a line, only the apparent geovoltages between nodes affect the resulting GICs. The plane-wave assumption along with a resulting uniform geoelectric field is in this case very convenient indeed since there is no integration along the line needed. This plane-wave assumption is good at mid-latitudes, but not at high latitudes with the auroral electrojets. Luckily, this work deals with modelling at mid-latitudes.

2.1 Applications Internationally

Although this work focusses on modelling GICs in the South African power network, certain international work pertaining to network parameters in GIC modelling can be used as background for local applications.

Pulkkinen et al. (2007) [53]

The authors make the point in this paper that although network parameters can be determined for discretely and continuously grounded systems analytically, often the technical information needed for such computations is not available. In many cases it is also just more practical to fit the parameters to observations - which they do. Two different scenarios are looked at, the first being that the geoelectric field is known and the second being that the geomagnetic field is known. For both cases it is assumed that there are GIC measurements.

In the formalism, the governing GIC equation is updated to include a noise term $\epsilon(t)$ that generalises the uniform plane-wave assumption to non-uniform sources locally if the geoelectric field is known.

It should be noted that this noise term is assumed to be normally distributed with a zero-mean, i.e. bell-shaped. The resistive network assumption from Viljanen et al. [60] above is still assumed, with no inductive effects between the network and geoelectric field. The authors also state that in principle, a and b could be solved from two independent observations at times t_1 and t_2. This is the inspiration for the current work. Instead of this method, the authors used expectation values in order to take the entire time-series into account and solved for a and b. This approach is summarised below.

Given,

$$GIC(t) = aE_x(t) + bE_y(t) + \epsilon(t)$$

and multiplying by E_x and E_y respectively before taking the expectation values of each term, we would get,

$$\Big\langle GIC(t)E_x(t)\Big\rangle = a\Big\langle E_x^2(t)\Big\rangle + b\Big\langle E_y(t)E_x(t)\Big\rangle + \Big\langle \epsilon(t)E_x(t)\Big\rangle$$

and

$$\Big\langle GIC(t)E_y(t)\Big\rangle = a\Big\langle E_x(t)E_y(t)\Big\rangle + b\Big\langle E_y^2(t)\Big\rangle + \Big\langle \epsilon(t)E_y(t)\Big\rangle.$$

Given that the noise term is assumed to have a zero-mean, i.e. $\Big\langle \epsilon(t)\Big\rangle = 0$, and that it is statistically independent from the geoelectric field, we have $\Big\langle \epsilon(t)E_{x,y}(t)\Big\rangle = \Big\langle \epsilon(t)\Big\rangle\Big\langle E_{x,y}(t)\Big\rangle = 0$. Taking this into account and that in general taking the expectation values of the different time-series results in a single value (no more time dependence), a and b can be solved by rearranging the above equations, i.e.

$$a = \frac{\Big\langle GICE_y\Big\rangle\Big\langle E_xE_y\Big\rangle - \Big\langle GICE_x\Big\rangle\Big\langle E_y^2\Big\rangle}{\Big\langle E_xE_y\Big\rangle^2 - \Big\langle E_x^2\Big\rangle\Big\langle E_y^2\Big\rangle}$$

and

$$b = \frac{\Big\langle GICE_x\Big\rangle\Big\langle E_xE_y\Big\rangle - \Big\langle GICE_x\Big\rangle\Big\langle E_x^2\Big\rangle}{\Big\langle E_xE_y\Big\rangle^2 - \Big\langle E_x^2\Big\rangle\Big\langle E_y^2\Big\rangle}.$$

In the second case, where only the GIC and the horizontal ground geomagnetic variations are known only the ratio $c = b/a$ can be determined. A similar approach as the one above is used, but in this case in the frequency domain. After an initial relation in the frequency domain, it assumed that c is independent of frequency, i.e. the network parameters are constant, and a relation in the time domain is derived. The resulting equation for c in the time domain is,

$$c = \frac{\Big\langle B_xB_y\Big\rangle - \chi\Big\langle B_yB_y\Big\rangle}{\Big\langle B_xB_x\Big\rangle - \chi\Big\langle B_xB_y\Big\rangle}$$

where $\chi = \Big\langle GICB_x\Big\rangle/\Big\langle GICB_y\Big\rangle$. Furthermore, the formalism was shown to be able to be extended to dB_x/dt and dB_y/dt. The ratio c (using both approaches) was analysed for different modelled datasets and found to be consistent and robust. When applied to measured datasets it was found that the previously derived analytical network parameters differed to the empirically derived parameters (this can be due to the limits of the analytical model or perhaps the neglecting of the noise term).

Wik et al. (2008) [67]

In this paper, the authors build on the work above. Specifically, they define empirically derived network parameters, α and β. To obtain these parameters, they assume a uniform geoelectric field close to the GIC site and make use of a least squares fitting routine to solve the equation,

$$GIC(t) = \alpha E_x(t) + \beta E_y(t).$$

The authors note that the ratio of network parameters changes, depending on the selected GIC threshold (used to define data used) and the location of where the geoelectric field is calculated. It is also noted that the ratio seems to decrease with an increase in GIC threshold. Not noted, but also relevant to this current work is that for higher GIC thresholds, the network parameters themselves seem to increase. Again, the point is made that for an empirical method, the estimation is only valid for the node at which it is calculated and given that the network configuration does not change.

In this paper, there is also a direct comparison between analytically derived network parameters (a and b in the usual sense) and the empirically derived network parameters. The ratio of the b/a was found to be -2 which falls within the range of values determined for β/α. This range was between -1.5 and -4.9. In an ideal case, these should be equal. This is not the case, but it is noted that the empirically derived parameters take into account the network as well as the conductivity profile used for the geoelectric field whereas the analytically derived parameters only take into account the network.

2.2 GIC and Network Parameter Modelling in South Africa

Closer to home there has also been a lot of research into modelling GICs and network parameter dependence. These contributions would be a useful yardstick to measure performance of the current work, since the current work deals with the South African grid and makes use of local data.

Koen (2002) [30]

In his PhD thesis, Koen does a rigorous assessment of GIC occurrence and risk in the South African grid. With regards to network parameters he makes use of the grid information available to derive analytical network parameters. Specific to this work, the derived (a, b) network parameters for the Hydra and Grassridge substations are (25,-111) and (-80,15) respectively. Also noted in the modelling is that when the ratio of the network constants differs by a magnitude four or more, the direction is biased to the direction is dominated by the bigger constant and the term relating to the smaller constant can be ignored for calculation purposes. The geoelectric field is calculated using a homogeneous Earth with constant ground conductivity. From this, a look-back time is defined and used to estimate the geoelectric field from the geomagnetic field. This procedure is described in full by Viljanen et al. [62].

Bernhardi et al. (2008) [4]

In this paper, GIC modelling in South Africa is improved using a SECS (Spherical Elementary Current Systems) interpolation scheme and applying the network parameters as defined by Koen [30]. The SECS interpolation scheme interpolates the geomagnetic field, resulting in a better local estimate of the geomagnetic field. The method used to derive the geoelectric field is the same as in Koen [30].

Ngwira et al. (2008) [43]

Firstly, this paper makes use of the method used by Pulkkinen et al. [53] to update the network parameters for Grassridge. After calculating the network parameter ratio, a was fixed from previous work done by Koen [30] and b updated to agree with the ratio. The resulting parameters for Grassridge are now $a = -80$ A km/V and $b = 1$ A km/V.

Up until this paper, GIC modelling made use of a uniform one-layer ground conductivity structure. The authors have improved on this by deriving a layered conductivity model that includes a wider frequency band than that normally associated with GICs. An apparent surface impedance was derived from geomagnetic field, GIC data and the new network coefficients. From this the surface impedance could be inverted using the simplified Occam's inversion algorithm and apparent resistivities and phases could be computed. The resulting 1-D 10-layer ground conductivity model is not a characterisation of the geology between the magnetometer and GIC site, but rather a reflection.

Ngwira et al. (2009) [42]

This paper follows up on Bernhardi et al. [4] and makes use of both SECS and fixed magnetometers to ascertain how 'local' a magnetometer needs to be to give an accurate representation of the geomagnetic (and hence geoelectric) field at a GIC site. The case study concludes that at low- to mid-latitude regions, the geoelectric field can be modelled relatively accurately within a spatial scale of about 600 km in the east-west direction and 300 km in the north-south direction (performance falls off more quickly). Specifically, it was found that Grassridge can be modelled well with Hermanus magnetometer data and a layered Earth conductivity model.

Matandirotya et al. (2015) [36]

Previous GIC modelling in South Africa have used a uniform Earth model which was then improved on using a layered Earth conductivity profile to derive the geoelectric field. This paper goes a step further and makes use of the relatively new application of finite element modelling (FEM) to compute the geoelectric field [19]. Along with the new technique, an interpolated geomagnetic field is used which further improves the modelling. More pertinent to the current work is a new empirical method for estimating the network parameters. The newly derived network parameters improve modelling in general but not during storm time.

The new empirical method entails identifying zero crossings for the different geoelectric field components. At a particular zero crossing, the governing GIC equation simplifies to a simple relation between the measured GIC and the measured non-zero geoelectric field component. To calculate the coefficient of the non-zero geoelectric field component, the ratio between the measured GIC and the measured non-zero geoelectric field component is taken. At this point it should be noted that the data used for calculation was specifically selected to ensure noise effects and divergence were avoided. This means only time instances where $|GIC| > 0.1 \times RMS(GIC)$ were used (RMS refers to the Root Mean Square). The geoelectric field data was further masked according to which parameter was to be calculated (relevant directional weighting). Geoelectric field angles in the general the north-south direction relate to the a network parameter. Those in the east-west direction relate more so to the b network parameter. In terms of data selection criteria, this means for a parameter calculation only geoelectric field values satisfying $|E_x| > 0.7 \times RMS(E_x)$ and $|E_y| < 0.1 \times RMS(E_y)$ were used. For b parameter calculation, only geoelectric field values satisfying $|E_y| > 0.7 \times RMS(E_y)$ and $|E_x| < 0.1 \times RMS(E_x)$ were used. This resulted in 31 a estimates and 11 b estimates for the Halloween Storm of 2003. The estimates were then arranged in the order of decreasing GIC magnitude. The polarity of the estimated a network parameter was consistently positive, whereas b was not.

For simplicity, the a network parameter estimates were further analysed. Outlier values that significantly increased the standard deviation of the a estimate set were discarded. From the remaining estimates, the estimates corresponding to the 10 largest GIC magnitudes were averaged. This produced a single estimate for a. Once again, the network parameter ratio derived by Ngwira et al. [43] was used to obtain an estimate for b. The final result was $a = -94$ A km/V and $b = 24$ A km/V.

2.3 Summary of Relevant Literature

Besides the literature cited in Section 1 and the main cases outlined above, there is a large body of other work relevant to this project. This is summarised, along with the literature already cited, in Table 1.

Title	Author(s)	Year	Local (Y/N)	Network Parameters (Y/N)	Relevant Aspects	
Basic Theory of the Magneto-Telluric Method of Geophysical Prospecting	Cagniard, L.	1953	N	N	Details the ground assumptions for the MT method to derive the geoelectric field	[12]
On the Relation Between Telluric Currents and the Earth's Magnetic Field	Wait, J. R.	1954	N	N	Layered ground conductivity profile introduced to MT method	[64]
The theory of magnetotelluric methods when the source field is considered	Price, A. T.	1962	N	N	MT method is considered while taking into account an ionospheric current source	[50]
Electromagnetic induction in the Earth by a plane-wave or by fields of line currents harmonic in time and space	Pirjola, R.	1982	N	N	Theoretical models of the link between the ionospheric current system and geoelectric field are formulated, specifically the plane-wave assumption	[48]
Currents produced in earthed conductor networks by geomagnetically-induced electric fields	Lehtinen, M. and Pirjola, R.	1985	N	Y	Pioneering paper regarding the calculation of GICs in an arbitrary grounded network - nodal matrix and system parameter approaches are introduced	[32]
Use of GIC's in Studies of Ionospheric-Magnetospheric Currents and the Earth's Structure	Viljanen, A. & Pirjola, R.	1991	N	Y	Theoretical calculation of GICs with result that GIC flow is limited to several hundred kilometres	[59]
What is a geomagnetic storm?	Gonzalez et al.	1994	N	N	Defines *Dst* thresholds for geomagnetic storms	[23]
Geomagnetically induced currents in the Finnish high-voltage power system	Viljanen, A. & Pirjola, R.	1994	N	Y	Ground assumptions for governing GIC equation stated and network parameters described	[60]
The complex-image method for calculating the magnetic and electric fields produced at the surface of the Earth by the auroral electrojet	Boteler, D. H. & Pirjola, R.	1998	N	N	Calculation of the geoelectric and geomagnetic field at the surface as a result of the auroral electrojet and taking into account different conductivity profiles	[10]
The effects of geomagnetic disturbances on electrical systems at the Earth's surface	Boteler, D. H., Pirjola, R. & Nevanlinna, H.	1998	N	N	Summary of incidents of geomagnetic effects on power networks and correlation to geomagnetic variation and solar cycle	[8]
On calculating the electric and magnetic fields produced in technological systems at the Earth's surface by a "wide" electrojet	Boteler, D. H., Pirjola, R. & Trichtchenko, L.	2000	N	N	Calculation of the geoelectric and geomagnetic field at the surface for a Cauchy distributed current density that relates to a "wide" current instead of a line current	[9]

GIC observations and studies in the Hydro-Québec power system	Bolduc, L.	2002	N	N	Analysis of the 1989 Hydro-Québec black-out resulting from a severe geomagnetic storm	[5]
Disturbances in the Southern African Power Network Due To Geomagnetically Induced Currents	Koen, J. & Gaunt, C. T.	2002	Y	N	Demonstrates (and analyses) for the first time that GICs have adversely effected the South African power network, thought previously not to be at risk	[31]
Geomagnetically Induced Currents in the Southern African Electricity Transmission Network	Koen, J.	2002	Y	Y	Further analysis of GIC effects in South African power network and derivation of theoretical network parameters	[30]
Storm sudden commencement events and the associated geomagnetically induced current risks to ground-based systems at low-latitude and midlatitude locations	Kappenman, J. G.	2003	N	N	Links SSC events to large GICs at mid-latitude regions	[24]
Geomagnetic Induction During Highly Disturbed Space Weather Conditions : Studies of Ground Effects	Pulkkinen, A.	2003	N	Y	Rigorous theoretical framework of GIC drivers and modelling during disturbed time (also includes SECS interpolation scheme)	[52]
An overview of the impulsive geomagnetic field disturbances and power grid impacts associated with the violent Sun-Earth connection events of 29-31 October 2003 and a comparative evaluation with other contemporary storms	Kappenman, J. G.	2005	N	N	The 1989 Hydro-Québec and 2003 Halloween geomagnetic storms are compared with emphasis on morphology and GIC impact with the result that ring current intensifications seem to drive GICs at low and equatorial latitudes	[25]
Estimation of geomagnetically induced current levels from different input data	Pulkkinen, A., Viljanen, A. & Pirjola, R.	2006	N	Y	Statistical methods are used to model GICs and specifically it is shown that the network parameters can be derived empirically given geoelectric field and GIC data	[51]
High-resolution global storm index: Dst versus SYM-H	Wanliss, J. A. & Showalter, K. M.	2006	N	N	Relation between *Dst* and SYM-H defined for geomagnetic storms	[66]
Transformer failures in regions incorrectly considered to have low GIC-risk	Gaunt, C. T. & Coetzee, G.	2007	Y	N	Transformers in the South African power network are shown by DGA to fail as a result of geomagnetic storm related GICs	[21]
Determination of ground conductivity and system parameters for optimal modelling of geomagnetically induced current flow in technological systems	Pulkkinen, A., Pirjola, R. & Viljanen, A.	2007	N	Y	Empirical network parameters are derived for optimal modelling along with a suitable ground conductivity model from an empirical surface impedance derived using a least squares fit to measured data - a distance of 200-300 km between magnetometer and GIC measurement was found to be acceptable	[53]
Geomagnetically induced currents in an electric power transmission system at low latitudes in Brazil: A case study	Trivedi et al.	2007	N	N	A case study of GIC occurrence in Brazil	[58]
Improvement in the modelling of geomagnetically induced currents in Southern Africa	Bernhardi, E. H., Cilliers, P. J. & Gaunt, C. T.	2008	Y	Y	SECS interpolation is used to improve on previous homogeneous Earth GIC modelling in South Africa (uses analytically network parameters at Grassridge)	[4]

Improved modelling of geomagnetically induced currents in the South African power network	Ngwira et al.	2008	Y	Y	Defines empirical ratio of network parameters and updates previous analytical network parameter pair at Grassridge - an empirical layered ground conductivity is further defined	[43]
Calculation of geomagnetically induced currents in the 400 kV power grid in southern Sweden	Wik et al.	2008	N	Y	Empirical network parameters derived from a least squares fit	[67]
Limitations of the modelling of geomagnetically induced currents in the South African power network	Ngwira et al.	2009	Y	Y	Looks at reliability of GIC modelling with distance between magnetometer and GIC sites given specific empirical layered Earth conductivity model	[42]
Derivation of characteristics of the relation between geomagnetic and geoelectric variation fields from the surface impedance for a two-layer earth	Pirjola, R.	2010	N	N	A study of the properties of the surface impedance and ground conductivity layers that lead to conclusions about the geoelectric and geomagnetic field relations	[49]
Deep Crustal Structure of the Son-Narmada-Tapti Lineament, Central India	Naidu, G. D.	2012	N	N	Summary of MT method and assumptions made	[41]
On the probability of occurrence of extreme space weather events	Riley, P.	2012	N	N	A statistical study of the probability of extreme events, such as the Carrington event, with possible application to probabilistic forecasting	[54]
Modelling geomagnetically induced electric field and currents by combining a global MHD model with a local one-dimensional method	Zhang, J. J., Wang, C. & Tang, B. B.	2012	N	Y	GIC prediction using a global MHD model to predict the geomagnetic field and then using the usual methods (with empirical network parameters) to predict GICs	[72]
Evaluating the applicability of the finite element method for modelling of geoelectric fields	Dong et al.	2013	N	N	FEM used to simulate geomagnetic and geoelectric fields, specifically with a layered Earth conductivity model that includes an interface between two profiles	[19]
Geomagnetically induced currents in Europe: Characteristics based on a local power grid model	Viljanen et al.	2013	N	N	A local grid model is used to characterise GICs in Europe with results that the intensity of geomagnetic variation and conductivity profiles are the main drivers (there was no dependence on the grid - although certain grid characteristics are defined as relevant, i.e. line resistances, line length, number of nodes to take into account and conductivity profile under the network)	[61]
Solar Storm Risk to the North American Electric Grid - Lloyd's	Maynard, T., Smith, N. & Gonzalez, S.	2013	N	N	A report on the risk associated with an extreme geomagnetic storm and its impact on the North America power network and economy	[37]
Geoelectric fields due to small-scale and large-scale source currents	Zheng et al.	2013	N	N	Line current and plane-wave sources are considered and shown to be different except when the distance to source or the frequency considered is large	[73]
Effects of geophysical parameters on GIC illustrated by benchmark network modelling	Zheng et al.	2013	N	N	A benchmark grid model is used to quantify the significance of geomagnetic variation and Earth's conductivity in GIC modelling	[74]

Methodology for simulation of geomagnetically induced currents in power systems	Boteler, D.	2014	N	N	Outlines the methods for simulating GIC in an arbitrary power network as part of power system analysis	[6]
On extreme geomagnetic storms	Cid et al.	2014	N	N	Outlines characteristics of extreme geomagnetic storms	[15]
Reducing uncertainty – responses for electricity utilities to severe solar storms	Gaunt, C. T.	2014	Y	N	Defines what is needed in terms of a mitigation scheme for power utilities	[20]
A solar wind-based model of geomagnetic field fluctuations at a mid-latitude station	Lotz, S. I. & Cilliers, P. J.	2015	Y	N	Model to use solar wind data to model geomagnetic field variation	[33]
Modelling geomagnetically induced currents in the South African power transmission network using the finite element method	Matandirotya, E., Cilliers, P. J. & Van Zyl, R.	2015	Y	Y	Empirically derived network parameters are used along with network parameter ratio to create new network parameter estimates for Grassridge and used with a FEM derived geoelectric field for improved GIC modelling	[36]
Geomagnetically Induced Currents (GIC) in Large Power Systems Including Transformer Time Response	Oyedokun, D.	2015	Y	N	An overview of GIC modelling for a power system analysis viewpoint with emphasis on transformer time response	[47]
GIC due to storm sudden commencement in low-latitude high-voltage power network in China: Observation and simulation	Zhang et al.	2015	N	Y	Empirically derived network parameters are used and SSC events are found to be correlated to large GICs at low-latitudes, especially in the eastward direction	[71]
Geoelectric hazard maps for the continental United States	Love et al.	2016	N	N	Hazard map of extreme geoelectric field cases over North America	[35]
Searching for Carrington-like events and their signatures and triggers	Saiz at al.	2016	N	N	Characterisation of Carrington-like events and details possible drivers such as field-aligned Currents (instead of ring current) and abrupt Southward reversals of the IMF	[55]
Modelling geomagnetically induced currents	Boteler, D. H. & Pirjola, R.	2017	N	N	Extensive overview of GIC modelling from the fundamental drivers to geoelectric field derivation and power system analysis	[11]
Quantifying the daily economic impact of extreme space weather due to failure in electricity transmission infrastructure	Oughton et al.	2017	N	N	The potential economic cost of a power system failure in the United States as a result of an extreme geomagnetic storm is quantified	[46]
Regression-based forecast model of induced geoelectric field	Lotz, S. I., Heyns, M. J. & Cilliers, P. J.	2017	Y	Y	GIC forecasting is implemented using solar wind data and empirically derived network parameters	[34]
Influences of various magnetospheric and ionospheric current systems on geomagnetically induced currents around the world	de Villiers et al.	2017	Y	N	Identifies relevant current systems for GICs at low and mid latitudes	[18]

Table 1: Summary of literature relevant to this work.

3 Theory and Model Development

When dealing with a system as complicated and/or non-linear as the effect of space weather on the power network, it becomes increasingly difficult to make use of analytical models. Analytical models simply cannot cope with all the variables involved - the simple case of the coastal effect or even an anomalous conductivity structure in the Earth can throw the results. Also typical with analytical models is the difficulty dealing with uncertainty in the results. Certain measured quantities have intrinsic errors associated with them, but how these propagate in a model where other parameters, such as network parameters, are assumed is not well defined. Even if there were models that could cope with all the variables involved and describe the different couplings perfectly (which as is seen in Section 1, we don't even fully understand), they are only as good as the data put into them. The South African power grid, where there is a lack of quality data made available about the state of the network at any given time, is a perfect example. This has affected previous analytical modelling of the network, which has been the main source of network parameters for GIC modelling in South Africa. Empirical models on the other hand can absorb the complicated and non-linear effects. These methods allow the use of a simple, physically relevant model as a basis to relate different sets of data. The parameters in such a simple model are then trained according to the data and the result is the best possible description of the relationship according to the simple model. These parameters may not be as well defined as those in analytical models, where they attempt to describe a certain physically defined factor. Instead, they may absorb the non-linearities and complexities that arise from special cases, such as a non-uniform geoelectric field. In this work, the simple model of the system used for empirical analysis is that defined by equation (28). This simple model also assumes a uniform geoelectric field across the relevant parts of the network.

3.1 Underlying Theory of Network Parameters

It pays to look further into the system geometry and specifically the direction of the induced uniform geoelectric field with respect to local network orientation (dot product related projection as defined by the EMF). This has specific implications pertaining to research questions RQ3 and RQ4. As mentioned in Section 1.3, this uniform geoelectric field assumption is a simplification and valid locally (which is defined according to the driving system). Much more realistic is a non-uniform geoelectric field, but this itself could be broken up into discreet sections where some sort of uniform geoelectric field is valid locally. These sections then together would contribute to the final result (the geoelectric field has to be integrated along the path of the transmission line). Since we can choose appropriate scales that result in a locally valid uniform field, in this section we only consider such cases. As mentioned before, the scales that define a local uniform geoelectric field at mid-latitudes are comparable with the entire system considered and a uniform field treatment (with no integration along the transmission lines) suffices as a good first order approximation.

Firstly, the network parameters are only defined as such in Cartesian coordinates. In cylindrical coordinates, there would also be two parameters but with different physical interpretations. The first would be a radial magnitude scaling factor, that takes into account the systems resistance and so forth, as if we were dealing with an aligned system (defined as ζ in Section 1.3). The second would be an angular alignment factor that takes into account the geometry of the network and the alignment of the geoelectric field with this geometry. The Cartesian version of this is purely a projection of the scaling and alignment components onto the Cartesian base of the northerly x and the easterly y directions. Thus, the network parameters can also be thought of as scaling factors that penalise non-alignment of the geoelectric field vector with the network. From these parameters, the preferred direction (angular alignment factor) for the geoelectric field to produce large GICs can be found.

To illustrate the preferred directionality defined by the network parameters, it helps to first visualise

the system in cylindrical coordinates. In this coordinate system, let us assume there a uniform unitary induced geoelectric field of $\vec{E} = 1$ in an arbitrary direction defined by an angle θ (represented by the blue vector in Figure 21). Fixing the magnitude in this case allows us to emphasise the directionality dependence. In addition to this, let us assume there is a length of transmission line connected to a network node (say a substation with a grounded neutral line) that stretches straight in a direction defined by ϕ (represented by the thick black line in Figure 21). For simplicity, let us also assume that there is a direct relation between the geoelectric field and the measured GIC in a transmission line with no network scaling whatsoever. Given this simplification, we would have the relation,

$$GIC = |\vec{E}| \cos(\phi - \theta) = \cos(\phi - \theta). \tag{33}$$

This is purely a scalar projection of the geoelectric field onto the transmission line (represented by the green vector in Figure 21). From equation (33), we see that the magnitude of the measured GIC is maximised when $\phi = \theta$, i.e. the geoelectric field is aligned to the network. Still using the simplification of a one-to-one relationship along with the concept of a projection between the geoelectric field and the line (measured GIC) and further defining the unit vector of the transmission line as $\hat{\varphi}$, we would expect,

$$\overrightarrow{GIC} = \frac{\hat{\varphi} \cdot \vec{E}}{|\hat{\varphi}|}\hat{\varphi} = \hat{\varphi_x} E_x \hat{x} + \hat{\varphi_y} E_y \hat{y}. \tag{34}$$

Here, the measured GIC is represented by a vector in the direction of the flow in transmission line, i.e. $\hat{\varphi}$. The traditionally defined GIC can then be linked to equation (34) by,

$$\overrightarrow{GIC} = aE_x\hat{x} + bE_y\hat{y} = \hat{\varphi_x} E_x \hat{x} + \hat{\varphi_y} E_y \hat{y}. \tag{35}$$

From this we can see the link between the direction of the transmission line and the network parameters, i.e. $a = \hat{\varphi_x}$ and $b = \hat{\varphi_y}$. Going back to cylindrical coordinates, the direction as defined by angle is,

$$\phi = \arctan\left(\frac{\hat{\varphi_x}}{\hat{\varphi_y}}\right) = \arctan\left(\frac{a}{b}\right). \tag{36}$$

The preferred direction of the geoelectric field to produce large GICs would ultimately maximise equation (33). This results with the condition that $\phi = \theta$ and hence,

$$\theta = \arctan\left(\frac{a}{b}\right). \tag{37}$$

Of course in the real world, the geoelectric field magnitude is not unitary or fixed and the relationship between the geoelectric field and the measured GIC is not one-to-one. Factors such as the resistance of the transmission lines need to be taken into account (see Section 1.3). This is in effect just a scaling factor in terms of the magnitude (represented by the red vector in Figure 21) of the resultant GIC and does not affect the directionality dependence. This can be illustrated in the same way as above, but also including the indirect relation of Ohm's Law with some network defined scaling parameter ζ and using an arbitrary geoelectric field (see Section 1.3 and specifically equation (30)). In this case,

$$GIC = \zeta |\vec{E}| \cos(\phi - \theta). \tag{38}$$

The resulting GIC is also no longer just a projection, but includes some sort of scaling,

$$\overrightarrow{GIC} = \zeta \frac{\hat{\varphi} \cdot \vec{E}}{|\hat{\varphi}|} \hat{\varphi} = \zeta \hat{\varphi}_x E_x \hat{x} + \zeta \hat{\varphi}_y E_y \hat{y}. \tag{39}$$

This scaling vanishes when direction is considered, since the ratio of Cartesian components is taken, and the resistance of transmission lines is assumed to be independent of direction (only dependent on length),

$$\theta = \phi = \arctan\left(\frac{\zeta \hat{\varphi}_x}{\zeta \hat{\varphi}_y}\right) = \arctan\left(\frac{a'}{b'}\right) = \arctan\left(\frac{\hat{\varphi}_x}{\hat{\varphi}_y}\right) = \arctan\left(\frac{a}{b}\right). \tag{40}$$

Of course in actual GIC modelling the magnitude scaling is very relevant and we have that the conductivity and other factors (given a real world system) are absorbed into the network parameters, i.e. $a' = \zeta \hat{\varphi}_x \neq a$ and $b' = \zeta \hat{\varphi}_y \neq b$ as defined here. Another consideration is the fact that in a real world system there is often a number of transmission lines connected to a node. In this case, the measured GIC at the node would be a combination of the different line GICs. To get the directionality dependence in such a case, each specific line needs to be taken into account and the result weighted according to line length, conductivity and other factors influencing the resulting GIC magnitude. It could often be the case that multiple directions are relevant, with a network parameter defined directionality distribution being the nett result. It should also be noted that for significant GICs to be produced at a node, the line must terminate at the node and be grounded. If a transmission line flows through a node, then most of the GIC would continue through as well, with only a faction being measured at the node.

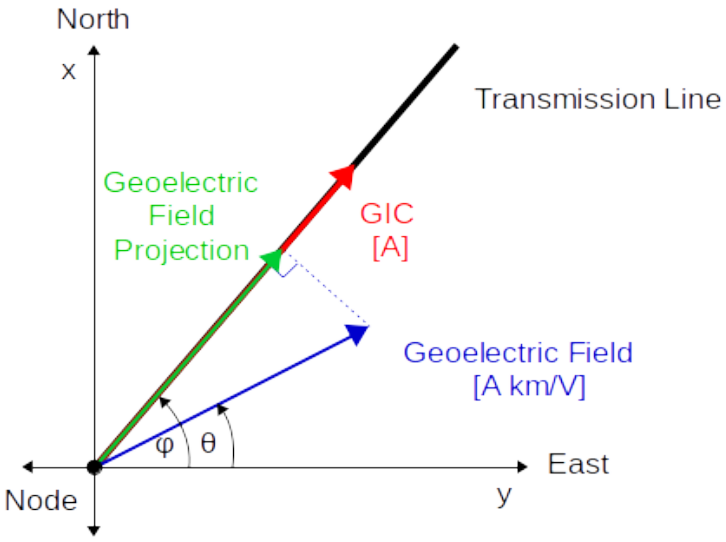

Figure 21: A visualisation of the link between the geoelectric field, the measured GIC and the network.

Any deviation of the geoelectric field from the preferred angle θ would result in a fraction of the total geoelectric field magnitude contributing to the measured GIC. The ratio of network parameters used in previous work [43] is encoded in this angle. That specific ratio was defined as b/a, which in effect is the angle from north, whereas a/b as used above is the angle from east. Since the GIC can only flow in the transmission lines, we have a constraint on the direction the resulting GIC can be. Given this, we expect the preferred direction of the geoelectric field to reflect the direction of the transmission lines immediately around the substation, i.e. $\theta = \phi$. This concept is looked at further in Section 6.3.

As mentioned, estimation of the network parameters can be done analytically, using a model of the power system, or empirically, using only data. From simultaneous GIC and $E_{x,y}$ data, an estimate of the network parameters can be derived [51, 67, 36]. It is assumed that these parameters are constant over the time scale of a geomagnetic event, only changing with major alterations of power network related hardware or operations [61]. That said, there are associated errors at each point in the GIC modelling chain. This is also true for the 'engineering step' in the modelling. In contrast to the assumption of unchanging parameters, it has been observed that different empirical values of a and b may be derived for a variety of different conditions including the specific GIC magnitude threshold used [67, 36] and conductivity/network modelling [36]. This suggests that a number of errors from different drivers are absorbed into these parameters. As a result, the variation in the network parameters should be taken into account when modelling GICs. In this work, we will borrow notation from Wik et al. [67], where α and β represent the empirically derived network parameters. Furthermore, we will define the ensemble of empirically derived parameters to be $\boldsymbol{\alpha}$ and $\boldsymbol{\beta}$ respectively (see Section 3.2). These ensembles include a huge number of parameter pairs that have been calculated from pairs of triplets as defined by equation (28). Each estimate in the ensemble is not defined as the true state of the system, but simply a possible state as calculated by solving simultaneous equations. Taking all the ensemble estimates into account together would reveal the most probable state.

This investigation of network parameters shows the extent of variation observed in derived network parameters over the course of a number of events as well as during an event (expanded further in Section 5). Histograms of the collection of $\boldsymbol{\alpha}$ and $\boldsymbol{\beta}$ values are plotted and the probability density function (PDF) of each parameter is estimated. Using a range of α and β values instead of single values enables an estimation of the measured GIC as a range of possible values changing in time (expanded further in Section 6.2). Furthermore, potential drivers of the variation in network parameters are identified and quantified (expanded further in Section 6.1). The data used in this analysis is described in Section 4.1.

3.2 Statistical Sampling

In both previous analytical and empirical work, network parameters have been assumed to be (i) constant and (ii) to be single valued. However, in previous empirical methods, there were indications that different parameter values were valid for different datasets used at the same power network node and magnetometer pair. These different datasets were defined by different GIC magnitudes [67, 36]. Although not acknowledged, a range of network parameters is to be expected in an empirical model. The simple governing model used would take into account non-linearities and complexity not included in the model by absorbing these perturbations into the parameters. Generally some sort of averaging is used to condense this effect into a single value. Although convenient for modelling, information is lost in the process. Instead we can use a similar approach of ensembles as used in statistical mechanics. In what is often considered the founding work of modern statistical mechanics, it was shown how the laws of thermodynamics arise from simple systems based on classical mechanics when some of the natural uncertainty about the state of the system is included [22]. Furthermore, it was shown how statistical mechanics can extend classical thermodynamics. At that time (1902), quantum physics was not even known of. By assuming as little as possible about the system (i.e. as simple a governing equation as possible) the results of this initial work on statistical mechanics has largely been shown to be accurate, even with the development of quantum mechanics. From this, an ensemble is defined as an idealisation that considers a huge number (could be infinitely many) of copies of a system. Each single copy represents a possible state of the real system. The variation in network parameters seen in previous empirical network parameter modelling is in effect a biasing of the empirical method to a subset of all the possible states. When all states are considered together and the result normalised appropriately, an ensemble becomes a probability distribution of system states.

In our case, the system would be defined by the governing GIC equation (see equation (28)). Physically, this includes the power network with its GIC measurement and the magnetometer with its geomagnetic field measurements. Of course the magnetometer's geomagnetic field measurements are indirectly part of the system, since they are used to derive the geoelectric field using an assumed ground conductivity profile. This step already introduces significant uncertainty into the system, along with the uncertainty involved in the measurements themselves. Given the system as defined by the governing equation, we can also define a subset of the system, namely the network parameters. Taking a time-series that includes both the GIC and geoelectric field for the given time instances, we can consider each an independent state of the system. Let us assume there are n time instances, each defined as a measured state of the system,

$$GIC(t_i) = a_i E_x(t_i) + b_i E_y(t_i), i \in \{1, ..., n\} \tag{41}$$

Taking any two of these states and using them to solve for the network parameters would result in an independent state of the network parameter subsystem.

$$\begin{array}{c} \\ (\alpha_k, \beta_k) = (\alpha_{i,j}, \beta_{i,j}) \\ k \in \{1, ..., l\} \\ \\ \end{array} \qquad \begin{array}{lrcl} t_1: & \Gamma(t_1) & = & \alpha_1 E_x(t_1) + \beta_1 E_y(t_1) \\ & & \cdots & \\ t_i: & \Gamma(t_i) & = & \alpha_i E_x(t_i) + \beta_i E_y(t_i) \\ & & \cdots & \\ t_j: & \Gamma(t_j) & = & \alpha_j E_x(t_j) + \beta_j E_y(t_j) \\ & & \cdots & \\ t_n: & \Gamma(t_n) & = & \alpha_n E_x(t_n) + \beta_n E_y(t_n) \end{array}$$

In this cases we assume that given two time instances, the network parameters are constant, i.e. $\alpha_i = \alpha_j$ and $\beta_i = \beta_j$. Solving these will result in $\alpha_{i,j}$ and $\beta_{i,j}$, which are defined by the two time instances and assumed constant for both. Of course, using all possible combinations of time instances will result in a number of different 'constant' network parameter estimates for a given instance. Although this seems to be a paradox, we should remember that each calculated network parameter pair is a possible state of the network parameters as defined by the time instances used to calculate them, and not the true state. Each set of calculated network parameter estimates can thus be collected into an ensemble. Given n relevant and comparable time instances, there will be a total of $l = n(n-1)/2 \approx n^2/2$ (for large n) sets of network parameter pairs. The network parameter subsystem will in fact result two separate ensembles, one for each network parameter. Considering each ensemble separately results in a probability distribution of that specific network parameter. From this distribution, the most probable state and hence the most probable value of the network parameter can be found. This is the typical single-valued approach. Additionally, considering the whole ensemble though allows for further analysis, since the nature of the probability distribution can provide insights into the nature of the system as it stands. An example of this would be using different input data and analysing the change in the probability distribution. Since the ensemble includes a huge number of estimates, including those generated by special cases where the system is in fact non-linear, a range of values can be used to define the network parameters. Even if not using a range of parameter values in modelling, the typical spread quantifies uncertainty in GIC modelling as a result of error propagated throughout the modelling chain.

3.3 Model Development - Ensemble Estimation

In order to create an ensemble of the network parameters, the linear nature of equation (28) is exploited. This governing equation assumes that the GIC measurements and the derived $E_{x,y}$ values are perfect. A further assumption is that network doesn't change appreciably over the time-series

considered. This however is not entirely accurate, since errors in GIC and the derived geoelectric field are present. Assuming a and b are constant, a more accurate relationship would be,

$$GIC(t) + GIC(t)_{err} = a\Big(E_x(t) + E_x(t)_{err}\Big) + b\Big(E_y(t) + E_y(t)_{err}\Big), \tag{42}$$

where X_{err} indicates the error made in the measurement or estimation of a relevant parameter X. This form of equation (28) shows explicitly that, due to the errors in $E_{x,y}$ and GIC, a and b are not independent of induced geoelectric field, and therefore not independent of GIC magnitude. Nevertheless, assuming a linear relationship between GIC and the geoelectric field of the form of equation (28) allows estimation of network parameters. In order to acknowledge the presence of inaccuracy in measurements though, the notation of the governing equation is changed to,

$$\Gamma(t) \approx \alpha E_x(t) + \beta E_y(t), \text{ where} \tag{43}$$

$$\Gamma(t) \equiv GIC(t) + GIC(t)_{err} \text{ (or the GIC as measured)}, \tag{43a}$$

$$\alpha \equiv a\Big(1 + E_x(t)_{err}/E_x(t)\Big) \text{ and} \tag{43b}$$

$$\beta \equiv b\Big(1 + E_y(t)_{err}/E_y(t)\Big). \tag{43c}$$

In matrix notation, equation (43) would simply be,

$$\Gamma(t) = \begin{bmatrix}\alpha & \beta\end{bmatrix} \begin{bmatrix} E_x(t) \\ E_y(t) \end{bmatrix}. \tag{44}$$

In the updated governing GIC equation, the α and β network parameter estimates take the place of the traditional network parameters, being empirically derived from measured data. These estimates include the associated error from the geoelectric field as well as the traditional definition of the network parameters. In this work, we additionally define $\boldsymbol{\alpha}$ and $\boldsymbol{\beta}$ to be the collection of α and β estimates obtained (referred to as the network parameter ensembles or distributions of network parameters). Assuming a time-series with a number of $E_{x,y}$ instances and constant network parameters a and b, then the resulting empirical $\boldsymbol{\alpha}$ and $\boldsymbol{\beta}$ ensembles would be bell-shaped. This stems from the form of the equations defining α and β where the estimates are related to the traditional constant network parameters a and b along with the deviation defined by an error term. Given enough estimates, the peak of the ensemble or distribution should reflect the traditional network parameters, with the spread coming from the error term's deviation. Generally, measurement errors follow normal distributions, but in this case the error term is defined by the error in the geoelectric field divided by the geoelectric field itself. Given that there would often be small geoelectric fields in the time-series considered, this will blow up. The resulting spread would most likely still be bell-shaped but with heavier tails than a typical normal distribution. At this point it should also be noted that although typical measurement errors are assumed to be normally distributed, the derived geoelectric field is not measured and propagates errors in the measured geomagnetic field and the assumed impedance profile. Errors in these components can possibly lead to initially heavier tails, such as homogeneous broadening for given geomagnetic frequencies when there is wrong impedance scaling (from the assumed profile). This relates to many time instances where the geoelectric field is inaccurate, which is compounded in the solving of network parameters, ultimately providing a base for the heavy tails. It should be noted that the error in GIC measurement is also present, and that the empirically modelled GIC would in fact include this error.

Taking this updated version of the GIC equation, let us think of the network parameters as variables and the E_x and E_y components to be coefficients of these variables. This is exactly the opposite of the common interpretation. The assumption that the network parameters are constant over a certain time period $\{t_1, \ldots t_n\}$ allows us to solve for α and β simultaneously given two time instances (say

t_i and t_j). Using any more than two comparable time instances would result in an overdetermined system.

Given two selected time instances, the system of linear equations would be represented in matrix form in the typical form of $\mathbf{Ax} = \mathbf{b}$, where $\mathbf{A}$ is a $m \times n$ (rows $\times$ columns) coefficient matrix, $\mathbf{x}$ the variable column vector with n components and $\mathbf{b}$ the resultant column vector with m components. With two time instances used to solve the two variables α and β, the system would be defined by a 2×2 matrix with the geoelectric field as components. The resultant column vector is of course the measured GIC. Summarised, the system would be in the form,

$$\begin{bmatrix} E_x(t_i) & E_y(t_i) \\ E_x(t_j) & E_y(t_j) \end{bmatrix} \begin{bmatrix} \alpha \\ \beta \end{bmatrix} = \begin{bmatrix} \Gamma(t_i) \\ \Gamma(t_j) \end{bmatrix}. \tag{45}$$

Given this matrix equation representing the system of linear equations, the variables α and β can easily be solved for using Cramer's Law, Gaussian elimination (or variants thereof) or simply taking the inverse of $\mathbf{A}$ and solving the matrix equation directly.

Repeated calculation of α and β for a number of (i, j) pairs creates an ensemble of network parameters $\boldsymbol{\alpha}$ and $\boldsymbol{\beta}$. Normalising these ensembles creates a PDF. As mentioned in Section 1, the result would no longer be a single estimate of the parameters, but a collection of different parameter pairs that satisfy the system for different pairs of time instances. Each estimate of the network parameters includes the associated error from the geoelectric field derivation. This error would typically be a cause of spread in the resulting ensemble. That said, the most probable estimate in the ensemble would relate to the traditional definition of a network parameter.

Previous empirical estimation has generally included a fit of sorts that results in a single estimate. One approach is to use a least squares routine and fit equation (28) to the data [67]. An alternate approach is to select near-zero crossings of the geoelectric field for a single geoelectric field component and solve equation (28). This would generate a number of single parameter estimates at these specific time instances. A linear fit is then used to find the best parameter while excluding outliers [36]. It has also been shown that the ratio of network parameters can be found empirically from data [53]. If a single parameter is known, this ratio can be used to find the other parameter in the parameter pair [43]. Both these methods are good predictors for the network parameters but do not give an indication of the variation in the parameters.

Ensemble estimation not only allows for improved prediction but also gives an estimate of variation. The proposed method produces a much larger set of α and β parameter pairs from the same dataset. This then allows us to generate a distribution instead of a single value. Still using the basis approximations of the system, the empirical method allows for more accurate modelling than an analytical alternative. Many links in the GIC modelling chain, such as the geoelectric field derivation, have associated errors that are ultimately absorbed into the empirically defined network parameters and their corresponding distributions (see Section 5). The empirical nature of the method would also absorb non-linear factors relating to the complex nature of the network, such as possible inductive effects. An analytical method has a limited set of input parameters that cannot take into account any of these other effects. An example of this is the lack of quality information available from network operators regarding the exact configuration of the network. This information is vital for analytical modelling but is not needed with an empirical approach and enough data. Studying the parameter distributions can lead to insights about the system and can be used as a general tool for analysis. This fits into an analogy often used in the field - we have a fantastic (but 'uncalibrated') antenna in the power network [27, 30] that allows us to look at the current systems both above and below the Earth's surface.

In order to solve the simultaneous equations correctly, we would need to identify relevant and comparable pairs of time instances. In this case this means that the network has not changed significantly

during the events that typically span 2-3 days (need instances to be 'comparable') and that there is significant GIC data available (need instances to be 'relevant'). Initially, we assume 'comparable' to only relate in terms of network stability, but as shown in Section 5.2 there may be other considerations. Ensemble estimation is then done separately for each event. Since the network has remained stable for over the course of all the events, the results from each event are added together to form the final ensemble. This methodology ensures comparable time instances are used, and has the added benefit that the computing required is decreased for substations with a lot of data (i.e. HYD), since the number of matrices to solve grows as n^2. In order to make sure the data is relevant, selection through criteria is used. In previous work, thresholds have been used to define the criteria [36]. This was done to make sure the calculations are out of the noise. In this work we introduce percentile selection in addition to the typical threshold selection methods (see Section 5.2).

The actual procedure for selecting significant data is common to both this work and previous work. Firstly, significant GIC data are selected, using some criteria. Then the corresponding geoelectric field data are selected to create a set of significant data. In the near-zero crossings approach and least squares fit, it was important to select the relevant geoelectric field to prevent divergent results. In the case of ensemble estimation we are solving a matrix of simultaneous equations. There are times where the matrix itself would be singular (i.e. determinant of is zero and the matrix is non-invertible), which can be avoided if the dataset is masked correctly. That said, ensemble estimation uses all possible pairs of comparable and relevant time instance pairs to calculate parameter pairs, which produces a large ensemble of parameters. This means we can afford to ignore the few cases of singular matrices without implementing any selection at all. Since no missing or zero-valued geoelectric field data is used in any case, the occurrence of singular coefficient matrices is limited to when the geoelectric field for the two time instances used are either exactly aligned or anti-aligned. This can be seen from the geometric interpretation of the determinant. Given two vectors (such as the two geoelectric field vectors), the determinant of these is defined as the area of the parallelogram formed by the vertices (0,0), $(E_x(t_i),E_y(t_i))$, $(E_x(t_j),E_y(t_j))$ and $(E_x(t_i)+E_x(t_j),E_y(t_i)+E_y(t_j))$. If these vectors are aligned or anti-aligned, then the resulting area is zero, as is the determinant. Taking into account almost all possible cases of the system prevents any sampling bias though, an example of which comes from the near-zero crossings approach [36]. Sampling according to specific geoelectric field characteristics causes an inherent directional bias (in this specific example, the NE-SW and NW-SE directions being under sampled compared to the main N-S and E-W directions). These considerations and the development of an empirical approach to network parameter estimation addresses research questions RQ1, RQ3 and RQ4 respectively.

4 Model Application

In order to apply this ensemble estimation model, there are a number of steps that have to be highlighted (and have a direct link with research question RQ4). A model is only as good as the input data. This data comes with its own conditions and considerations. In this work, the ensemble estimation model is implemented for two different nodes in the South African power network during a period when the network was stable. Along with these two nodes, magnetometer data from Hermanus was used. Given different factors, such as network nodes, time period and magnetometer-node combinations, the model will perform differently. It is important to specify these factors and any other conditions used in data selection explicitly. The model must be reproducible for other scenarios. As is seen in previous work, empirical results are sensitive to the data used and any bias must be minimised. Since the method is empirical in nature the result is defined by the data used. When measuring performance of the result, it is important not to use data used in the model that generated the result. This would result in over-fitting and an artificially high level of accuracy.

4.1 Data Sources and Conditioning

GIC measurements from two substations in the South African power network, Hydra (HYD) and Grassridge (GRS), were utilised. The network layout is plotted in Figure 16. The 2-second GIC data is obtained from a transformer neutral line. The GIC data available corresponds to 7 geomagnetic events listed in Table 2. As defined in Section 1, a major global geomagnetic storm is defined as when SYM-H drops to below -100 nT [23, 66]. SYM-H data is obtained from the high resolution OMNI dataset (`https://omniweb.gsfc.nasa.gov/`). To include the storm recovery and commencement, we use an intermediate threshold of -20 nT and a look back time of 1 day. This intermediate threshold means that for a period which is identified as a storm, we include all the time from when the ring current first dropped below -20 nT to when it recovered to above -20 nT. To include the positive signature of sudden storm commencement, we make use of the look back time before the period as defined by the thresholds above. In this look back time, we find the minimum value of the ring current and then include 12 hours before this. Applying these criteria there may be more than one global geomagnetic storm during a selected event. Apart from a globally defined disturbance, a local (Hermanus) geomagnetic disturbance is commonly defined by K-index of ≥ 4. Both these conditions are satisfied for the selected geomagnetic events and ensure there is continuous disturbed time.

Event	Start Date	End Date
Event 1	2001/03/31	2001/03/31
Event 2	**2003/10/29**	2003/10/31
Event 3	2004/11/06	2004/11/11
Event 4	2005/01/19	2005/01/22
Event 5	2005/05/15	2005/05/16
Event 6	2005/08/24	2005/08/25
Event 7	2005/09/10	2005/09/13

Table 2: Data from 7 different geomagnetic events was used. The first day of the Halloween Storm (bold) is used as a validation set for modelling.

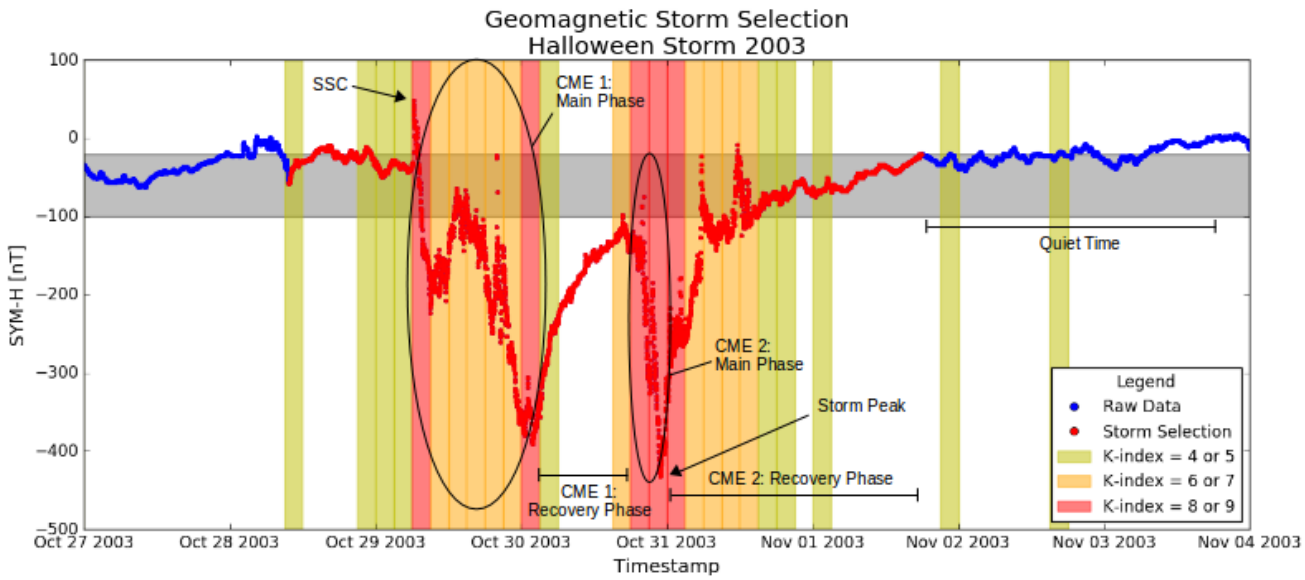

Figure 22: The SYM-H storm selection algorithm (with selection thresholds represented by the grey shaded region) is shown here, using the Halloween Storm of 2003 - also shown are the different storm phases for this more complicated storm and the local K-index at Hermanus. The storm is of interest since a number of different flares and CMEs contribute to the resulting geomagnetic storm [15, 70].

The GRS and HYD substations make up part of the 400 kV network. These high voltage lines are long enough (of the order of a few hundred kilometres) for significant GICs to be induced (of the order of a couple of amps to tens of amps given the right conditions) [31, 21]. In lower voltage sub-networks, the network is more complicated over shorter distances with many grounding points. This results in weaker GICs and for this reason the lower voltage networks are not included in this analysis [60]. It should be noted that power systems, even the more restricted high voltage networks, are exceptionally complicated and dynamic. There is no way to perfectly model all the components in the system, which includes assortments of different transformers and more. An example of this is at HYD, where there is more than one transformer (7 in total with no two exactly the same). This has an effect on the data obtained. To get the GIC in the transmission line itself (not the transformer), a scaling factor would have to be included. GRS on the other hand has only one auto-transformer and various other step down transformers. The leakage from the auto-transformer will have a small, but negligible effect on the GIC measurement. It should also be noted that the GIC measured in the neutral of an auto-transformer is not a true reflection of the state of the core. GICs in this case do not terminate at a grounding point, but may bypass the transformer via a common winding to the next transformer. The measured GIC may in this case be only a fraction of the GIC in the series winding. A strength of empirical modelling is that all these complications are absorbed and do not have to be explicitly modelled. Luckily, both substations are very stable. This stability is a result of the main north-south transmission lines in South Africa feeding to the east at HYD ending in a node GRS. No other lines are available and as a result network switching is very unlikely, since that would leave a lot of people in the dark (see Figure 16). In general though, network switching or other changes must be acknowledged as a source of uncertainty [30].

Geomagnetic data is collected from the Hermanus (HER) magnetometer station in South Africa, about 600 km from GRS and 610 km from HYD. 1-minute resolution data is available from INTERMAGNET (`http://www.intermagnet.org`). The geoelectric field is derived from this data. This procedure is covered in Section 4.2. It should be noted that the measured GIC data has a 2-sec resolution and is down sampled to 1-min to be comparable with the derived geoelectric field. This is done by using a 1-min average, which is intrinsically the same approach used when the magnetic

field is measured. Table 3 lists both the magnetometer and substation positions with the relevant events for each.

Name	Type	Lat	Lon	Data Span
Hermanus (HER)	MAG	34.42°S	19.22°E	event 1 - event 7
Grassridge (GRS)	SS	33.74°S	25.64°E	event 1 - event 2
Hydra (HYD)	SS	30.71°S	24.09°E	event 3 - event 7

Table 3: Data from one magnetometer and two power network substations are used in this study. Geographic position and corresponding data intervals are listed for each station.

4.2 Geoelectric Field Derivation

Deriving the geoelectric from geomagnetic field observations requires an understanding of the driving current systems as well as the conductivity of the Earth. The nature of both these requirements is not accurately known and we have to make use of simplifying assumptions. Extending the initial assumption that the geomagnetic field is a plane-wave and that the conductivity of Earth solely depends on depth, we can make use of the basic magnetotelluric equation [12, 63]. This equation relates the horizontal components of the geomagnetic field, B_x and B_y (being the northward and eastward components respectively), to the induced geoelectric field, E_y and E_x, in the frequency domain. Specifically,

$$E_x(\omega) = \frac{Z(\omega)}{\mu_0} B_y(\omega) \qquad \text{and} \qquad E_y(\omega) = -\frac{Z(\omega)}{\mu_0} B_x(\omega). \tag{46}$$

Here, μ_0 is the permeability of free space and $Z(\omega)$ is the frequency dependent impedance. The most basic form of the magnetotelluric equation makes use of uniform conductivity of the Earth. This can be extended to a 1D layered Earth model of the conductivity where the different layers are assumed to be uniform and are defined solely by depth [53]. This is encoded in the impedance $Z(\omega)$. This impedance is multiplied with the frequency dependent geomagnetic field (a Fast Fourier Transform or FFT is applied to the geomagnetic time-series) to estimate the geoelectric field components in the frequency domain [73]. To obtain the geoelectric time-series, in inverse FFT is applied. Typically, a short time-series is distorted at the edges when taking an inverse FFT (Gibbs phenomenon). In order to limit this distortion, the data that is processed is padded. A day of data is added before and after the day of interest (4320 data points). This is then clipped to a time-series with $N = 2^{12} = 4096$ data points. Once in the time domain, a Parzen window of the form,

$$w = 1 - \left[\frac{\{1, 2, ..N\} - N/2}{N/2} \right]^{2m} \tag{47}$$

is applied to the data, where N is the length of the clipped time-series and $m = 4$. After this conditioning, only the central day of day of interest is extracted, resulting in the geoelectric field used [34].

For lack of a conductivity profile at HYD, the frequently used 5-layer Québec profile (1D layered Earth model) [10] is applied in the geoelectric field calculation. This profile has layers with thicknesses of $d = [15, 10, 125, 200, \infty]$ km and corresponding layer resistivities of $r = [20000, 200, 1000, 100, 3]$ Ω·m. The resulting magnitude of the surface impedance is close to the locally derived profile at GRS [43]. Specifically, the two resulting surface impedances are comparable in terms of magnitude (see Figure 23) [34]. The local profile is more complicated with a conductivity profile consisting of 10 layers that was obtained by applying Occam's inversion algorithm to the derived apparent surface impedance [53]. Previous studies of different conductivity profiles, specifically at GRS, have shown that the choice of impedance profile has a significant effect on the accuracy of GIC modelling [36]. We make

a similar comparison between the non-local Québec profile and local GRS profile in terms of network parameter estimation. In this work though, the main focus is on improving network parameter estimation and the Québec conductivity profile suffices for relative comparisons. The other relevant input parameter to consider is the geomagnetic data. For correct GIC modelling, the derived geoelectric field should use local geomagnetic data in the vicinity of the substation [4]. In this case 'local' refers to a spatial scale of roughly 600 km in the east-west direction and 300 km in the north-south [42]. Both substations in this case are within an acceptable (but very borderline) distance from the HER magnetometer.

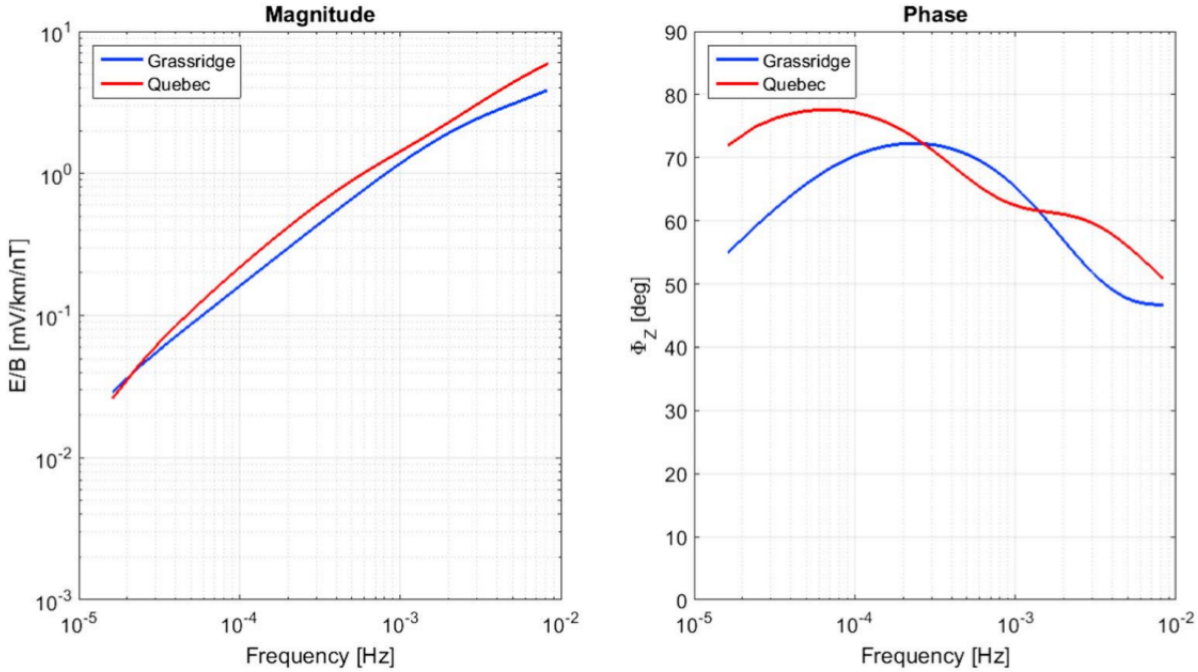

Figure 23: Comparison of the magnitude and phase of the surface impedances for the Québec and Grassridge conductivity models [Image credit: Lotz et al. [34]].

4.3 Model Flow

After data selection and conditioning, we can apply the model. All coding was done in `Python`, with the simultaneous equations defined by time instance pairs solved using the `Numpy` library with its `linalg.solve()` method. Due to the extent and time-series nature of the data, `Pandas` dataframes were used for processing. All plotting was done using the `Matplotlib` library. Further fitting (expanded further in Section 5.1) of the resulting probability distributions were also done using the `Scipy` library. The `stats` module, which includes a Cauchy fitting routine, was used to define the scale and location parameters of the distributions. The FWHM, which is also used as a measure of the scale parameter of the distribution, was calculated using a spline fit as defined by the `interpolate` module and `UnivariateSpline()` method. Before moving further, an out-of-sample validation set was selected to be used to model the results of the ensemble network parameter estimation (see Section 6.3). This is done to avoid any over-fitting bias. Using the rest of the data, the model was implemented for each of the events (see Table 2) separately. The results for each were then merged into one global set of results for the specific network node.

At this point, we have the measured GIC data which has already been down-sampled to match the geoelectric field data (that has been derived from corresponding geomagnetic data). Assuming a single event, the first step is to make sure that the GIC data is relevant. Relevant in this sense means that the data is (i) well defined and calibrated and (ii) associated with geomagnetically disturbed time. The first point of the GIC data being well defined and calibrated stems from the fact that there

is little control over the environment in which the data is collected. Previous data has had a time or voltage off-set that has rendered the data untrustworthy. Given bad data quality, the data has to be discarded. General tests were done to ensure that the data quality was acceptable. This included looking for outliers and discontinuities, plotting a distribution of the GIC magnitudes and verifying the shape of the distribution. The timing of the data was checked by comparing initial GIC spike to the SCC spike in the geomagnetic data. The data used passed all these tests. The second point stems from what the overall goal of the modelling is. GICs have been shown to be correlated with geomagnetic disturbances and specifically geomagnetic storms. This means that the empirical model needs to use this specific type of data to be able to be relevant in GIC modelling with unseen out-of-sample geomagnetic disturbances. Typically, there are more quiet days than disturbed days, and not implementing this condition would result in a bias towards quiet days and decreased accuracy when modelling storm days. All the data comes from disturbed periods, as defined from either the global SYM-H index or the local K-index (often with an overlap).

The criteria for selecting relevant GIC data can be extended further. Even during disturbed time, there are instances where the GIC response is low and close to quiet time levels. Since we want to model cases of extreme GICs accurately, the lower level GICs are effectively noise. To get away from this noise previous work has defined an absolute threshold to select only relevant GIC data. This is implemented in this work as well, but with the added flexibility of a relative threshold as defined by the data (see Section 5.2). This is needed since the measured GIC may be only a factor of the true line GIC. A relative threshold will absorb this, whereas an absolute threshold may not. If the exact network configuration is not known, then the measured GIC cannot be appropriately scaled and an absolute threshold may inaccurate. Ultimately though, some further criteria are needed to define relevant GICs to be used in modelling.

With relevant GIC data defined by some selection criteria, the corresponding geoelectric field data has to be selected. This is done purely using the timestamps as indices for both time-series. Using the indices from the relevant GIC data, the corresponding geoelectric field data can be selected as well. After geoelectric field selection, there will be are cases where the geoelectric field is not defined (i.e. missing data) or not significant enough (i.e. close to zero magnitude) for a GIC data point. As a result, a similar process of index selection is needed to select all the corresponding data points from the relevant GIC data before solving. In previous work, the geoelectric field data was also selected according to further criteria as defined by the different methods. Since the simultaneous equations do not need any specific zero crossings or such, no selection criteria is used, besides the fact that either of the geoelectric field components must be non-zero (to be significant enough to be used in calculations). If a singular matrix arises when solving (resulting from specific cases as described in Section 3.3), instead of using a least squares fit routine to find the best possible solution and risking a divergent or undefined result, the time instance pair is ignored.

This process results in two comparable subsets of the original GIC and geoelectric field data. Now, we iterate through all possible pairs of time instances and solve for the network parameters. The results are saved in a dataframe (which in turn can be saved as a binary file) along with the associated timestamps, GIC values and geoelectric field values. This is done for the sake of possible post processing. After this entire process is completed for each event, the results can be merged into a single result for a given network node. Following from this, the network parameters are extracted and the resulting ensembles analysed (through plotting and fitting). Using the results of the analysis, the out-of-sample validation set can be modelled and the performance of the model measured.

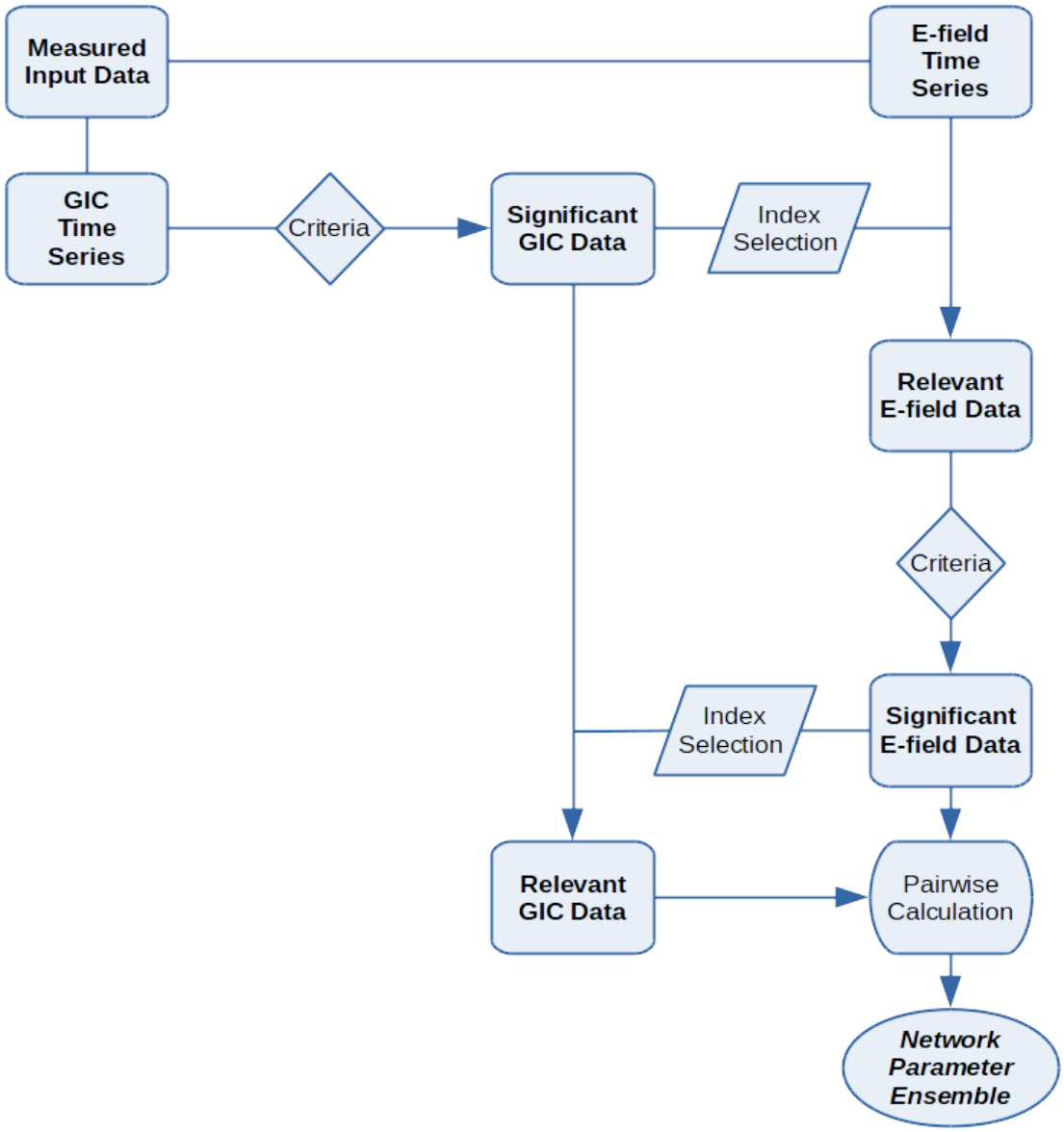

Figure 24: General process flow of ensemble estimation - with emphasis on how the corresponding datasets are selected (from which all possible pairs are sampled)

4.4 Further Considerations

As is the gripe of many a researcher doing experimental work, there could always be better data. This is not the only point to bear in mind. Briefly summarised, the following factors affect the implementation and performance of the model:

1. *Limited data:* First and foremost is the question of data availability. In this work, GIC data from only two substations was available. Furthermore, this data only spanned 7 geomagnetic storm events. Luckily, the events included the Halloween Storm of 2003, which is known to have had adverse effects on transformers in the South African power network [31, 21]. GIC modelling on the other hand has only been done at Grassridge for this specific storm, and is the only case study where results can be compared to. There was only one other event with GIC measurements at Grassridge, limiting the data used to derive the network parameters. Hydra has measured data for 5 different events between 2004 and 2005. Since no previous modelling was done using this substation, this is used in general analysis of the GIC and

network parameter behaviour. In order to validate an entire network model and behaviour during different storms, more (and reliable) measured data is needed.

2. *Improved temporal resolution:* The measured GIC data has a 2-sec temporal resolution. The INTERMAGNET magnetometer data on the other hand has a 1-min resolution. Modern magnetometers (since the period in question) now have a resolution of 1-sec. Using this data to derive the geoelectric field and averaging to 2-sec data would increase the amount of data available and also take into account higher frequencies, which may be of importance during extreme events.

3. *Network changes:* Since 2005, the South African network has changed significantly (although during the period between 2001 and 2005 the network was stable in the region analysed). The empirically derived results of this period are thus not necessarily the same as what they would be now. Ultimately, new network parameters must be estimated.

4. *Conductivity profiles:* The derivation of the geoelectric field is critical to the model as it relates the network parameters to the GIC. More specifically, the surface impedance derived from a conductivity structure is important. Up to now, modelling has been done using increasingly complicated conductivity profiles. All of these are still based on assumptions of ground conductivity or empirically derived apparent surface impedances, with no measured surface impedances. Since 2005, there have been a number of magnetotelluric (MT) stations installed in different parts of South Africa. The results of these may help to fix the conductivity profiles in future work.

5. *Locality:* The location of the network nodes and magnetometer station is important in the model, since the results are defined by the data used and unique to the pair. The combination of Hermanus and Grassridge or Hydra is on the borderline of what is acceptable in modelling [42]. For any pairs separated by larger distances, an interpolation scheme should be used for the geomagnetic data [4]. Furthermore, this work is done at mid-latitudes. Applying the model at higher latitudes, where the plane-wave assumption is no longer as valid, may introduce additional uncertainty.

6. *Governing assumptions:* Another consideration to take into account is the assumption of a resistive network, constant network parameters and the uniform geoelectric field. Power networks are generally designed so that the inductance and capacitance effects are limited, making the network close to restive at power frequencies. At quasi-DC GIC frequencies, this may not always be the case. This possibility is not covered in this work. The second assumption is that of a uniform geoelectric field driving the measured GIC. Using an empirical approach, the effect of non-alignment may be absorbed when considering different intensities of GIC measurement. The resistive network assumption along with the plane-wave assumption leads to the assumption that the network parameters are constant. In this work, we assume network parameters are constant for comparable GIC magnitudes to solve the simultaneous equations. Ultimately, as long as there are enough instances close to the plane-wave assumption the network parameters can be solved for.

Although highlighted, in future implementations, certain considerations and limitations may no longer be an issue.

5 Ensemble Estimation Results

After applying the model and producing an ensemble of network parameter estimates, the most probable network parameters can be estimated. This is done by finding the peak of the probability distributions produced (which are just normalised ensembles). The distributions themselves can also be analysed and network parameter behaviour quantified. Furthermore, the results can be analysed for consistency with the underlying theory.

5.1 Network Parameter Distributions

As a start, we first will apply the ensemble estimation of the network parameters for the same substation and using the same data as used by Matandirotya et al. [36]. Ultimately, we want to compare the ensemble estimation method and resulting GIC modelling performance with previous work (which will specifically answer research question RQ2 in this case) so it is important to use the same data and selection conditions where applicable. The first of these deals with the GIC data measured at GRS over the Halloween Storm of 2003. Matandirotya et al. defined the condition $|GIC| > 0.1 \times RMS(GIC)$ to select relevant GIC data. Here $RMS(GIC)$ is defined by,

$$RMS(GIC) = \sqrt{\frac{\sum_{i=1}^{n} GIC(t_i)^2}{n}}. \tag{48}$$

Matandirotya et al. went further to select instances of the geoelectric field where either geoelectric field component was near-zero and could be neglected. These zero crossings could then be used to estimate the network component related to the non-zero geoelectric field component directly (see Section 2.2 for more detail). On the other hand, as mentioned in Section 4, none of this further data selection is needed for ensemble estimation. The only condition applied is that comparable time instances are used (no network changes). In order to ensure this is the case, a single geomagnetic event is processed at a time. the results from each event are then merged into a result set. In terms of the derivation of the geoelectric field data to be used, Matandirotya et al. made use of a locally derived conductivity profile for GRS. The geomagnetic field data used in this derivation was either HER magnetometer data or interpolated geomagnetic field data. In the case of this work, only HER magnetometer geomagnetic data was used in the geoelectric field derivation since it has been shown to be 'local' enough for GIC modelling [42]. In this work, we apply the local GRS conductivity model, but also introduce a non-local conductivity model (specifically since HYD does not have any local conductivity profile defined). The geoelectric field derivation is assumed to be a source of uncertainty (see Section 3.3) and this should be seen in the comparison of the distributions resulting from the different profiles. As one of the main objectives is to measure the performance of ensemble network parameter estimation in actual GIC modelling, this work keeps GRS data from the 29th of October 2003 out of the estimation process to be used as an out-of-sample dataset (not done in previous work). The results of GIC modelling using this dataset along with the ensemble estimated network parameters can be compared to the results obtained by Matandirotya et al. and the performance of the model quantified. That said, Figures 25 and 26 are normalised histograms of the resulting ensembles, calculated using the data as described above. These normalised histograms can be thought of as PDFs of the different network parameters.

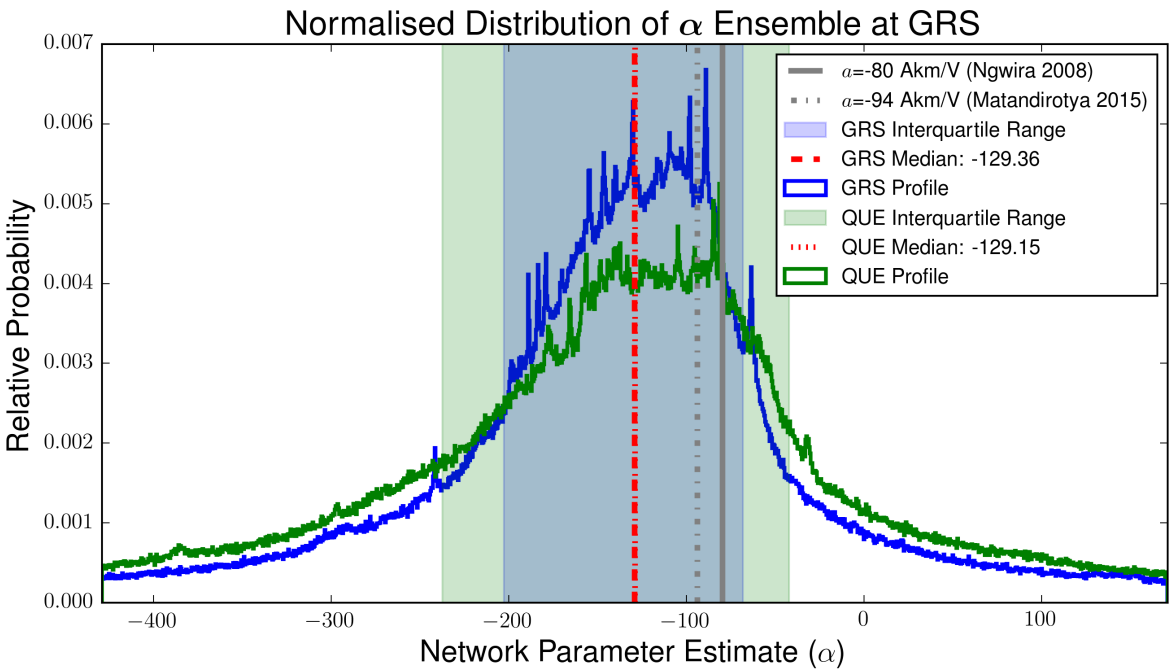

Figure 25: Comparison of the $\boldsymbol{\alpha}$ distributions derived from the local and Québec conductivity profiles. This behaviour also holds for the $\boldsymbol{\beta}$ distribution. The interquartile range shown is used to model a prediction band (Figure 28). Also shown are the network parameter estimates from previous work.

Since the result of ensemble estimation is a distribution, the central tendency is used to estimate α and β. At a first glance, the general distributions seem bell-shaped. One cause of the spread has already been identified as the associated error from the geoelectric field. The most obvious approach given this shape would be to try and fit a normal distribution, since measurement errors are typically normally distributed. In the case of a normal distribution, the mean is a good estimate of the central tendency, but is otherwise significantly biased by outliers, skewness or heavy tails. In the resulting ensembles though, this fit is in fact not possible at all since the variance is not well defined. Taking the entire $\boldsymbol{\alpha}$ and $\boldsymbol{\beta}$ ensembles, each with 2 118 711 estimates using the GRS conductivity profile and 2 124 891 using the Québec profile, we have variances of 1.9×10^{10} and 3.7×10^{10} (GRS) and 1.2×10^{11} and 1.3×10^{11} (Québec) respectively. Similar undefined results are obtained for the higher order moments of skewness and kurtosis. Kurtosis is of particular interest since a kurtosis of more than 3 suggests the distribution is heavy-tailed or leptokurtotic. This means its tails of the distribution asymptotically approach zero more slowly than those of a normal distribution due to a greater influence from outliers and extreme values. The kurtosis for all the ensembles blows up (order of 10^5 and greater) in is in fact undefined. All of this points to the fact that the resulting distributions are heavy-tailed distributions, which are known to have undefined statistical moments. The distributions displayed in Figures 25 and 26 are defined by clipping the ensembles to values within 300 A km/V of the central peak, with 1 200 bins in the histograms (a bin width of 0.5). These clipped ensembles still have over 1.7 million estimates for the GRS conductivity profile and 1.6 million estimates for the Québec profile. Looking at the statistics defined by these restricted distributions (which are less influenced by divergent extreme values), see that the variances are still undefined, being of the order of 10^4 A km/V given only a range of 600 A km/V. For heavy-tailed distributions, the median is a much better measure of central tendency as it remains relevant for skew and heavy-tailed distributions [17].

The true nature of the distributions is more accurately described by the Cauchy distribution. In a Cauchy distribution, the mean and all higher moments are not well defined if at all (as observed). Both the normal distribution and the Cauchy distribution are specific cases of the more general family of distributions - the stable distributions [45]. In this family, the only non-heavy tail distribution

is the normal distribution. The most general form of a stable distribution includes parameters that allow for tail thickness and 'skewness', although this is not needed to find the most probable value (and are very computationally intensive to fit). This type of distribution has application in the field, but not in the same context. It has also been shown that the electric and magnetic fields produced at Earth's surface resulting from a line current I at height $h + a$ are identical to those from an ionospheric current at height h with a Cauchy-distributed current density with a half-width a [9]. This type of distribution takes the median and half-width at half-max of the distribution as location and scale arguments respectively. The results of this fit are shown in Figure 26. In this fit, a spline interpolation is used to approximate the FWHM. These initial estimates form a starting point for a fitting routine is used to fit a Cauchy PDF to the probability distribution. This then improves on the scale parameter estimate, while hardly changing the location parameter estimate as defined by the median. Although the fit may not seem too accurate, it provides a relative measure of the spread and an accurate location of the peak/most probable value. This is used for later analysis (see Section 5.2).

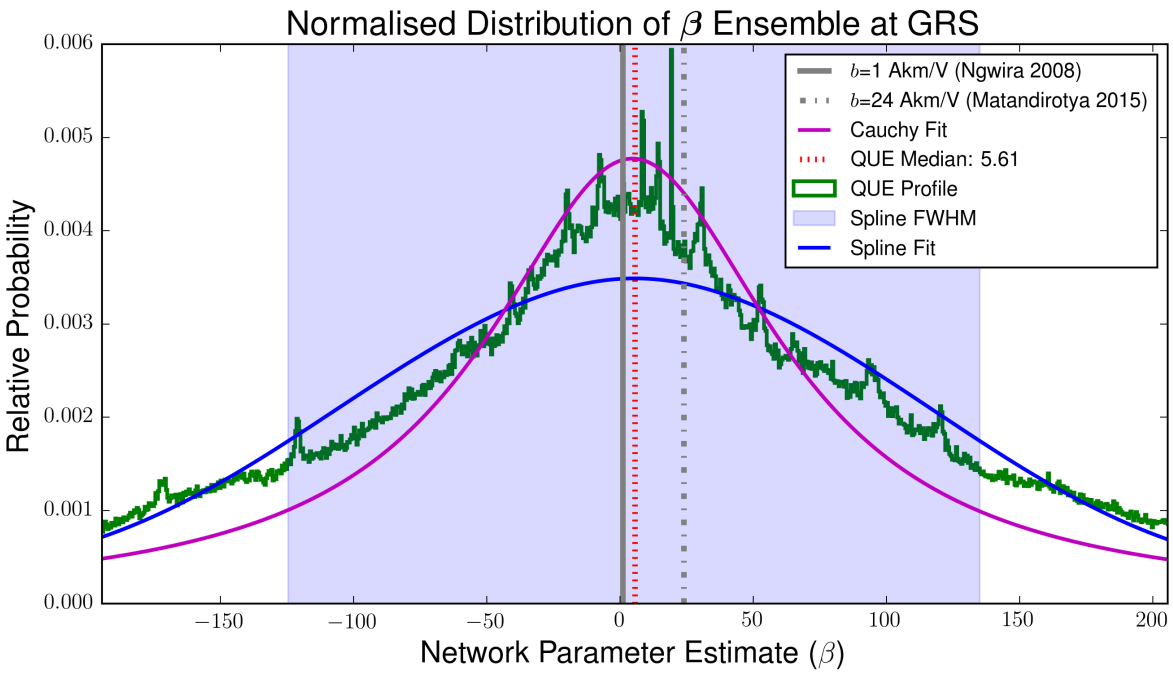

Figure 26: The fitting routines to quantify the distributions include a Cauchy and spline fit (along with relative spread as defined by the FWHM of the spline). This is shown using the $\boldsymbol{\beta}$ distribution, but is valid for the $\boldsymbol{\alpha}$ distribution as well. Also shown are the network parameter estimates from previous work.

Knowing how to quantify the resulting distribution and what some of the particular drivers are allows us to improve prediction. A direct result of this is the use of the impedance profile to relate the measured geomagnetic field to the derived geoelectric field. Any errors in this geophysical step of the GIC modelling process would lead to a change in the distributions of $\boldsymbol{\alpha}$ and $\boldsymbol{\beta}$. Using a local impedance at GRS instead of the Québec profile results in narrowed (but hardly shifted) distribution as is seen in Figure 25. The fact that a non-local, but well defined, conductivity profile results in the same network parameter estimation but with a larger spread can be very useful in cases where the conductivity structure of the Earth is not well-known. The significant influence of the change in profile illustrates how errors in the estimation of $E_{x,y}$ from $B_{x,y}$ are collected into the network parameter estimates, as seen in the increased spread. Although a local impedance profile is preferable for accurate modelling, we will be using the local GRS profile for comparative modelling at GRS and the Québec profile in the rest of the analysis for HYD. This first order approximation is sufficient to

measure the relative performance of the ensemble estimation and look at resulting behaviour.

In order to measure the performance of ensemble estimation as a method for network parameter prediction, a comparison is made with the results of two previous studies, namely Ngwira et al. [43] and Matandirotya et al. [36]. Both these studies used GRS GIC data from the first day of the Halloween Storm, 29 October 2003, for GIC modelling. During this day, the period between 06:00 UT and 12:00 UT is highly disturbed according to SYM-H and the period between 19:00 UT and 24:00 UT is relatively disturbed (see Figure 28). Both periods relate to the effects of a single full-halo CME that was emitted on 28 October at 11:30 UT (with an associated X17.2 class flare). Unrelated to this, but evident in Figure 22 is a second CME that slammed into the Earth's magnetosphere during the recovery phase of the initial geomagnetic storm on 30 October. This second CME left the Sun on 29 October at 20:54 UT and had an associated X10.0 class flare [15]. The second period of disturbed time in the initial geomagnetic storm is a result of a change in the B_z component to southward after an initial northward recovery [70]. Regardless of this, both previous studies identified these times as particularly active periods and looked at the performance of modelling of these periods separately in addition to the entire day. This work will also follow the same approach and the two periods, 06:00-12:00 UT and 19:00-24:00 UT, will be referred to as the Primary and Secondary Storm Phases respectively.

Both Ngwira et al. [43] and Matandirotya et al. [36] derived network parameters empirically (to some degree), which improved on previous estimates (see Section 2.2). In the second study, Matandirotya et al. made use of the finite element method (FEM) to further improve the derived geoelectric field results. The geomagnetic data used for this included HER magnetic data and interpolated magnetic field data to get a better local estimate for GRS. The interpolated data came from two South African observatories, namely Hermanus (HER) and Hartebeeshoek near Pretoria. The HER magnetic data and finite element method derived geoelectric field result is referred to as FEM 1 and the interpolated magnetic data and finite element method derived geoelectric field is referred to as FEM 2. Matandirotya et al. then used both sets of improved network parameters to test the two FEM geoelectric fields. The final two network parameter sets will be referred to as the 'Ngwira Set' and 'Matandirotya Set' respectively. These parameter sets, along with the results of the previous studies are summarised in Table 4.

Keeping in line with the previous work, the validation set used to measure performance of the ensemble estimation method is also GIC data from the 29th of October 2003 as measured at GRS. The other data available for GRS is used for ensemble training. In addition to this, this work includes the Québec profile in ensemble estimation. This is purely to look at the different behaviour of profiles in the ensemble estimation method and allow for further comparison and analysis. For both cases, the threshold used to select significant GIC data is the same as that used by Matandirotya et al., namely $|GIC| > 0.1RMS(GIC)$.

Besides the *RMS*, which acts as a data dependent threshold, we also make use of different error metrics. These metrics measure the performance of the modelling for both storm phases as well as the total validation set. The first is an extension of the above, namely the *RMSE* or Root Mean Square Error of the model,

$$RMSE = \sqrt{\frac{\sum_{i=1}^{n} (GIC_{obs}(t_i) - GIC_{mod}(t_i))^2}{n}}. \tag{49}$$

It should be noted that for modelling, error metrics need to be applied to an out-of-sample validation set. This was not done in previous work and should be kept in mind when comparing performance results to the current work. The *RMSE* metric is further supplemented by the *RE* or Relative Error,

$$RE = \frac{GIC_{obs} - GIC_{mod}}{GIC_{obs}}. \tag{50}$$

Using the previous work's definition, only the median *RE* for $|GIC| > 1$ A is considered. The *RE* can be shown as a percentage.

Where the *RMSE* and *RE* both quantify the error in absolute amplitude, Pearson's correlation coefficient ρ quantifies the correlation. In order to measure the performance of both aspects, we create a hybrid error metric (*HE*) which is a combination of the above. This is purely defined for convenience in this work and uses the properties of the other error metrics for relative comparisons in performance. The hybrid error uses a normalised and weighted *RMSE*. This is as a result of the aim of GIC modelling to model the extreme cases where power networks are most likely to be affected. The normalised and weighted *RMSE* is thus penalised more for doing badly at higher absolute magnitudes and denoted by *RMSE*′,

$$RMSE' = \frac{1}{\max(|GIC_{obs}|)} \sqrt{\frac{\sum_{i=1}^{n} \left(\frac{|GIC_{obs}(t_i)|}{\max(|GIC_{obs}|)}\right)\left(GIC_{obs}(t_i) - GIC_{mod}(t_i)\right)^2}{n}}. \tag{51}$$

Combining the normalised and weighted *RMSE*′ with the correlation coefficient, ρ, the *HE* is obtained,

$$HE = (1 - RMSE') \times \rho. \tag{52}$$

The *HE* metric varies between -1 (completely wrong), 0 (as bad as random) and 1 (perfect).

Data	RMSE [A] (ρ) 06:00-12:00	19:00-24:00	00:00-24:00	RE%	Hybrid Error
Ngwira Set (a=-80, b=1 A km/V)					
FEM 1	0.96	1.07	1.35	51	-
FEM 2	0.97	1.14	1.31	55	-
Matandirotya Set (a=-94, b=24 A km/V)					
FEM 1	1.38	1.11	0.98	41	-
FEM 2	1.41	1.21	1.02	47	-
Grassridge (GRS) Profile (α=-129.36, β=7.90 A km/V)					
	1.42 (0.88)	0.54 (0.97)	0.86 (0.88)	30	0.856
Québec Profile (α=-129.15, β=5.61 A km/V)					
	1.78 (0.78)	0.81 (0.93)	1.12 (0.79)	35	0.756

Table 4: Ensemble estimation results are compared to previous work. Three different error metrics are used after the resulting network parameter estimates are applied to a validation set. Specifically, the *RMSE* and correlation coefficient (not used in previous work) are calculated for the different storm phases as well as the entire validation set. The relative and hybrid errors are shown for the entire validation set.

From the defined error metrics we see an improvement in GIC modelling in almost every aspect when compared to previous work. This improvement is seen even though the modelling was done on an independent validation set that was not used in the ensemble estimation. In the previous work, the empirically estimated parameters did better than the analytically estimated parameters given the whole day, but not during the significantly disturbed times. Comparing the use of different impedance profiles, the associated geoelectric field error does not affect network parameter estimation given enough data but does have an effect on the modelling of the GIC. Using the local conductivity profile does better as measured by the error metrics. This improvement in the error

metrics is directly related to a more accurate geoelectric field and not network parameters. Using the same conductivity profile (GRS) as in previous work, there is more than a 10% improvement in the relative error throughout the day and the RMSE is halved during the Secondary Storm Phase. The only shortcoming is during the Primary Storm Phase where the RMSE is marginally greater than in previous work. Even using the non-local Québec conductivity profile shows improvements compared to previous work in all aspects but the RMSE of the Primary Storm Phase. The results are summarised in Table 4, along with the α and β estimates for the GRS and Québec profiles.

5.2 Dependence on GIC Magnitude

The ensemble method produces many network parameter estimates collected in $\boldsymbol{\alpha}$ and $\boldsymbol{\beta}$. This allows for a more stringent data selection procedure to be followed. Using a general *RMS* as a threshold to select GIC is a good approach to exclude noise, but is relative to the dataset. Given the system configuration at HYD, the measured GIC is a fraction of the transmission line GIC and relatively small (mean of absolute GIC magnitude is roughly ≈ 0.3 A) and the distribution of GIC values relatively narrow. This results in the *RMS* condition straying closer to the typical noise than when compared to GRS where the GIC distribution is more spread. At GRS, since there is only one autotransformer, the GIC in the transformer neutral is larger (mean of absolute GIC magnitude is roughly ≈ 0.9 A). Although this is an autotransformer, which is not grounded (resulting in the measured GIC being smaller than the GIC in the transmission line), the measured GIC is still closer to the GIC in the transmission line than the fractional GIC at HYD. Instead of a relative threshold such as the RMS which can be affected if not enough is known about the system, we can use a data defined absolute. An example of this would be to use percentile levels. Taking all the available measured GIC data for a site, we can define thresholds based on percentile levels. In this case, the given percentile level is absolute for all cases. The threshold related to the percentile level is not absolute though, since it is defined by the type of data used (relative to the data). Using data for a quiet day only, a high percentile threshold would still be in the 'noise' for modelling extreme GICs. But, if we make use of enough representative data, which would include extreme GIC scenarios, we overcome this. Additionally, the unknown scaling needed because of network configuration is not needed and different substations can be compared, i.e. with enough representative data the percentile ranges correspond to intensities from similar scenarios at each station (although the measured intensities at each station may be very different). Taking percentile ranges as defining different scenarios, these subsets are then processed in the same way as before, calculating estimates for each geomagnetic storm event separately and then merging them back into an ensemble for the percentile range or window. The selected data within each percentile range or window results in a dataset based on GIC intensity and are consistent with all others in terms of the number of time instances used and the type of events spanned. Ultimately, this threshold selection is comparable between a number of factors, including different intensities and different nodes (when normalised).

It has been seen that the empirical estimation of network parameters changes when data defined by different GIC strength thresholds is used [67, 36]. This means the performance of modelling changes with GIC strength. Delving deeper into this observed relationship stems from research question RQ5. Making use of different percentile windows allows us to quantify this behaviour. Grouping the data in this way also ensures that the data is comparable for the calculation of the network parameters, given some driver relating to GIC strength. Separate ensemble estimates are thus made for each percentile window. The only condition for this data selection method is to make sure there are enough time instances in a percentile range to result in a distribution. Taking a 25% percentile window for GRS results in more than 1 million parameters pairs per window and taking a 10% window for HYD results in more than 4 million parameter pairs. These windows are started at the 0th percentile to include the noise and are shifted up incrementally by 5% to span all the data. For each window we then fit a Cauchy PDF to the distributions of $\boldsymbol{\alpha}$ and $\boldsymbol{\beta}$. This allows the scale and location parameters to be quantified along with the normal location and scale estimates of the

median and half-width at half-max (as defined by a spline fit to the distribution) respectively. To obtain the best quantitative result of the location estimate for a given percentile range, the average of the Cauchy PDF location parameter and the median is taken. A similar average is taken for the HWHM (FWHM/2) and Cauchy scale estimates. Arranging the percentile range estimates along increasing values of measured GIC in Figures 27a and 27b show that α and β are apparently not constant and vary with GIC intensity as the storm evolves (since GIC magnitude varies with time).

From the plots of estimated parameters versus GIC magnitude percentile range (see Figures 27a and 27b), we see that for small GICs, the network parameters are negligible. This suggests that the preferred direction is indeterminate for very small GIC and that these cases are often a result of miss-alignment and most likely a small geoelectric field. As the GIC strength grows, the network parameters become more and more relevant. This is not the case with the β parameter at GRS which stays close to zero. This is most likely a function of the directionality weighting from the network. GRS is located at a stable endpoint in the network with only a single, approximately north-south directed, line feeding in (see Figure 16). Therefore the β parameter, which scales the eastward geoelectric field component E_y, is small. This suggests that GICs at GRS are practically independent of the eastward component of the geoelectric field. In previous work, it was suggested that when any network parameter is more than 4 times greater than the other, the resulting GICs at the node would be largely dependent on the geoelectric field direction associated with the greater network parameter (and the other network parameter ignored) [30, 43].

In general, the spread of the distribution first increases with GIC strength and then decreases. At low GIC strength there is hardly any dependence on the parameters (i.e. they can be anything) with a small and unaligned geoelectric field. The resulting distributions are small peaks on top of heavy tails that artificially result in 'narrow' spreads. As the GIC strength increases to intermediate percentiles, the geoelectric field becomes more relevant as well as the directionality, but there is still the case of non-alignment which increases the spread. At the strong GIC thresholds, we have a significant geoelectric field that is largely aligned and the peak sharpens, decreasing the spread. This behaviour is again not seen with the β parameter at GRS where the spread just increases. This is another suggestion that the β parameter and the corresponding east-west direction have no influence at this substation. This result has been reported in previous work, where the β parameter was not well-behaved and varied in polarity. This is a further indication that GICs at GRS are independent of east-west geoelectric fields [36].

When comparing the HYD network parameters to previous work, we see a huge discrepancy. Previously, a and b were estimated analytically to be 25 and -111 respectively [30]. Using ensemble parameter estimation, we see that α tends to 100 and β tends to roughly -60. This discrepancy may possibly be a result of unknown factors in the network that were not taken into account in the analytical estimation of the parameters.

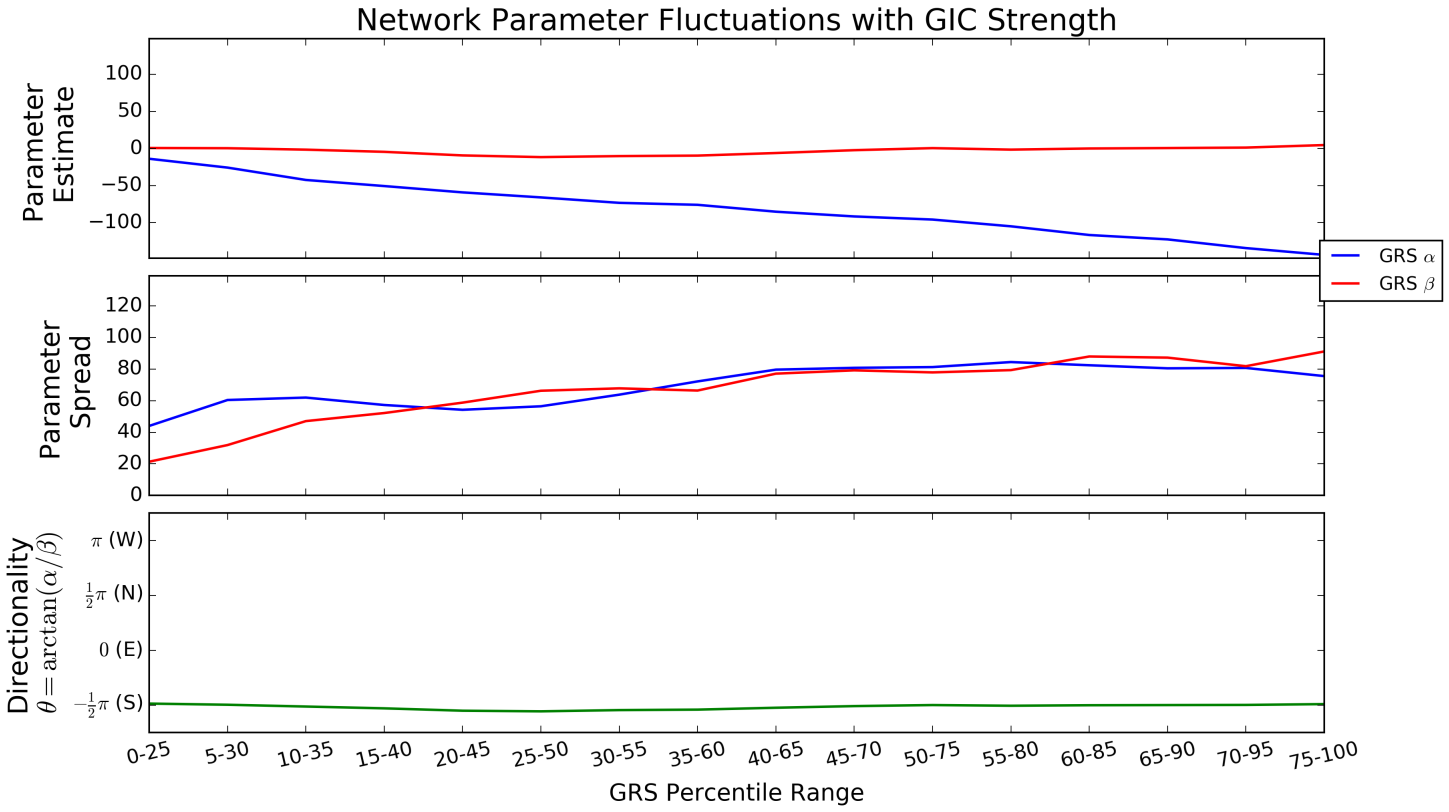

(a) Network parameter fluctuations at GRS.

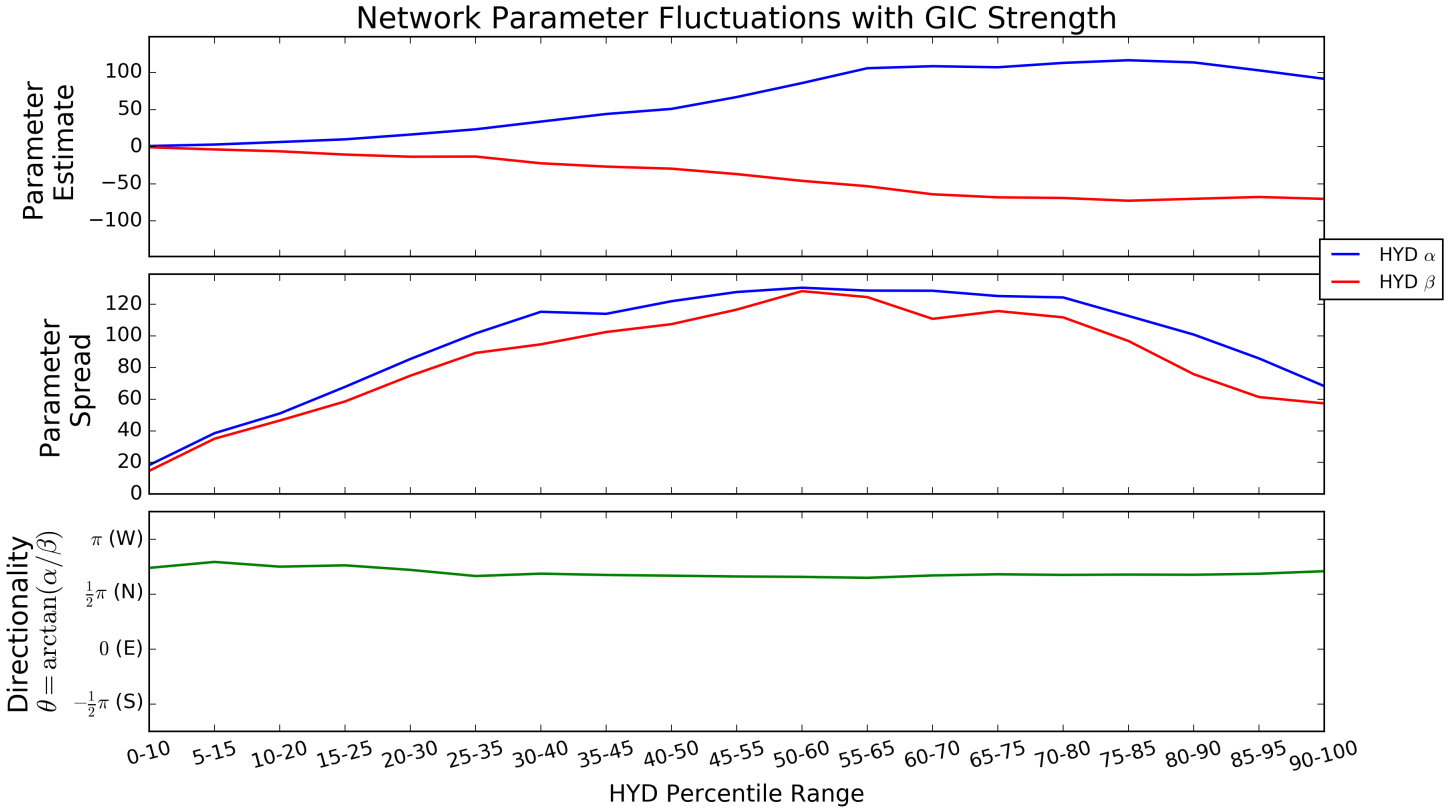

(b) Network parameter fluctuations at HYD.

Figure 27: Plots of network parameter estimates and distribution spreads against GIC strength. Taking the ensemble parameter estimates and calculating the associated directionality, we find this to be constant. This would imply the ratio of the parameters is constant with GIC strength as well.

6 Discussion and Implications

Apart from the results of ensemble estimation and the general improvement they bring to GIC modelling, further factors regarding GICs and network parameter behaviour can be unpacked (see research questions RQ3 and RQ5). The first of these additional insights is that the empirically derived network parameters form a distribution with a certain spread. Since each estimate is a valid state, with a given probability associated to it, a single network parameter estimate may not always be the best. Sampling from a range of estimates may in fact be closer to reality. A further insight is that empirical network parameters vary depending on the GIC magnitudes used to calculate them. This behaviour raises questions regarding the underlying model assumptions. Practically, this behaviour also needs to be taken into account when choosing network parameters for modelling.

6.1 Error Propagation in the Modelling Chain

In Section 3.3, the governing GIC equation was updated to an empirical version that would include the associated errors from the measured GIC data and derived geoelectric field data (and possibly errors in the assumptions or other errors that have propagated through the modelling chain). As has been assumed in previous work, the measured error (GIC and geomagnetic field data) would follow a typical normal distribution with a zero-mean. This is not the case with the derived geoelectric field data where the errors are heavy-tailed. This data is derived in the frequency domain using an impedance profile that is usually obtained from a conductivity profile of the Earth in that area. As seen in Section 5.1, a surface impedance derived from a local conductivity profile produces a sharper network parameter distribution (narrower spread) and indicates less error associated with the profile. A further result from this analysis is that given different conductivity profiles, the location parameter (median) of the network parameter distribution does not shift. This suggests that the network parameters themselves are well defined given enough data and confirms that associated errors contributing to the spread in the distributions are roughly bell-shaped with a zero-mean and a zero-median. Additionally, this suggests that approximate conductivity profiles can still converge to a good result, albeit with more uncertainty. Given more analysis of when convergence is possible for a given conductivity profile, a possible application in the real world is to use a simple convergent profile to derive ensemble network parameters in cases where the conductivity profiles are not known. When considering the change in network parameters (shift in distributions) for different GIC magnitudes (which are indicative of different storm phases), the frequency dependent error in the geoelectric field and error in geoelectric field alignment may be more relevant.

With the network parameters well defined, they can be used in modelling and validating analytical models of GICs in networks. The associated errors that are encoded in the spread of the distributions can be useful as well. Up to now, there has not been any quantifying of the associated uncertainty in the network parameters and for that matter GIC modelling results. The spread in the distributions address the former explicitly and the uncertainty in GIC modelling implicitly. Since the spread takes into account other, non-network parameter related errors, a range of estimates would correspond to a measure of the associated errors. The bounds of such a range, spanning the median of the distribution, can be used for as upper and lower bounds for GIC estimation and ultimately limits of uncertainty associated with the modelled system. This approach of a prediction band can be incredibly useful in forecasting, allowing an estimate of extreme cases along with conventional estimation at any given time.

6.2 GIC Prediction Band

The spread in the distributions of estimated network parameters suggests that using single values of α and β to relate GIC to induced geoelectric field is not correct. Instead of using this approach

(and rather continuing from the previous section), we can use the interquartile range of $\boldsymbol{\alpha}$ and $\boldsymbol{\beta}$ (see Figure 25) to predict an associated range of GICs. This network parameter range would span the typical error propagated in the GIC modelling chain, without straying into the heavy tails. Since we are most concerned about the largest GICs, we then use the values of α and β in this interquartile range that will maximise the range of resulting GIC. Summarised, we choose network parameter values $(\alpha_{upper}, \beta_{upper})$ and $(\alpha_{lower}, \beta_{lower})$ sampled from the interquartile range such that equation (53) is maximised for every time instance t_i in the time-series $\{t_1, ..., t_n\}$,

$$\begin{aligned} GIC_{upper}(t_i) - GIC_{lower}(t_i) &= \Big(\alpha_{upper}E_x(t_i) + \beta_{upper}E_y(t_i)\Big) - \Big(\alpha_{lower}E_x(t_i) + \beta_{lower}E_y(t_i)\Big) \\ &= \Big(\alpha_{upper} - \alpha_{lower}\Big)\, E_x(t_i) + (\beta_{lower} - \beta_{lower})\, E_y(t_i). \end{aligned} \quad (53)$$

This approach results in a GIC band, instead of a single estimate. Although it can be thought of as a band resulting from network parameter uncertainty, we have already shown that these parameters absorb many other uncertainties. Improving the errors in the modelling chain would narrow the distribution of network parameters and then also narrow the band. Ultimately, this prediction band can then be thought of as an error estimate in the prediction. Figure 28 shows such a derived band for the Halloween Storm of 29 October 2003. During this period, only 17.5% of the measured GIC data was found to be outside the non-local Québec profile prediction band.

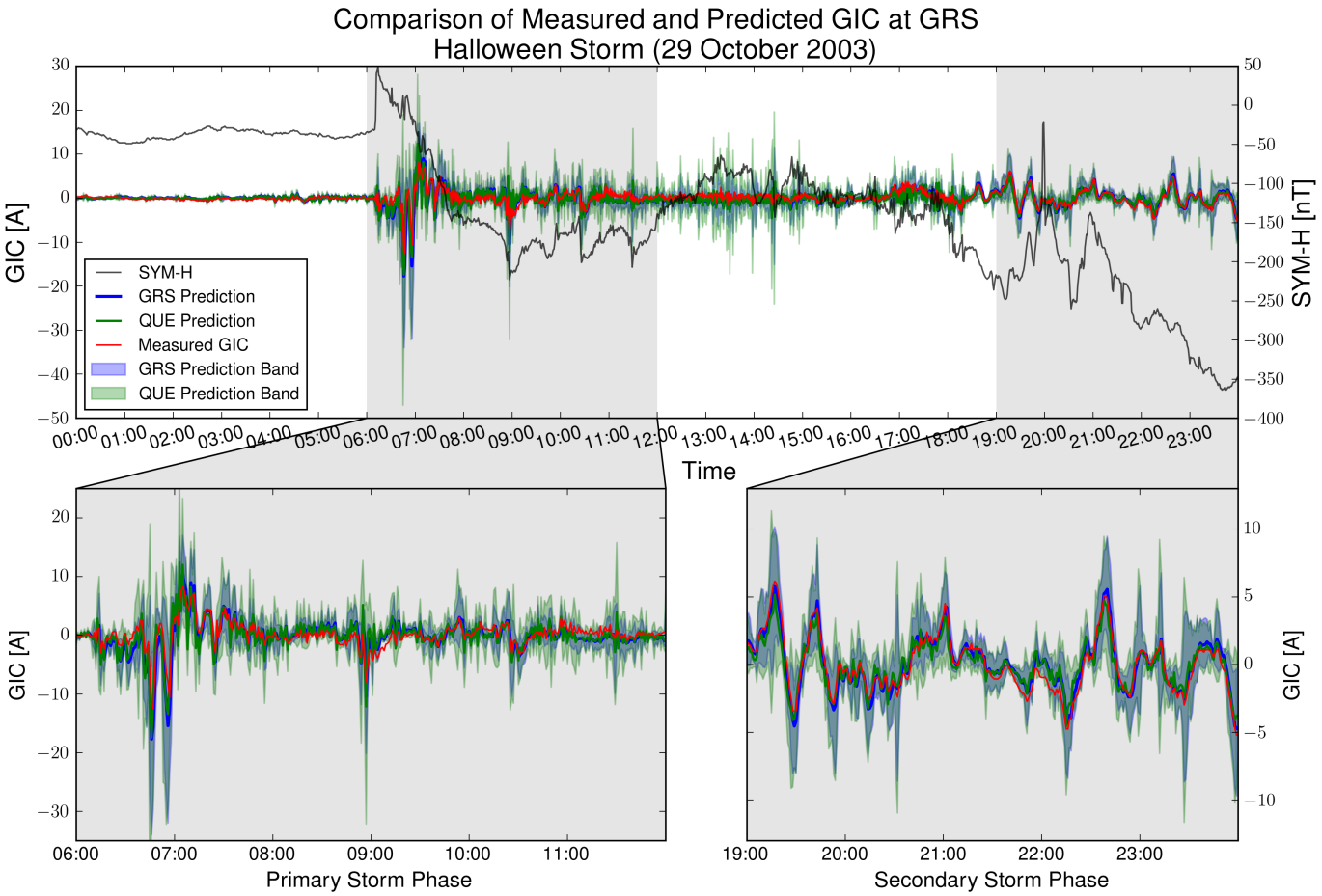

Figure 28: A direct application of an ensemble estimation of the network parameters - the GIC prediction band.

An alternative approach would be to use the observed correlation of the network parameters with GIC strength to create dynamic network parameters. The percentile range used to estimate the

parameters initially can be thought of as a window shifted through all the percentiles. That said, for a given GIC magnitude with a corresponding percentile in the training data (percentile of the GIC magnitude as if it was inserted into the historic data), we have a number of relevant percentile range estimated parameters (there is an overlap between percentile ranges). In order to estimate the parameter for this magnitude, we make use of a weighted average of all the different parameters estimates.

The normalised weighting for each estimate is done by measuring how central the given percentile is in a window. With a percentile exactly in the centre of the window, the estimate would have a weighting of 1, which linearly decreases to either side. When the percentile is on the edge or outside a window, the weighting of the estimate is 0 (see Figure 29). For the extreme percentile ranges, there will be the case that the percentile falls in only one window. This is then taken as the estimate. A disadvantage of this method is the discrete nature of the percentile range estimates and the impact of resolution of the percentile window and shifting. Given more data, the percentile window size can be decreased as well as the step shifting of the window. This will improve the resolution of the estimates and ultimately improve the accuracy. Using the GRS data with its low resolution and the non-local Québec profile (that should do a lot worse than a locally derived profile) we see an improvement nonetheless (see Table 5).

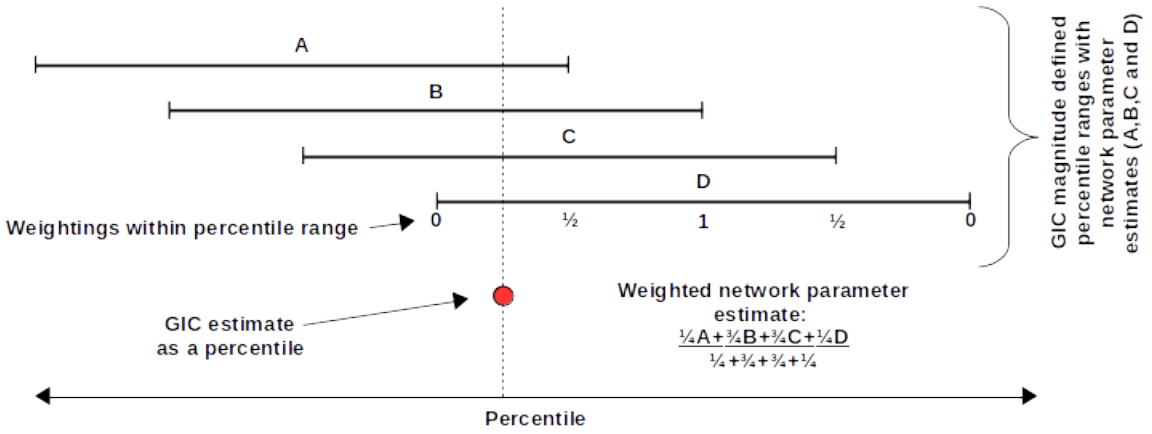

Figure 29: A diagram representing the weighted average procedure for dynamic network parameter estimation.

Québec Profile	RMSE [A] (ρ)			RE%	HE
	06:00-12:00	19:00-24:00	00:00-24:00		
Static Parameters	1.78 (0.78)	0.81 (0.93)	1.12 (0.79)	35	0.756
Dynamic Parameters	1.75 (0.82)	0.72 (0.94)	1.05 (0.82)	36	0.786
Extreme Parameters	1.97 (0.79)	0.78 (0.93)	1.21 (0.79)	36	0.752

Table 5: Dynamic network parameter estimation using GIC magnitude.

In terms of incorporating dynamic parameter estimation into a prediction scheme, power utility staff need access to real time estimates of α and β. To do this, exactly the same approach can be followed but with parameter ensemble training done according to the geoelectric field corresponding to GIC magnitude (see Section 6.3). The geoelectric field in turn can be derived from the geomagnetic field predicted by solar wind data [68, 69, 34]. This solar wind data can give an indication of an event as much as a day in advance using the WSA-ENLIL model and STEREO satellite data (depending on CME speed). This prediction can be further updated when the plasma passes the DISCOVR satellite at the L1 Lagrangian point. The lead time from this update would be of the order of 15 minutes.

This will allow an operator to monitor the status of an event and given a certain threshold, hit the big red button to implement the appropriate mitigation strategy. Alternatively, since we are more interested in modelling the largest GICs correctly, we could use the network parameters that relate to the highest percentile range solely (in the case of GRS data, this relates to the 75-100 percentile range). The resulting prediction may not do as well in terms of error metrics (see Table 5), but will allow for accurate enough prediction of the extreme events. With either of these network parameters predictions, the process will need to be continuously iterated in time to improve the final prediction.

6.3 Linking Directionality

Separate to the network parameters, the geoelectric field is the other main component in modelling GICs. As mentioned in previous sections, the orientation of this field in relation to the power network is crucial in producing GICs. Using the concept of percentile range selection for different GIC magnitudes and then binning the corresponding geoelectric field directions associated with each, we can find the typical directionality spread of the geoelectric field for a given GIC magnitude percentile range. This is done in Figure 30 for three different percentile ranges at HYD. These different ranges correspond to weakest (or 'noise'), average (or intermediate) and strongest GICs, as defined by the dataset. The geoelectric field vector corresponding to each GIC instance is then binned in the separate polar subplots according to their horizontal direction. In the case of the polar subplots, the radial extent indicates the percentage of the total data in the percentile range (and in this case, each range corresponds to 10% of the total HYD dataset) corresponding to a certain direction. Also shown is the average strength of the geoelectric field in a specific direction. This is represented through a colourbar. Taking all of this together, the predominant bins give an idea of the preferred direction of the geoelectric field to produce GICs in the given percentile range.

Although this method holds for any substation relatively close to the magnetometer, in this case we only look at HYD. The magnitude of measured GICs at a substation is expected to be modulated by the local geoelectric field magnitude and direction. In the case of strong GICs, the local geoelectric field would be roughly aligned to the local network structure. The more unaligned the geoelectric field, the larger the magnitude of the geoelectric field must be to produce large GICs. At the other end of the scale, weak GICs can result from an aligned but small magnitude geoelectric field or an unaligned but significant geoelectric field. Both of these results are observed in Figure 30. At HYD, the network forms a T-junction, with a SW-NE line running through the substation and a SE-NW line terminating at the substation. It is expected that the SE-NW terminating line contributes to the measured GIC since any induced current in this line is forced to ground, whereas the transmission line that goes through substation will allow flow to continue past the node [60, 67]. With this assumption, we see that the strong GICs are mostly aligned, with some spread in directionality. Complete non-alignment seems almost non-existent as expected, with slight non-alignment requiring very large magnitude geoelectric fields to produce large GICs. The weak GICs show a large spread of directions and are at times aligned (small geoelectric field) but mostly are not (as expected from a more significant geoelectric field with some alignment). The intermediate GICs seem to mostly have an unaligned significant geoelectric field, similar but more pronounced than the weak GICs. It should be noted that although the HER magnetometer and HYD substation are comparable for GIC modelling, the distance between them may result in an intrinsically different geoelectric field orientation at times. This may introduce the spread of directions seen. A second comment is that the 'transmission lines' (network orientation) shown in Figure 30 are in fact only the bearings towards the next nodes. This does not reflect the actual direction of the lines for the majority of the distance between nodes or in the immediate vicinity of the substation, but is rather an indication. The slight deviation from these 'transmission lines' may be explained by that fact that the network layout may be more complicated and that there is a some deviation from the plane-wave assumption, which would result in the true network layout having to be taken into account and the geoelectric field integrated along the true 'transmission lines' (see Section 1.3).

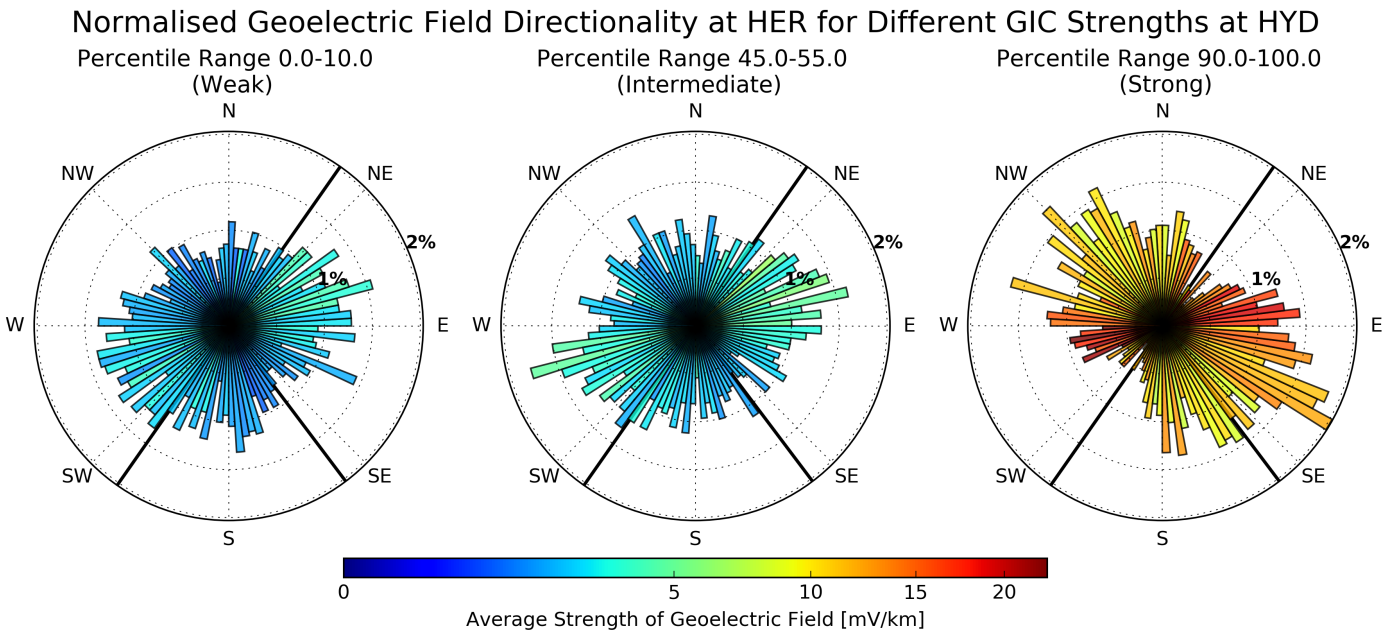

Figure 30: 'Wind socks' of the geoelectric field directionality at HER for representative GIC strengths at HYD. The amplitudes represent the relative counts (shown as percentage of data points in the percentile range) in a given direction and the colour bar represents the average strength in that direction. It should be noted that colour bar is square root stretched to emphasise the lower strengths. The bearings of the next relevant nodes in the network are also shown in the background.

A separate method of finding the preferred directionality is to make use of the $\boldsymbol{\alpha}$ and $\boldsymbol{\beta}$ ensembles and find the corresponding directionality for each parameter pair as defined in equation (37). This in turn will create an ensemble of directions. Applying this for HYD (see Figure 31), we confirm that the relevance of the network defined directionality increases with GIC magnitude. This is expected as higher GIC implies not only higher magnitude geoelectric field, but also a stronger alignment of the geoelectric field vector with the local transmission lines. With strong GICs this is clearly seen (dark red line in Figure 31), where the NW direction dominates the SE. This directionality analysis is assuming the positive polarity of the GIC only (the absolute value of the GIC magnitude is taken and hence only the 'positive' direction of the flow in the network is found). The 'positive' polarity direction depends entirely on the measurement set-up at the transformer. 'Negative' polarity flows are simply 'positive' polarity flows in the opposite direction. To give a true reflection of the directionality significance the distribution should be folded. Given that we consider only one direction of flow/polarity, contributions in the opposite direction for the same polarity would decrease the significance of that specific direction. After folding, the noise as defined by the lowest percentile range would have almost no directional dependence, as seen in the geoelectric field direction analysis above.

In this representation of directionality dependence, the network parameter response to the different GIC magnitudes is emphasised. As mentioned before, these parameters absorb errors made in the modelling chain. One such error is the possibility of a non-plane-wave driving the geoelectric field. Alternatively stated, this error could be from perturbations in the lateral conductivity structure of the Earth. Both cases would result in a non-aligned non-uniform geoelectric field. A further error could be in that the measured geomagnetic field is not the same at the node as at the magnetometer. This could mean the modelled uniform geoelectric field is not in fact aligned. Both these effects would see the resulting GIC scaled down, i.e. would be especially relevant and seen at low GIC magnitudes. In previous work, this effect was included by adding an error term (which was never quantified) to the governing equation, but in this work we see the direct result of the effects in

the network parameters [53]. At low GIC magnitudes, the network parameters display almost no directionality dependence in the directionality distribution, but the main directionality as defined by the ratio of network parameters. This indicates that at low GIC magnitudes, the associated error term dominates and quantifies the error made in the purely plane-wave geomagnetic field, solely depth dependent conductivity and uniform geoelectric field assumption. It is the higher percentile ranges, where the geoelectric field is mostly aligned, that match the plane-wave assumption and the traditional interpretation of the network parameters.

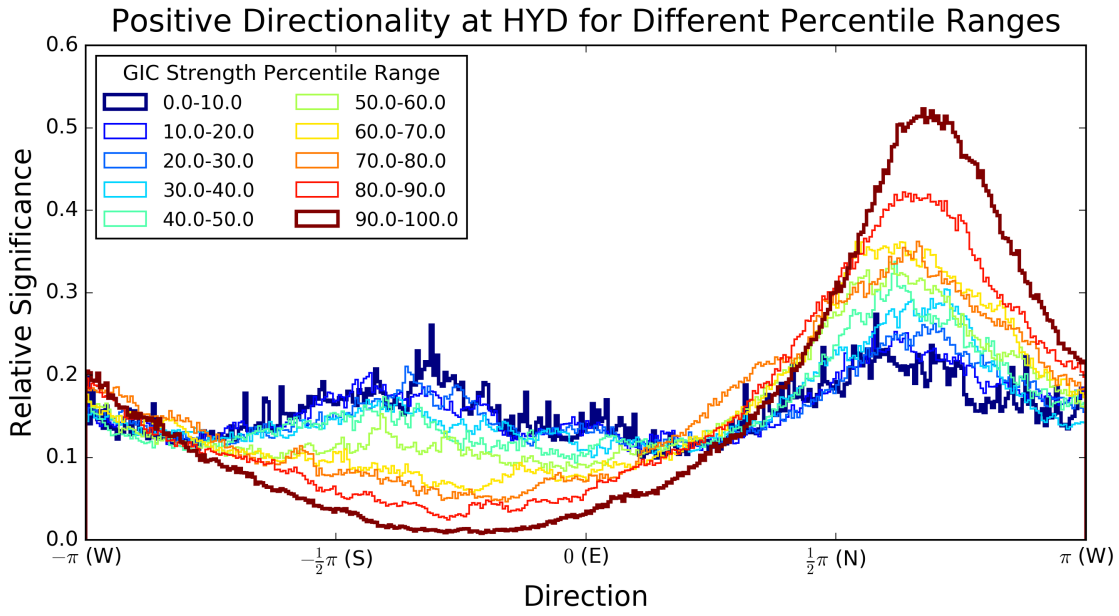

Figure 31: Plot of the normalised parameter-defined directionality distribution (direction as defined by each parameter pair). The directionality distributions varies from weak GIC (dark blue) to strong GICs (dark red) as defined by the percentile ranges.

That said, the directionality preference of the network itself should stay constant. This is predicted by the ratio of network parameters staying constant given the network parameters stay constant. From Figures 27a and 27b we see that this is the case, even for the lowest percentile ranges. This confirms the resistive network and plane-wave assumption as a first order approximation for modelling extreme GICs, but does not explain the correlation with GIC strength.

When we compare the resulting network directionality (as defined by the parameter estimates, directionality distributions and geoelectric field alignment) to the network map, we see that all these agree very well, which is expected [57]. GRS, which is an end point on a north-south line, displays predominantly north-south directionality. This makes sense since for such an end point, any GIC produced by a network aligned geoelectric field will have to terminate where the line is grounded. Since the line is north-south, a geoelectric field in this direction will produce the largest GICs. As already mentioned, at HYD we have a T-junction in the network. There is a SW-NE line that runs through the substation. From this we do not expect any significant GICs produced to be grounded when the geoelectric field is aligned since the line continues (small voltage difference). The SE-NW line that joins this line at the T-junction on the other hand would result in an endpoint. For a geoelectric field aligned in this direction, the GICs would terminate and ground. Both of these cases are clearly seen in the directionality analysis. A result of previous work regarding preferred geoelectric field directionality, is that using peak 1-hour or 3-hour values for the datasets instead of the 1-min resolution (the envelopes) result in higher directionality dependence and correlation [57]. This is effectively using the highest percentile ranges and moving away from the noise, with the end result agreeing with this work.

6.4 Validity of Governing Assumptions

Given the analysis of the network and parameter directionality with GIC strength, we have seen that the plane-wave assumption seems to hold, especially for large GICs. For the large GICs there was hardly any anti-alignment seen in the geoelectric field direction analysis. If there was, this would be an indication that the plane-wave assumption between HER and HYD does not hold. The plane-wave model is not perfect though, especially at lower GIC strengths where anti-alignment still produces GICs. These could be times when the geoelectric field aligns with the 'network' at the actual substation but not at the magnetometer from which the geoelectric field is calculated. This is expected since the magnetometer and substation are separated by a significant distance. On top of this, the relevant network itself spans a large distance and there are bound to be perturbations from the plane-wave assumption along the transmission lines. This is a reason for some of the error associated with the network parameters, but the constant ratio of network parameters and hence directionality of the network mean this is a valid enough first approximation.

What isn't explained is the changing of the network parameters with GIC strength. Given a resistive network and plane-wave driver, the assumption that the parameters are constant should be valid. The empirical ensemble estimation shows that this is not the case. This may be as a result of empirical scaling, since we see that for larger GICs the network parameters become more relevant. Although the empirical scaling is of a non-linear nature, this is most likely not a shortcoming of the ensemble method since alignment (plane-wave assumption) is not certain. Alternatively, it is a strength of the empirical method, since it gives a way to absorb this uncertainty and still relate the different components of the geoelectric field and the produced GIC.

In the case of a non-aligned geoelectric field, the resulting GIC would always be smaller than an aligned geoelectric field. This would be encoded in the network parameters. A non-uniform geoelectric field would have a similar scaling effect. In previous work, this was encoded by including an error term in the governing GIC equation [53]. A further consideration is that power network however may not be purely resistive at GIC frequencies and could include inductive effects from the transformers. As discussed in Section 6.1, an overall change in conductivity profile does not shift the network parameters, but a subset of magnitude defined estimates does. The GIC magnitude is ultimately related to the geoelectric field magnitude, which itself is dependent on the frequency scaling of the geomagnetic field. The GIC magnitude is also related to different storm phases, where we would expect to have different frequencies responses. This may suggest that there is further scaling in the frequency domain as a result of the network, apart from the frequency scaling associated with the ground conductivity profile used in the geoelectric field derivation. Either driver, or even a combination of both, may be the reason for different network parameters at different GIC levels.

7 Concluding Remarks

This work has demonstrated, for the first time, the derivation of an empirical ensemble of the traditional a and b network parameters from simultaneously observed GIC and derived geoelectric field data. These ensembles give a much better prediction compared to previous analytical and empirical methods. From analysis of the ensembles, it is shown how errors made in the derivation of the geoelectric field components are reflected in the network parameters. This has led to variation in the network parameters which can be used as an indication of the error associated with GIC prediction. Using a range of values for each of the network parameters, a band of GIC may be calculated instead of a single estimate. Furthermore, the directionality of the network was derived through the ensemble network parameters and verified by correlating the geoelectric field with GIC strength. The plane-wave assumption was found to be a valid first approximation for the large GICs. It was also shown explicitly for the first time that the network parameters are not constant and are correlated with GIC strength. This means the parameters show dependence on storm phase and ultimately time. Taking this into account when modelling GIC response to a storm as it evolves can greatly improve model accuracy. The dynamic or extreme parameter estimation approaches have been shown to do just that. The network parameter and GIC strength correlation also suggests further work could include non-uniform geoelectric fields and further frequency scaling (inductive effects).

In Section 1.4, a number of research questions were posed in order to test the hypotheses made. These questions, along with the results of investigating them can be summarised as:

RQ1: *What methods can be used to estimate the network parameters empirically from measured data?*

After an extensive literature review, a number of examples of empirical methods for deriving network parameters were found. After understanding the pros and cons of each along with the nature of the assumptions made and the data available, a new method was formulated. This method was then compared to previous empirical and analytical network parameter estimates for the South African power network and found to perform better when used in GIC modelling. See Sections 2 and 3.3.

RQ2: *Do empirically derived network parameters perform better than analytically derived network parameters when modelling extreme events?*

In this work, it was found that the new method of ensemble estimation improves on both previous empirical and previous analytical methods. Also in the previous methods applied in South Africa, the empirical methods improved on the analytical. In the literature, this is the case abroad as well. See Sections 2 and 5.1.

RQ3: *Could the uncertainty in the network parameters and specifically the error made in the empirical derivation of the network parameters be quantified?*

There has been no indication of the error associated with network parameters (and for that matter GIC modelling) in the literature. This work for the first time attempts to quantify the error by using the spread in the ensemble defined distributions. In doing so, it was shown that errors from other parts of the GIC modelling chain are absorbed into the empirically derived network parameters. Using the interquartile range, a GIC prediction band is created that effectively is a measure of the uncertainty. The closest analogous error measure is the Bootstrapping routine used for the empirical apparent surface impedance derivation [53]. See Sections 2, 3.1, 3.3 and 6.

RQ4: *What are the drivers of the error in the empirically derived network parameters?*

When dealing with analytically derived network parameters, it is a case of garbage-in garbage-out. The estimates are only as good as the network information available. This is never perfect, especially for older networks. In the case of empirically derived network parameters, a num-

ber of errors elsewhere in the GIC modelling chain are absorbed along with measurement errors in the GIC data. The errors propagated stem mainly from the derivation of the geoelectric field, where the conductivity profile dependent surface impedance is seldom well-known. Furthermore, there is uncertainty about the state of the fields, i.e. if the geomagnetic field is a plane-wave and the geoelectric field is uniform or not. The difference in the field at the network node where the GIC is measured and the magnetometer where the geomagnetic field is measured can also lead to errors if the separation is too great. See Sections 2, 3 and 4

RQ5: *When exploring the parameter-space that defines extreme geomagnetic events, do the network parameters and the associated error in them stay constant or are they sensitive to factors such as event intensity?*

The main parameters in the governing GIC equation are the GIC and geoelectric field values. The network parameters that relate the two have been the main topic of this work. The point of this research question was to see how the network parameters respond to variations in the governing equation parameters. Firstly, looking at the GIC values, this work also explored for the first time the variation of empirically derived network parameters given different GIC magnitudes. Of the parameter-space defining extreme GICs, there was not enough storm data to make a study of storm morphology, but the next best characterising factor was GIC intensity. It was shown that contrary to the assumption that network parameters are constant, they vary and become increasingly relevant with GIC magnitude. Variation has been seen before indirectly in the literature, but never quantified. Looking alternately at the geoelectric field, this work quantified the effect of different conductivities (which result in different geoelectric field values) on network parameters. Using two well defined and physically significant profiles showed that the network parameters derived remain stable, but the spread of the network parameter distributions differed. This suggested that a properly defined, physically significant and convergent profile may be used to tie down the network parameters in cases where the conductivity profile is not known. See Sections 2, 5.2 and 6.1.

Taking the results of the research into account, the validity of the hypotheses, as defined in Section 1.4, can be adjudged. These hypotheses were:

H1: *"Considering an empirically defined set of network parameters would improve the accuracy of GIC modelling during extreme geomagnetic events when compared to previous analytically derived network parameters."*

H2: *"Network parameters themselves have an intrinsic error associated with them and quantifying this error would improve GIC modelling during extreme geomagnetic events even further."*

The results of the ensemble estimation of network parameters (see Section 5 and RQ2) clearly show that the first hypothesis, H1, is confirmed. The second hypothesis, H2, has largely been confirmed (see Section 5 and 6, along with RQ3, RQ4 and RQ5). Although the uncertainty was quantified, the exact drivers of the uncertainty and their contributions to the overall uncertainty still has to be defined. This second hypothesis can be redefined to the following:

> *"Empirical network parameters derived using local data used in the plane-wave resistive network approximation have an intrinsic error associated with the impedance profile used in the geoelectric field derivation as well as conventional measurement errors. Quantifying these errors would improve GIC modelling during extreme geomagnetic events even further."*

Furthermore, this work may be useful in the context of space weather forecasting and power network management. Forecasts of the induced geoelectric field may be used to predict a band of expected GIC for an imminent event. This can further be extended to dynamic network parameter estimation to improve the modelling of GICs. This approach has been shown to be practical, but still needs to be extended into a full real time prediction tool.

References

[1] Albertson, V., Kappenman, J., Mohan, N., and Skarbakka, G. (1981). Load-Flow Studies in the Presence of Geomagnetically-Induced Currents. *IEEE Transactions on Power Apparatus and Systems*, PAS-100(2):594–607.

[2] Albertson, V., Thorson, J., and Miske, S. (1974). The Effects of Geomagnetic Storms on Electrical Power Systems. *IEEE Transactions on Power Apparatus and Systems*, PAS-93(4):1031–1044.

[3] Amuanyena, L. A. (2002). *Effect of geomagnetically induced currents on power transformers and reactors*. M.Sc. (Eng), University of Cape Town.

[4] Bernhardi, E. H., Cilliers, P. J., and Gaunt, C. T. (2008). Improvement in the modelling of geomagnetically induced currents in southern Africa. *South African Journal of Science*, 104(7-8):265–272.

[5] Bolduc, L. (2002). GIC observations and studies in the Hydro-Québec power system. *Journal of Atmospheric and Solar-Terrestrial Physics*, 64(16):1793–1802.

[6] Boteler, D. (2014). Methodology for simulation of geomagnetically induced currents in power systems. *Journal of Space Weather and Space Climate*, 4:A21.

[7] Boteler, D. and Pirjola, R. (1998a). Modelling geomagnetically induced currents produced by realistic and uniform electric fields. *IEEE Transactions on Power Delivery*, 13(4):1303–1308.

[8] Boteler, D., Pirjola, R., and Nevanlinna, H. (1998). The effects of geomagnetic disturbances on electrical systems at the Earth's surface. *Advances in Space Research*, 22(1):17–27.

[9] Boteler, D., Pirjola, R., and Trichtchenko, L. (2000). On calculating the electric and magnetic fields produced in technological systems at the Earth's surface by a "wide" electrojet. *Journal of Atmospheric and Solar-Terrestrial Physics*, 62(14):1311–1315.

[10] Boteler, D. H. and Pirjola, R. J. (1998b). The complex-image method for calculating the magnetic and electric fields produced at the surface of the Earth by the auroral electrojet. *Geophysical Journal International*, 132(1):31–40.

[11] Boteler, D. H. and Pirjola, R. J. (2017). Modeling geomagnetically induced currents. *Space Weather*, pages 1–46.

[12] Cagniard, L. (1953). Basic Theory Of The Magneto-Telluric Method Of Geophysical Prospecting. *Geophysics*, 18(3):605–635.

[13] Campbell, W. H. (1997). *Introduction to Geomagnetic Fields*. Cambridge University Press, Cambridge, UK.

[14] Campbell, W. H. (2001). *Earth Magnetism: A Guided Tour Through Magnetic Fields*. Complementary science series. Harcourt/Academic Press, San Diego, California.

[15] Cid, C., Palacios, J., Saiz, E., Guerrero, A., and Cerrato, Y. (2014). On extreme geomagnetic storms. *Journal of Space Weather and Space Climate*, 4:A28.

[16] Cravens, T. E. (1997). *Physics of Solar System Plasmas*. Cambridge University Press, Cambridge, UK.

[17] Croarkin, C. and Tobias, P. (2012). NIST/SEMATECH e-Handbook of Statistical Methods. http://www.itl.nist.gov/div898/handbook/. Last accessed on 2017-01-16.

[18] de Villiers, J. S., Kosch, M., Yamazaki, Y., and Lotz, S. (2017). Influences of various magnetospheric and ionospheric current systems on geomagnetically induced currents around the world. *Space Weather*, pages 1–15.

[19] Dong, B., Danskin, D. W., Pirjola, R. J., Boteler, D. H., and Wang, Z. Z. (2013). Evaluating the applicability of the finite element method for modelling of geoelectric fields. *Annales Geophysicae*, 31(10):1689–1698.

[20] Gaunt, C. T. (2015). Information Needed From GMD Forecasters. In *Space Weather Workshop, Boulder, CO*.

[21] Gaunt, C. T. and Coetzee, G. (2007). Transformer failures in regions incorrectly considered to have low GIC-risk. In *2007 IEEE Lausanne Power Tech*, number April, pages 807–812. IEEE.

[22] Gibbs, J. W. (2014). *Elementary Principles in Statistical Mechanics*. Dover Books on Physics. Dover Publications.

[23] Gonzalez, W. D., Joselyn, J. A., Kamide, Y., Kroehl, H. W., Rostoker, G., Tsurutani, B. T., and Vasyliunas, V. M. (1994). What is a geomagnetic storm? *Journal of Geophysical Research*, 99(A4):5771.

[24] Kappenman, J. G. (2003). Storm sudden commencement events and the associated geomagnetically induced current risks to ground-based systems at low-latitude and midlatitude locations. *Space Weather*, 1(3).

[25] Kappenman, J. G. (2005). An overview of the impulsive geomagnetic field disturbances and power grid impacts associated with the violent Sun-Earth connection events of 29-31 October 2003 and a comparative evaluation with other contemporary storms. *Space Weather*, 3(8).

[26] Kappernman, J. and Albertson, V. (1990). Bracing for the geomagnetic storms. *IEEE Spectrum*, 27(3):27–33.

[27] Keesey, L. (2014). High-Voltage Transmission Lines to Act as Antenna in First-of-its-Kind NASA Space-Weather Project. https://www.nasa.gov/content/goddard/high-voltage-transmission-lines-are-antenna-for-space-weather/. Last accessed on 2016-11-03.

[28] Kivelson, M. G. and Russell, C. T. (1995). *Introduction to Space Physics*. Cambridge University Press, Cambridge, UK.

[29] Koen, J. (2000). *Geomagnetically Induced Currents and its Presence in the Eskom Transmission Network*. M.Sc. (Eng), University of Cape Town.

[30] Koen, J. (2002). *Geomagnetically Induced Currents in the Southern African Electricity Transmission Network*. PhD, University of Cape Town.

[31] Koen, J. and Gaunt, C. T. (2002). Disturbances in the Southern African Power Network Due To Geomagnetically Induced Currents. Number August.

[32] Lehtinen, M. and Pirjola, R. J. (1985). Currents produced in earthed conductor networks by geomagnetically-induced electric fields. *Annales Geophysicae*, 3:479–484.

[33] Lotz, S. and Cilliers, P. (2015). A solar wind-based model of geomagnetic field fluctuations at a mid-latitude station. *Advances in Space Research*, 55(1):220–230.

[34] Lotz, S. I., Heyns, M. J., and Cilliers, P. J. (2017). Regression-based forecast model of induced geoelectric field. *Space Weather*, 15(1):180–191.

[35] Love, J. J., Pulkkinen, A., Bedrosian, P. A., Jonas, S., Kelbert, A., Rigler, E. J., Finn, C. A., Balch, C. C., Rutledge, R., Waggel, R. M., Sabata, A. T., Kozyra, J. U., and Black, C. E. (2016). Geoelectric hazard maps for the continental United States. *Geophysical Research Letters*, 43(18):9415–9424.

[36] Matandirotya, E., Cilliers, P. J., and Van Zyl, R. R. (2015). Modeling geomagnetically induced currents in the South African power transmission network using the finite element method. *Space Weather*, 13(3):185–195.

[37] Maynard, T., Smith, N., and Gonzalez, S. (2013). Solar Storm Risk to the North American Electric Grid - Lloyd's. *Lloyd's*, pages 1–21.

[38] McDonald, J. D. (2016). *Electric Power Substations Engineering, Second Edition.* The Electric Power Engineering Hbk, Second Edition. CRC Press.

[39] Milligan, R. O. (2015). X17 Solar Flare and Solar Storm of October 28, 2003. http://www.thesuntoday.org/historical-sun/x17-solar-flare-and-solar-storm-of-october-28-2003/. Last accessed on 2017-03-08.

[40] Molinski, T. S. (2002). Why utilities respect geomagnetically induced currents. *Journal of Atmospheric and Solar-Terrestrial Physics*, 64(16):1765–1778.

[41] Naidu, G. D. (2012). *Deep Crustal Structure of the Son-Narmada-Tapti Lineament, Central India.* Springer Theses. Springer Berlin Heidelberg, Berlin, Heidelberg.

[42] Ngwira, C. M., McKinnell, L.-A., Cilliers, P. J., Viljanen, A., and Pirjola, R. (2009). Limitations of the modeling of geomagnetically induced currents in the South African power network. *Space Weather*, 7(10).

[43] Ngwira, C. M., Pulkkinen, A., McKinnell, L.-A., and Cilliers, P. J. (2008). Improved modeling of geomagnetically induced currents in the South African power network. *Space Weather*, 6(11).

[44] NOAA SWPC (2015). G1 (Minor) Geomagnetic Storm Watch For 18 March. http://www.swpc.noaa.gov/news/g1-minor-geomagnetic-storm-watch-18-march. Last accessed on 2017-03-08.

[45] Nolan, J. P. (2016). Models for Heavy Tailed Data.

[46] Oughton, E. J., Skelton, A., Horne, R. B., Thomson, A. W. P., and Gaunt, C. T. (2017). Quantifying the daily economic impact of extreme space weather due to failure in electricity transmission infrastructure. *Space Weather*.

[47] Oyedokun, D. (2015). *Geomagnetically Induced Currents (GIC) In Large Power Systems Including Transformer Time Response.* PhD, University of Cape Town.

[48] Pirjola, R. (1982). Electromagnetic induction in the Earth by a plane wave or by fields of line currents harmonic in time and space. *Geophysica*, 18(1-2):1–161.

[49] Pirjola, R. (2010). Derivation of characteristics of the relation between geomagnetic and geoelectric variation fields from the surface impedance for a two-layer earth. *Earth, Planets and Space*, 62(3):287–295.

[50] Price, A. T. (1962). The theory of magnetotelluric methods when the source field is considered. *Journal of Geophysical Research*, 67(5):1907–1918.

[51] Pulkkinen, A., Viljanen, A., and Pirjola, R. (2006). Estimation of geomagnetically induced current levels from different input data. *Space Weather*, 4(8):1–15.

[52] Pulkkinen, A. A. (2003). *Geomagnetic Induction During Highly Disturbed Space Weather Conditions: Studies Of Ground Effects.* PhD, University of Helsinki.

[53] Pulkkinen, A. A., Pirjola, R., and Viljanen, A. (2007). Determination of ground conductivity and system parameters for optimal modeling of geomagnetically induced current flow in technological systems. *Earth, Planets and Space*, 59(9):999–1006.

[54] Riley, P. (2012). On the probability of occurrence of extreme space weather events. *Space Weather*, 10(2).

[55] Saiz, E., Guerrero, A., Cid, C., Palacios, J., and Cerrato, Y. (2016). Searching for Carrington-like events and their signatures and triggers. *Journal of Space Weather and Space Climate*, 6:A6.

[56] Solarham.com (2015). St. Patrick's Day Storm of 2015. http://www.solarham.net/march2015storm/index.htm. Last accessed on 2017-03-08.

[57] Trichtchenko, L. and Boteler, D. H. (2004). Modeling geomagnetically induced currents using geomagnetic indices and data. *IEEE Transactions on Plasma Science*, 32(4 I):1459–1467.

[58] Trivedi, N. B., Vitorello, Í., Kabata, W., Dutra, S. L. G., Padilha, A. L., Bologna, M. S., de Pádua, M. B., Soares, A. P., Luz, G. S., Pinto, F. d. A., Pirjola, R., and Viljanen, A. (2007). Geomagnetically induced currents in an electric power transmission system at low latitudes in Brazil: A case study. *Space Weather*, 5(4).

[59] Viljanen, A. and Pirjola, R. (1991). Use of Gic's in Studies of Ionospheric-Magnetospheric Currents and the Earth's Structure. In *[Proceedings] IGARSS'91 Remote Sensing: Global Monitoring for Earth Management*, volume 3, pages 1687–1690. IEEE.

[60] Viljanen, A. and Pirjola, R. (1994). Geomagnetically induced currents in the Finnish high-voltage power system. *Surveys in Geophysics*, 15(4):383–408.

[61] Viljanen, A., Pirjola, R., Prácser, E., Ahmadzai, S., and Singh, V. (2013). Geomagnetically induced currents in Europe: Characteristics based on a local power grid model. *Space Weather*, 11(10):575–584.

[62] Viljanen, A. and Pirjola, R. J. (1989). Statistics on geomagnetically-induced currents in the Finnish 400kV power system based on recordings of geomagnetic variations. *Journal of geomagnetism and geoelectricity*, 41(4):411–420.

[63] Viljanen, A., Pulkkinen, A., Amm, O., Pirjola, R., Korja, T., and BEAR Working Group (2004). Fast computation of the geoelectric field using the method of elementary current systems and planar Earth models. *Annales Geophysicae*, 22(1):101–113.

[64] Wait, J. R. (1954). On The Relation Between Telluric Currents And The Earth's Magnetic Field. *Geophysics*, 19(2):281–289.

[65] Walling, R. and Khan, A. (1991). Characteristics of transformer exciting-current during geomagnetic disturbances. *IEEE Transactions on Power Delivery*, 6(4):1707–1714.

[66] Wanliss, J. A. and Showalter, K. M. (2006). High-resolution global storm index: Dst versus SYM-H. *Journal of Geophysical Research*, 111(A2):A02202.

[67] Wik, M., Viljanen, A., Pirjola, R., Pulkkinen, A., Wintoft, P., and Lundstedt, H. (2008). Calculation of geomagnetically induced currents in the 400 kV power grid in southern Sweden. *Space Weather*, 6(7).

[68] Wintoft, P., Wik, M., Lundstedt, H., and Eliasson, L. (2005). Predictions of local ground geomagnetic field fluctuations during the 7-10 November 2004 events studied with solar wind driven models. *Annales Geophysicae*, 23(9):3095–3101.

[69] Wintoft, P., Wik, M., and Viljanen, A. (2015). Solar wind driven empirical forecast models of the time derivative of the ground magnetic field. *Journal of Space Weather and Space Climate*, 5:A7.

[70] Wu, C.-C., Wu, S. T., Dryer, M., Fry, C. D., Berdichevsky, D., Smith, Z., Detman, T., Gopalswamy, N., Skoug, R., Zurbuchen, T., and Smith, C. (2005). Flare-generated shock evolution and geomagnetic storms during the "Halloween 2003 epoch": 29 October to 2 November. *Journal of Geophysical Research: Space Physics*, 110(A9):1–14.

[71] Zhang, J. J., Wang, C., Sun, T. R., Liu, C. M., and Wang, K. R. (2015). GIC due to storm sudden commencement in low-latitude high-voltage power network in China: Observation and simulation. *Space Weather*, 13(10):643–655.

[72] Zhang, J. J., Wang, C., and Tang, B. B. (2012). Modeling geomagnetically induced electric field and currents by combining a global MHD model with a local one-dimensional method. *Space Weather*, 10(5).

[73] Zheng, K., Pirjola, R. J., Boteler, D. H., and Liu, L. G. (2013a). Geoelectric fields due to small-scale and large-scale source currents. *IEEE Transactions on Power Delivery*, 28(1):442–449.

[74] Zheng, K., Trichtchenko, L., Pirjola, R., and Liu, L. G. (2013b). Effects of geophysical parameters on GIC illustrated by benchmark network modeling. *IEEE Transactions on Power Delivery*, 28(2):1183–1191.